Coulomb interaction and phonons in doped semiconducting and metallic two-dimensional materials

Gunnar Schönhoff

Bremen 2017

Coulomb interaction and phonons in doped semiconducting and metallic two-dimensional materials

Dissertation
zur Erlangung des akademischen Grades eines
Doktor der Naturwissenschaften (Dr. rer. nat)

Universität Bremen

vorgelegt von
Gunnar Schönhoff
aus Ankum

Bremen, den 14.03.2017

1. Gutachter: Prof. Dr. Tim Wehling
2. Gutachter: Prof. Dr. Gerd Czycholl

Datum des Promotionskolloquiums: 17.05.2017

Abstract

Two-dimensional (2D) materials present a rapidly developing field of research with sometimes highly unusual and uniquely two-dimensional physics. Starting with graphene, many recent studies have investigated 2D materials, with results for properties encompassing such different topics as Dirac electrons, charge ordering, and superconductivity. To get closer to a predictive theory of the phases of 2D materials, this thesis systematically tackles the previously unclear problem of the Coulomb interaction and its influence on the electronic and many-body properties, with the focus on transition metal dichalcogenides (TMDCs). While this influence can be quite strong due to the low dimensionality and the corresponding reduced screening, there is so far no comprehensive understanding of the Coulomb interaction in 2D, its effects, and the possibilities for engineering it. Furthermore, the interplay between electron-electron interaction, electron-phonon interaction, and screening is far from being fully understood. The goal of this thesis is to improve on this by providing a description of the Coulomb interaction for the example of the TMDCs as well as to develop a material-systematic database on the basis of ab-initio calculations for electrons and phonons. We use Density Functional Theory to describe the electronic structure, Density Functional Perturbation Theory for the phonons and the electron-phonon interaction, and the Random Phase Approximation to obtain Coulomb matrix elements. In addition to both semiconducting and metallic TMDCs, we look at functionalized graphene C_8H_2. The first step is a quantification of the Coulomb interaction and the screening in the TMDCs along with calculations for the plasmonic spectra, which turn out to be highly susceptible to environment and doping. Secondly, we discuss the influence of the interaction on different many-body instabilities and find a small suppression of superconducting order in semiconducting TMDCs, depending again on doping and the dielectric environment, while the magnetic order in metallic TMDCs is enhanced. If we further include the phonons, we see that superconductivity is predicted to be a global phenomenon in the doped semiconducting TMDCs and C_8H_2, and that charge density waves at different wave vectors are supposedly occurring in all TMDCs.

Contents

1. Introduction

In recent years, the interest in low-dimensional materials has grown steadily [1]. Especially since the production of stable two-dimensional (2D) carbon called graphene by exfoliation from graphite became possible [2, 3], a lot of effort has been put into the research on these systems. The focus often lies on 2D materials consisting of a single atomic layer, such as graphene, transition metal dichalcogenides (TMDCs) or hexagonal boron nitride [4]. In bulk samples of these materials, the different layers are coupled only by weak van-der-Waals forces, thereby making it possible to obtain monolayer samples from the bulk via exfoliation techniques [3, 5]. The different 2D materials exhibit great potential, both for the finding of new physics as well as (industrial) applications such as the field of electronics and transistors [6, 7]. Another important point is the understanding of fundamental physics such as the behavior of Dirac electrons in graphene [8–10].

Although some research on monolayer TMDCs was done earlier since the 1970s [11, 12], and intercalation compounds as well as pristine bulk materials have a long history [13, 14], the advancements in the research on graphene have also fueled the research in this class of materials during the last decade [4]. The TMDCs show very rich phase diagrams, with many properties depending rather strongly on the material thickness and dimensionality while other properties remain similar from bulk to monolayer [15, 16]. These phase diagrams include a competition of semiconducting, metallic, Mott insulating, superconducting, charge density wave and magnetic phases [16–28], see Fig. 1.1.

One of the most interesting characteristics of 2D materials is the fact that they basically only consist of surfaces and are, thus, very susceptible to changes in their environment. This means that their properties can be manipulated on an atomic scale, e.g. via dielectric substrates, doping or functionalization, especially when it comes to the Coulomb interaction since this interaction as well as the electronic properties influenced by it can strongly depend on the dielectric environment [29]. Furthermore, the screening is in general reduced in 2D systems, which leads to an enhanced Coulomb interaction.

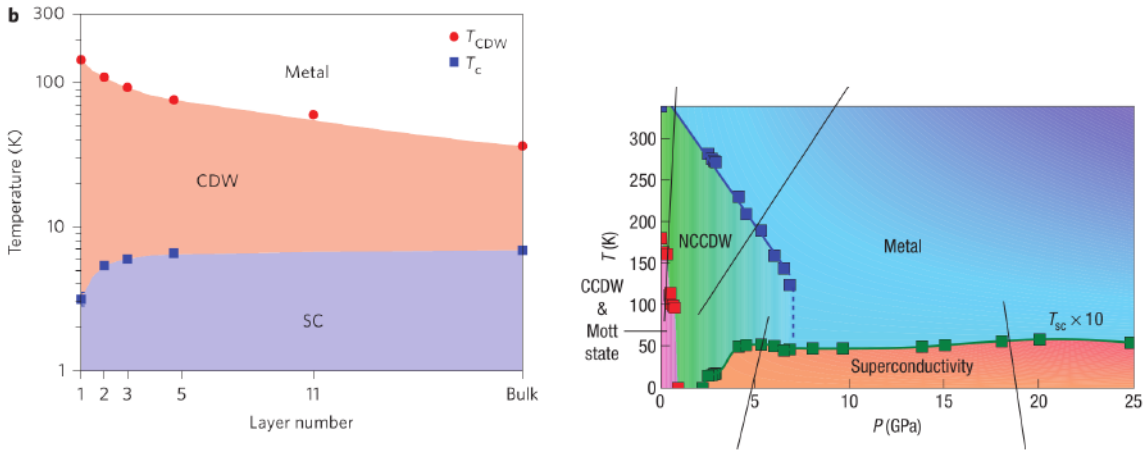

Figure 1.1.: (Left) Phase diagram of 2H-$NbSe_2$ depending on temperature and layer number, taken from [23]. The rise of the critical temperature of the charge density wave phase measured in this work is questionable, see Ref. [16]. (Right) Phase diagram of bulk 1T-TaS_2 depending on pressure and temperature, taken from [19].

Previously, it was shown that changes in the substrates lead to a different screening as well as to a renormalization of the band gap [30, 31], which can be used to engineer the properties of a material non-invasively. The final goal in this line of research is the production of tailor-made materials via the use of stacked assemblies of different monolayers, bound together by the van-der-Waals forces in so-called heterostructures which were, for example, proposed in Refs. [32, 33].

Although it can be a very important ingredient when determining the properties and phase diagram of a material, the Coulomb interaction and its effects are often not well understood. So far, only a few *ab-initio* approaches tried to quantify the interaction, especially for graphene [34, 35]. For example, it is unclear whether the dome shape observed for the superconducting phase in few-layer MoS_2 (see Fig. 1.2) and the drop of the critical temperature of superconductivity when reducing the thickness of the system to a monolayer (see Fig. 1.1 and Refs. [16, 23, 36]) might be caused by the increased Coulomb repulsion between electrons in low dimensions. A comprehensive understanding of the Coulomb interaction in 2D materials is important, not only to describe and understand the properties of these materials but also to be able to combine them efficiently in future heterostructures and other devices.

The aim of this thesis is twofold. First, we investigate the nature of the Coulomb interaction in 2D materials with a focus on the quantification of the interaction in TMDCs MX_2, consisting of transition metals $M = \mathrm{Mo}, \mathrm{W}, \mathrm{Nb}$ and chalcogens $X = \mathrm{S}, \mathrm{Se}$. We

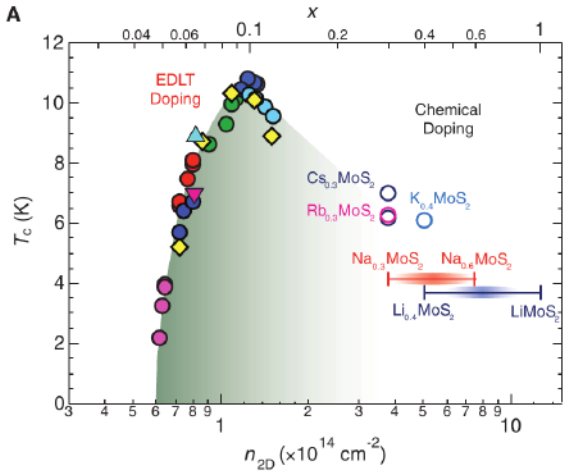

Figure 1.2.: Critical temperature of the superconducting phase of few-layer MoS_2 depending on electron doping, taken from [22].

take into account the effects of doping and different dielectric environments. A simple, material-realistic model for the TMDCs including the Coulomb interaction presents an important result. This model can also be used for other studies of this material class. Secondly, we discuss the influence of the Coulomb interaction and the electron-phonon interaction on several many-body instabilities, namely conventional superconductivity, unconventional superconductivity, charge order and spin order. For comparison, we also investigate possible superconductivity in functionalized graphene C_8H_2. In all cases, we look at metallic materials or semiconducting materials under doping.

The main methods that we employ in our studies are Density Functional Theory for the calculation of the electronic structure, the Random Phase Approximation to the electronic polarization for the description of screening effects, and Density Functional Perturbation Theory for the description of the phonon properties and the electron-phonon interaction.

The thesis is organized as follows: At first, we give an overview of the theoretical methods and underlying concepts in chapter 2. This is followed by a description of the electronic structure of the TMDC monolayers and functionalized graphene in chapter 3. Afterwards, we quantify and study the Coulomb interaction in the TMDCs in chapter 4. At last, we investigate the aforementioned many-body instabilities in chapter 5.

2. Methods and theory

In this chapter, we present the theoretical foundations of the calculations that are carried out in the later parts of the thesis. We first present some general remarks on the theory for many-body systems and recall basic concepts. After that, we give a short overview of Density Functional Theory (DFT) which is the main method we employ for our ab-initio calculations of the electronic structure. The following two sections are dedicated to the Coulomb interaction, with focus on the Random Phase Approximation (RPA), and the *GW* approximation. Having discussed the relevant theories for the electronic properties, we turn to the lattice dynamics, especially in the framework of Density Functional Perturbation Theory (DFPT). Lastly, we deal with the theories of electron-phonon superconductivity.

If not stated otherwise, we have used the Refs. [37–41] for the theoretical considerations presented in this chapter.

2.1. General many-body theory

Every closed quantum mechanical system can be described by the Schrödinger equation

$$\hat{H}|\Psi\rangle = \mathrm{i}\hbar\partial_t|\Psi\rangle \tag{2.1}$$

where the Hamiltonian $\hat{H}$ incorporates all those atomic and electronic one-particle and two-particle energy terms that are relevant for the problem at hand, see Sec. 2.1.1. For a time-independent Hamiltonian the Schrödinger equation simplifies to

$$\hat{H}|\psi\rangle = E|\psi\rangle \tag{2.2}$$

where the time evolution of the system in the state $|\psi\rangle$ with energy E is described by $|\Psi\rangle = |\psi\rangle \exp(-iEt/\hbar)$.

While the Schödinger equation gives a simple and, in principle, exact description of a quantum mechanical system, it cannot be solved exactly for more than about ten particles due to the exponential scaling of computational effort and storage demand with particle number [42]. Thus, the question in solid state physics is how to describe a system of many particles, since there is a typical number of $\sim 10^{23}$ atoms per cm^3 in bulk materials. The answer is that methods from both quantum mechanics and statistical physics need to be used, together with more or less severe approximations. Furthermore, the focus needs to be on certain quantum mechanical states like the ground state and energetically low excited states.

2.1.1. Many-body Hamiltonian

The most general Hamiltonian for a solid state system consisting of electrons and atomic cores can be written as

$$\hat{H} = \hat{T}_{\mathrm{el}} + \hat{T}_{\mathrm{at}} + \hat{V}_{\mathrm{el-el}} + \hat{V}_{\mathrm{el-at}} + \hat{V}_{\mathrm{at-at}}. \tag{2.3}$$

This includes the electronic kinetic energy $\hat{T}_{\mathrm{el}}$, the atomic core kinetic energy $\hat{T}_{\mathrm{at}}$, the electron-electron interaction $\hat{V}_{\mathrm{el-el}}$, the electron-core interaction $\hat{V}_{\mathrm{el-at}}$, and the interaction between the atomic cores $\hat{V}_{\mathrm{at-at}}$. If one explicitly considers a number of electrons at positions $\{\boldsymbol{r}_i\}$ and a number of cores at positions $\{\boldsymbol{R}_\alpha\}$, these terms are given by

$$\hat{H} = \sum_i^{N_{\mathrm{el}}} \frac{\boldsymbol{p}_i^2}{2m} + \sum_\alpha^{N_{\mathrm{at}}} \frac{\boldsymbol{P}_\alpha^2}{2m} - \sum_i^{N_{\mathrm{el}}} \sum_\alpha^{N_{\mathrm{at}}} \frac{Z_\alpha e^2}{|\boldsymbol{r}_i - \boldsymbol{R}_\alpha|} + \sum_{i>j}^{N_{\mathrm{el}}} \frac{e^2}{|\boldsymbol{r}_i - \boldsymbol{r}_j|} + \sum_{\alpha>\beta}^{N_{\mathrm{at}}} \frac{Z_\alpha Z_\beta e^2}{|\boldsymbol{R}_\alpha - \boldsymbol{R}_\beta|} \tag{2.4}$$

with electronic momenta $\boldsymbol{p}_i = -\mathrm{i}\hbar\nabla_i$, core momenta $\boldsymbol{P}_\alpha = -\mathrm{i}\hbar\nabla_\alpha$, masses of the nuclei M_α, and atomic numbers Z_α. A vacuum dielectric constant of $\varepsilon_0 = 1/(4\pi)$ for the Coulomb interaction was used here for the interaction and will be used later on, see Eq. (2.45).

In this thesis, we do not deal with the coupling of electrons or atomic cores to (external) electric or magnetic fields. This would require a time-dependent Hamiltonian with, for example, a scalar field $V_{\mathrm{ext}}(t)$.

2.1.2. Born-Oppenheimer approximation

The Born-Oppenheimer approximation [43] presents an important simplification for the treatment of a system of electrons and atomic cores. The basic assumption is that the (light) electrons follow the motion of the (much heavier) atomic cores instantaneously and with a corresponding instantaneous change of their eigenstate, which is why the approximation is sometimes called the adiabatic approximation. This leads to a seperation of the electronic and the lattice or vibrational degrees of freedom and to a product ansatz for the many-body wave function

$$|\psi\rangle = |\psi_{\mathrm{el}}\rangle|\phi_{\mathrm{at}}\rangle \tag{2.5}$$

(see also Sec. 2.5). The kinetic energy of the atomic cores is viewed as a perturbation to the rest of the system

$$\hat{H} = \hat{H}_0 + \hat{T}_{\mathrm{at}} \tag{2.6}$$

and their movement is neglected in a first step, which leads to the treatment of the electrons in the effective potential of the atoms fixed at positions $\{\mathbf{R}_\alpha\}$ via the Hamiltonian of the undisturbed system

$$\hat{H}_0 = \sum_i^{N_{\mathrm{el}}} \frac{\boldsymbol{p}_i^2}{2m} - \sum_i^{N_{\mathrm{el}}} \sum_\alpha^{N_{\mathrm{at}}} \frac{Z_\alpha e^2}{|\boldsymbol{r}_i - \mathbf{R}_\alpha|} + \sum_{i>j}^{N_{\mathrm{el}}} \frac{e^2}{|\boldsymbol{r}_i - \boldsymbol{r}_j|} + \sum_{\alpha>\beta}^{N_{\mathrm{at}}} \frac{Z_\alpha Z_\beta e^2}{|\mathbf{R}_\alpha - \mathbf{R}_\beta|}. \tag{2.7}$$

The electrons obey the Schrödinger equation

$$\hat{H}_0|\psi_{\mathrm{el},i}(\boldsymbol{r},\mathbf{R})\rangle = E_{\mathrm{el},i}(\mathbf{R})|\psi_{\mathrm{el},i}(\boldsymbol{r},\mathbf{R})\rangle, \tag{2.8}$$

i.e., their motion depends on the coordinates of the other electrons $\boldsymbol{r}$ as well as the fixed atomic positions $\mathbf{R}$ which act as parameters. The electronic Born-Oppenheimer energies $E_{\mathrm{el}}(\mathbf{R})$ then form an effective potential for the motion of the atoms via the equation

$$\left[\hat{T}_{\mathrm{at}} + E_{\mathrm{el}}(\mathbf{R})\right] |\phi_{\mathrm{at},\alpha}(\boldsymbol{R})\rangle = E_{\mathrm{at}}|\phi_{\mathrm{at},\alpha}(\boldsymbol{R})\rangle. \tag{2.9}$$

2.1.3. Second quantization

In solid state theory, the language of *second quantization*, or more accurately occupation number representation, is often used to describe the properties of a system. This means that instead of using the many-body wave functions $|\psi_\lambda\rangle$ of single particles, one uses the Fock states $|n_\lambda\rangle$ as a basis for the description of the electronic states. One starts from the indistinguishability of individual fermions (half-integral spin) or bosons (integral spin) and the behavior of their many-body wave function under particle exchange[1]. This leads to the notion that it is more reasonable to look at the occupation number n_λ of each quantum state λ than to look at the state of every single particle.

The observables and the Hamiltonian in second quantization are expressed using the creation and annihilation operators $c_\lambda^\dagger$ and c_λ for fermions (for example electrons) and $b_\lambda^\dagger$ and b_λ for bosons (for example phonons) which create or destroy a particle in a quantum state λ. They obey the (anti-)commutation rules

$$[b_\alpha^\dagger, b_\beta^\dagger]_{-\varepsilon} = [b_\alpha, b_\beta]_{-\varepsilon} = 0, \quad [b_\alpha, b_\beta^\dagger]_{-\varepsilon} = \delta_{\alpha\beta} \tag{2.10}$$

$$[c_\alpha^\dagger, c_\beta^\dagger]_{-\varepsilon} = [c_\alpha, c_\beta]_{-\varepsilon} = 0, \quad [c_\alpha, c_\beta^\dagger]_{-\varepsilon} = \delta_{\alpha\beta} \tag{2.11}$$

with the subscript $-\varepsilon$ denoting the commutator for bosons and the anticommutator for fermions. The number of particles in a single quantum state is given by the expectation value of the occupation number operator $n_\lambda = c_\lambda^\dagger c_\lambda$ for fermions, which can have eigenvalues of either 0 or 1 due to the Pauli principle, and $n_\lambda = b_\lambda^\dagger b_\lambda$ for bosons.

The general Hamiltonian for a system of interacting electrons with general quantum numbers $k_{(i)}$ in the language of second quantization reads

$$H = \sum_{k_1 k_2} \varepsilon_{k_1 k_2} c_{k_1}^\dagger c_{k_2} + \frac{1}{2} \sum_{k_1 k_2 k_3 k_4} V_{k_1 k_2 k_3 k_4} c_{k_1}^\dagger c_{k_2}^\dagger c_{k_3} c_{k_4} \tag{2.12}$$

where the single-particle matrix element $\varepsilon_{k_1 k_2}$ includes the kinetic energy $\hat{T}_{\mathrm{el}}$ of the electrons and their interaction with the (static) atoms $\hat{V}_{\mathrm{el-at}}$, see Eq. (2.3), while the two-particle matrix element $V_{k_1 k_2 k_3 k_4}$ describes the Coulomb interaction $\hat{V}_{\mathrm{el-el}}$ of two electrons with ingoing states k_3 and k_4 and outgoing states k_1 and k_2. The above Hamiltonian can be simplified via the approximation of a homogeneous electron gas or jellium model which treats the atomic cores as a uniform background charge and has

[1] The wave function is antisymmetric for fermions, i.e., it changes sign with $\varepsilon = -1$, while it is symmetric for bosons, i.e., it does not change the sign, $\varepsilon = +1$.

the electronic Hamiltonian

$$H = \sum_{k\sigma} \varepsilon_k c^\dagger_{k,\sigma} c_{k,\sigma} + \frac{1}{2} \sum_{qkk',\sigma\sigma'} V_q c^\dagger_{k+q,\sigma} c^\dagger_{k'-q,\sigma'} c_{k',\sigma'} c_{k,\sigma} \tag{2.13}$$

with $\varepsilon_k = \hbar^2 k^2/(2m)$. This Hamiltonian explicitly includes momentum conservation and the momentum exchange $\boldsymbol{q}$ via the interaction V_q between two electrons with ingoing momenta $\boldsymbol{k}$ and $\boldsymbol{k}'$, outgoing momenta $\boldsymbol{k}+\boldsymbol{q}$ and $\boldsymbol{k}'-\boldsymbol{q}$, and the spins σ and σ'. As long as $\boldsymbol{k}$ is only a momentum index and no band index is included, the model also has only a single electronic band with spin-degenerate parabolic dispersion ε_k.

2.1.4. Hubbard model and related models

The Hubbard model [44] was originally introduced to describe ferromagnetism in materials where the local Coulomb interaction is dominant. In recent years, it was used for a variety of other subjects such as the study of high-temperature superconductors [45]. It is basically a tight-binding model which includes local Coulomb interaction U_i between two electrons at lattice site i in addition to the nearest-neighbor hopping t_{ij} for an electron from site i to site j

$$H = -\sum_{\langle ij\rangle,\sigma} t_{ij} c^\dagger_{i,\sigma} c_{j,\sigma} + \sum_i U_i n_{i,\uparrow} n_{i,\downarrow}. \tag{2.14}$$

As in all other Hamiltonians presented in thesis, the Pauli principle is included here, meaning that two electrons of the same spin σ cannot occupy the same lattice site. The Hubbard model can be further simplified by assuming the same hopping t and interaction U for all lattice sites

$$H = -t \sum_{\langle ij\rangle,\sigma} c^\dagger_{i,\sigma} c_{j,\sigma} + U \sum_i n_{i,\uparrow} n_{i,\downarrow}. \tag{2.15}$$

The last equation is often simply called the Hubbard model. It cannot be solved exactly in more than one dimension if both t and U are non-zero and is mostly treated numerically by investigating a certain limit of the parameters such as $t \gg U$ or $t \ll U$. Depending on the limit and the choice of parameters, the Hubbard model exibits very different physics such as metallic behavior, antiferromagnetism or the Mott transition [46] from metal to insulator.

Several extensions to the Hubbard model are possible. In most cases, the model which includes nearest-neighbor interaction V in addition to the onsite interaction U is called

extended Hubbard model. Besides that, the model can be generalized by including hopping between sites that are not nearest-neigbor sites or by incorporating more than one electronic band.

If we want to include phonons and the interaction of electrons and phonons on a simple level, we arrive at the Hubbard-Holstein Hamiltonian[2]

$$H = -t \sum_{\langle ij \rangle, \sigma} c_{i,\sigma}^{\dagger} c_{j,\sigma} + U \sum_{i} n_{i,\uparrow} n_{i,\downarrow} + \omega_0 \sum_{i} b_i^{\dagger} b_i + g \sum_{i} n_i \left(b_i^{\dagger} + b_i \right). \tag{2.16}$$

The first two terms are the Hubbard model while the latter two constitute the electron-phonon part with phonon frequency ω_0 and electron-phonon coupling g. The use of a single phonon frequency is similar to the description of optical phonons with an Einstein mode, see Sec. 2.5.1. The Hubbard-Holstein model shows physics such as charge density wave formation and superconductivity, also in two dimensions [48]. Furthermore, one can study the transition from a metal to both a Mott insulator and a bipolaronic insulator, depending on the parameters, with this model, see Ref. [49]. The Hubbard-Holstein model can be extended for site-dependent electron-phonon interaction which leads to the Fröhlich Hamiltonian, see Sec. 2.5.3 and Eq. (2.84).

2.1.5. Green's functions

In cases where the Hamiltonian at hand is not solveable exactly, for instance a system of interacting electrons, Green's functions represent an important tool for finding approximations to the many-body problem. We start with the general time-ordered two-point correlation function at zero temperature for operators A and B which is defined via

$$G_{AB}(t, t') = -\mathrm{i} \langle \psi_0 | T A(t) B(t') | \psi_0 \rangle \tag{2.17}$$

with time ordering operator T and many-body ground state $|\psi_0\rangle$. The operator T sorts the other operators so that $TA(t)B(t') = A(t)B(t')$ if $t > t'$ and $TA(t)B(t') = B(t')A(t)$ if $t' > t$. We explicitly call those correlation functions Green's functions where the operators A and B are given by the creation or annihilation operators of fermions or bosons. Here, we use the Heisenberg picture of quantum mechanics, i.e., the full time

[2] Note that the original Holstein model [47] did not include Coulomb repulsion.

dependence is attributed to the operators via

$$A(t) = \mathrm{e}^{\mathrm{i}Ht} A(0) \mathrm{e}^{-\mathrm{i}Ht} \tag{2.18}$$

while the wave functions are independent of time. In addition to the time-ordered correlation function in Eq. (2.17), one often uses the retarded and the advanced Green's functions which are defined by

$$G^{\mathrm{R}}_{AB}(t,t') = -\mathrm{i}\Theta(t-t')\langle\psi_0|\left[A(t), B(t')\right]_{-\varepsilon}|\psi_0\rangle \tag{2.19}$$

$$G^{\mathrm{A}}_{AB}(t,t') = \mathrm{i}\Theta(t'-t)\langle\psi_0|\left[A(t), B(t')\right]_{-\varepsilon}|\psi_0\rangle \tag{2.20}$$

with the Heaviside step function $\Theta(x)$, and where the (anti)commutator is used depending on whether A and B are Fermi or Bose operators, see Eq. (2.11). Experimentally, one can measure the spectral function which is related to the Fourier transform of the retarded Green's function via

$$S_{AB}(\omega) = -\frac{1}{\pi} \operatorname{Im} G^{\mathrm{R}}_{AB}(\omega). \tag{2.21}$$

The single-electron Green's function is given by

$$G_{\alpha\beta}(t,t') = -\mathrm{i}\langle\psi_0|T c_\alpha(t) c^\dagger_\beta(t')|\psi_0\rangle \tag{2.22}$$

with fermion operators c and $c^\dagger$. This Green's function is often called the propagator because for $t > t'$, it tells us the amplitude for a particle being created at time t', going from state β to state α and being destroyed again at time t. In the opposite case $t' > t$, one can view Eq. (2.22) as the description of the propagation of a hole from state α to state β.

An especially simple description of a Green's function can be obtained using the Lehmann representation for a system described by a complete orthonormal system of eigenstates $|n\rangle$ with $H|n\rangle = E_n|n\rangle$. For a system of non-interacting electrons with dispersion $\varepsilon_{\boldsymbol{k}}$ and general quantum number $\boldsymbol{k}$, the time-evolution in Eq. (2.18) then depends only on the dispersion $\varepsilon_{\boldsymbol{k}}$ and the function in Eq. (2.22) is non-zero only for $\alpha = \beta$. Thus, we get for the one-electron (retarded) Green's function

$$G_0(\boldsymbol{k},\omega) = \frac{1}{\omega + \mathrm{i}0^+ - \varepsilon_{\boldsymbol{k}}} \tag{2.23}$$

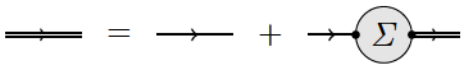

Figure 2.1.: Feynman diagram showing the Dyson equation for the Green's function as given by Eq. (2.25).

where $\mathrm{i}0^+$ is an infinitesimal number that is needed to converge the Fourier transformation on the way from Eq. (2.22) to this formula. With $A_{\boldsymbol{q}} = a_{\boldsymbol{q}} + a^\dagger_{-\boldsymbol{q}}$ and $B = A_{-\boldsymbol{q}}$ in Eq. (2.17), we can obtain the phononic Green's function which we denote by $D(\boldsymbol{q}, \omega)$. In the non-interacting case, this yields

$$D_0(\boldsymbol{q}, \omega) = \frac{1}{\omega + \mathrm{i}0^+ - \omega_{\boldsymbol{q}}} - \frac{1}{\omega - \mathrm{i}0^+ + \omega_{\boldsymbol{q}}} = \frac{2\omega_{\boldsymbol{q}}}{\omega^2 - \omega_{\boldsymbol{q}}^2 + \mathrm{i}0^+}. \tag{2.24}$$

The possible excitation energies of the system are given by the singularities of these Green's functions. From the above retarded Green's functions we can obtain the thermal Green's function by going from the analytical continuation $\mathrm{i}\omega = \omega + \mathrm{i}0^+$ to the Matsubara frequencies $\omega_n = (2n+1)\pi/\beta$ for fermions and $\omega_n = 2n\pi/\beta$ for bosons, where $\beta = 1/(k_\mathrm{B}T)$ is the inverse temperature.

The formalism of Green's functions is especially suited to treat the effects of interactions. When going from non-interacting to interacting particles, one introduces the concept of self-energy. This quantity, denoted by $\Sigma(\boldsymbol{k}, \omega)$, contains all interaction effects. Its real part contains information on the energy renormalization of the quasiparticles while the imaginary part gives their lifetime. The full Green's function can be calculated from the self-energy and the non-interacting Green's function using the Dyson equation

$$G(\boldsymbol{k}, \omega) = G_0(\boldsymbol{k}, \omega) + G_0(\boldsymbol{k}, \omega)\Sigma(\boldsymbol{k}, \omega)G(\boldsymbol{k}, \omega) \tag{2.25}$$

which is also shown in the language of Feynman diagrams in Fig. 2.1. The self-energy is given by a sum over those diagrams that are considered to be relevant for the problem at hand; an example for a frequent approximation is the GW approximation which we discuss in Sec. 2.4.

2.1.6. Wannier functions

Wannier functions [50] are defined as the Fourier transformations of Bloch functions. The latter are described by

$$\psi_{\boldsymbol{k}}(\boldsymbol{r}) = \mathrm{e}^{\mathrm{i}\boldsymbol{k}\boldsymbol{r}} u_{\boldsymbol{k}}(\boldsymbol{r}) \tag{2.26}$$

for an isolated electronic band in a crystal where $u_{\boldsymbol{k}}(\boldsymbol{r})$ is a function that has the same periodicity as the lattice. The Wannier functions are localized orbitals given by

$$w_{\mathbf{R}}(\boldsymbol{r}) = \frac{1}{N} \sum_{\boldsymbol{k}} \mathrm{e}^{-\mathrm{i}\boldsymbol{k}\mathbf{R}} \psi_{\boldsymbol{k}}(\boldsymbol{r}) \tag{2.27}$$

with lattice vectors $\mathbf{R}$ and number of primitive cells N. Since the phases of the Bloch functions can be freely chosen, one can use the phases in such a way that they lead to a set of convenient Wannier functions.

In this thesis, we make use of the software code Wannier 90 [51, 52] to obtain a simple description of the electronic states around the Fermi energy in the transition metal dichalcogenides, see Sec. 3.1.2. The algorithm is based on the construction of Wannier functions $w_{n\mathbf{R}}(\boldsymbol{r})$ for a set of N Bloch bands via

$$|w_{n\mathbf{R}}\rangle = \frac{V}{2\pi^3} \int_{\mathrm{BZ}} \left[\sum_{m=1}^{N} U_{mn}^{(\boldsymbol{k})} |\psi_{m\boldsymbol{k}}\rangle \right] \mathrm{e}^{-\mathrm{i}\boldsymbol{k}\mathbf{R}} \mathrm{d}\boldsymbol{k} \tag{2.28}$$

where $m, n \in N$. The unitary matrix $\mathbf{U}^{(\boldsymbol{k})}$ mixes the different bands at the wave vector $\boldsymbol{k}$ and BZ stands for the integration over the whole Brillouin zone. The matrix $\mathbf{U}^{(\boldsymbol{k})}$ is usually chosen via the maximal localization scheme implemented in Wannier 90 that was proposed in Ref. [53]. This scheme minimizes the functional

$$\Omega = \sum_{n}^{N} \langle w_{n\mathbf{0}} | (\boldsymbol{r} - \overline{\boldsymbol{r}}_n)^2 | w_{n\mathbf{0}} \rangle \tag{2.29}$$

which is the sum of the quadratic spreads of the Wannier functions around their centers. The functional can be decomposed into two terms

$$\Omega_I = \sum_{n} \left[\langle w_{n\mathbf{0}} | r^2 | w_{n\mathbf{0}} \rangle - \sum_{m\mathbf{R}} |\langle w_{m\mathbf{R}} | \mathbf{r} | w_{n\mathbf{0}} \rangle|^2 \right] \tag{2.30}$$

$$\tilde{\Omega} = \sum_{n} \sum_{m\mathbf{R} \neq n\mathbf{0}} |\langle w_{m\mathbf{R}} | \mathbf{r} | w_{n\mathbf{0}} \rangle|^2 \tag{2.31}$$

where Ω_I is insensitive to changes in $\mathbf{U}^{(k)}$. Thus, for an isolated set of bands, the minimization is only performed for $\tilde{\Omega}$, which leads to the computation of the overlap matrix of periodic Bloch functions

$$M_{mn}^{kb} = \langle u_{m,k} u_{n,k+b} \rangle. \tag{2.32}$$

If the N Bloch bands of interest inside an *inner* energy window are not isolated but entangled with other bands, one has to look at the $N_{\mathrm{Win}}^{(k)} \geq N$ states within an *outer* energy window and perform a disentanglement as described in Ref. [54] via

$$|u_{nk}^{\mathrm{opt}}\rangle = \sum_m U_{mn}^{\mathrm{dis}(k)} |u_{mk}\rangle \tag{2.33}$$

where $m \in N_{\mathrm{Win}}^{(k)}$, $n \in N$, and $U^{\mathrm{dis}(k)}$ is the disentanglement matrix. In this work, we use this disentanglement of the electronic bands but not the maximal localization. This is due to the fact that we use only first-guess Wannier functions to retain the symmetry of the corresponding atomic orbitals. Thus, to obtain the relevant Wannier functions, we start with N trial functions $g_n(\boldsymbol{r})$ as a first guess and need to project them onto the periodic parts of the Bloch functions via

$$|\phi_{nk}\rangle = \sum_m A_{mn}^{(k)} |u_{mk}\rangle \tag{2.34}$$

where the overlap matrix is

$$A_{mn}^{(k)} = \langle u_{mk} | g_n \rangle. \tag{2.35}$$

After that, $\mathbf{A}\mathbf{S}^{1/2}$ with $S_{mn}^{(k)} = \langle \phi_{mk} | \phi_{nk} \rangle$ is used as the inital guess for $U^{\mathrm{dis}(k)}$ and the spread functional Ω_I is minimized with respect to this matrix.

2.2. Density Functional Theory

Density Functional Theory (DFT) was originally developed by Hohenberg, Kohn and Sham in 1964 and 1965 [55, 56]. Especially since large-scale numerical calculations have become possible in the late eighties and early nineties, this theory has become very successful and is used as a standard tool today to study the electronic and geometric structure of atoms, molecules, and solids in materials science and chemistry [57]. While

the theory does not work well in some cases such as many chemical reactions[3] or strongly correlated materials, it is, for example, able to accurately predict atomic geometries. Following the frequent use and success of DFT, the Nobel prize in chemistry was awarded to Walter Kohn in 1998.

The basic idea of DFT is that it uses the electronic density n instead of the wave functions to calculate the electronic structure, following the two Hohenberg-Kohn theorems which state that

- the ground-state properties of a system of electrons are uniquely determined by the electronic density $n(\boldsymbol{r})$
- the correct ground-state electron-density minimizes the energy functional of the system.

Thus, one does not have to solve equations for the many-body wave function of N particles with $3N$ degrees of freedom such as the Schrödinger equation, but has to deal only with the electron density which only depends on three spatial coordinates.

DFT essentially only describes the ground-state properties of a system. Furthermore, in the most common approximations, DFT is only able to describe systems with weak electronic correlations. More advanced methods such as LDA+U [59] or DMFT [60] have to be used for strongly correlated systems. In this thesis, we restrict ourselves to cases without strong correlations in the sense of the Hubbard model and the Mott transition. We mainly use the software package Quantum Espresso [61] to calculate electronic properties via DFT. Additionally, we have used the FLEUR code [62] and checked our results with VASP [63, 64].

2.2.1. Formalism

Here, we aim only at a short description of the cornerstones of DFT as we will use it later on. Detailed reviews of the foundations and the formalism of DFT as well as its relation to Hartree-Fock, Hartree and Thomas-Fermi approaches can be found in many textbooks and articles such as [65].

[3] For example, even the energy barrier in such simple reactions as $H + H_2 \rightarrow H_2 + H$ is strongly underestimated by standard DFT calculations; in certain cases, the results can be improved by using hybrid functionals [58].

DFT starts with a system of N electrons for which the single-particle density is given by

$$n(\boldsymbol{r}) = \int ... \int \mathrm{d}^3\boldsymbol{r}_2 ... \mathrm{d}^3\boldsymbol{r}_N |\Psi(\boldsymbol{r}, \boldsymbol{r}_2 ... \boldsymbol{r}_N)|^2 \tag{2.36}$$

where $\Psi(\{\boldsymbol{r}_i\})$ is the many-body wave function of the system and the particle number is $N = \int \mathrm{d}^3\boldsymbol{r}\, n(\boldsymbol{r})$. The energy functional of the system is

$$E[n(\boldsymbol{r})] = \frac{\langle \Psi | T + V + U | \Psi \rangle}{\langle \Psi | \Psi \rangle} \tag{2.37}$$

where T is the kinetic energy of the electrons, V is an external potential, in our case given by the periodic lattice ions, and U is the Coulomb interaction of the electrons. The Coulomb interaction (see Sec. 2.3) is split up into a Hartree term[4] and an exchange-correlation term which leads to the following form of the functional

$$E[n(\boldsymbol{r})] = T[n(\boldsymbol{r})] + \int V(\boldsymbol{r}) n(\boldsymbol{r}) \mathrm{d}^3\boldsymbol{r} + \frac{e^2}{2} \frac{1}{4\pi\varepsilon_0} \int \int \frac{n(\boldsymbol{r}) n(\boldsymbol{r}')}{|\boldsymbol{r} - \boldsymbol{r}'|} \mathrm{d}^3\boldsymbol{r} \mathrm{d}^3\boldsymbol{r}' + E_{\mathrm{xc}}[n(\boldsymbol{r})]. \tag{2.38}$$

where the kinetic energy is usually assumed to be that of the non-interacting system $T = T_0$. The Hohenberg-Kohn theorems state that the energy functional is minimized by the ground state density $n_0(\boldsymbol{r})$, so that the ground state energy is

$$E_0 = E[n_0(\boldsymbol{r})] \leq E[n'(\boldsymbol{r})] \tag{2.39}$$

for all densities $n'(\boldsymbol{r})$ with $n_0(\boldsymbol{r}) \neq n'(\boldsymbol{r})$. The ground state density determines not only the values of the total energy, but also the expectation values of all other observables in the ground state. The problem of finding this density by finding the minimum of Eq. (2.38) is usually tackled via the Kohn-Sham approach which we describe in the next section.

[4] This term is also called the direct or the density-density part of the interaction.

2.2.2. Kohn-Sham equations

To minimize the energy functional in Eq. (2.38) one uses a complete set of auxiliary single-particle wave functions ψ_α which are called Kohn-Sham orbitals and obey

$$n(\boldsymbol{r}) = \sum_\alpha |\psi_\alpha(\boldsymbol{r})|^2, \quad \langle\psi_\alpha|\psi_\alpha\rangle = 1. \tag{2.40}$$

They form the basis of a non-interacting reference system to the real electronic system.

We note that varying the energy functional with respect to $n(\boldsymbol{r})$ is equivalent to the functional derivate with respect to ψ_α^*. Both lead to the so called Kohn-Sham equations

$$\left[-\frac{\hbar^2}{2m}\Delta + V(\boldsymbol{r}) + \frac{e^2}{4\pi\varepsilon_0}\int \frac{n(\boldsymbol{r}')}{|\boldsymbol{r}-\boldsymbol{r}'|}\mathrm{d}^3\boldsymbol{r}' + V_{\mathrm{xc}}(\boldsymbol{r})\right]\psi_\alpha(\boldsymbol{r}) = E_\alpha\psi_\alpha(\boldsymbol{r}) \tag{2.41}$$

which have the form of a one-particle Schrödinger equation for the auxiliary orbitals ψ_α. The Kohn-Sham equations are in principle exact if one uses the true exchange-correlation potential $V_{\mathrm{xc}}(\boldsymbol{r}) = \frac{\delta}{\delta n}E_{\mathrm{xc}}[n]$, but this is a priori unknown, and a lot of effort can be put into the determination of the potential that works best, see Sec. 2.2.3.

Since the Coulomb interaction terms in the Kohn-Sham equations depend on the electronic density $n(\boldsymbol{r})$ and, thus, on all Kohn-Sham orbitals ψ_α, one has to follow an iterative procedure and solve the Kohn-Sham equations self-consistently. The Kohn-Sham orbitals and energies obtained in this way have no direct physical meaning and are only auxiliary quantities to determine the electron density of a system's ground state. Nevertheless, these orbitals are often used to describe the electronic structure of a system, especially of the occupied states, and tend to work well in many situations.

2.2.3. Exchange-correlation potential

The main issue and limitation of DFT is the determination of the *correct* or *best* exchange-correlation potential, i.e., finding the best[5] effective single-particle potential to be used in Eq. (2.41). While this potential is only known nearly exact for the free electron gas, several approximations have been suggested that tend to work rather well in more or less specific situations. The two approximations that are used most commonly are the Local Density Approximation (LDA) and the Generalized Gradient Approximation (GGA).

[5]Usually, this means that one wants to be able to reproduce certain experimental results.

Local Density Approximation

The LDA assumes that the exchange-correlation potential at a certain point in space does only depend on the electronic density at this point, and that this local potential is similar to the potential of a homogeneous electron gas. Thus, the exchange-correlation energy can be expressed by

$$E_{\mathrm{xc}}[n] = \int n(\boldsymbol{r})\varepsilon_{\mathrm{xc}}(n)\mathrm{d}^3\boldsymbol{r} \tag{2.42}$$

where $\varepsilon_{\mathrm{xc}}(n)$ is the exchange-correlation energy of the homogeneous electron gas. The exchange-energy of the homogeneous electron gas can be analytically expressed via

$$E_{\mathrm{x}}[n] = -\frac{3e^2}{4}\left(\frac{3}{\pi}\right)^{1/3}\int n(\boldsymbol{r})^{4/3}\mathrm{d}^3\boldsymbol{r}. \tag{2.43}$$

The correlation energy can be expressed analytically only for certain limits, and different proposals have been made for the full exchange-correlation potential in LDA. We use potentials resulting from the approach presented in Ref. [66].

Generalized Gradient Approximation

The GGA goes beyond the LDA and assumes that the exchange-correlation energy does not only depend on the local values of the density n, but also on its derivatives [67],

$$E_{\mathrm{xc}}[n] = \int n(\boldsymbol{r})\varepsilon_{\mathrm{xc}}(n, \nabla n)\mathrm{d}^3\boldsymbol{r}. \tag{2.44}$$

In this way, the GGA accounts for the fact that the true electron density is not homogeneous, which often leads to better results for the equilibrium geometry and electronic structure of a material than those obtained from LDA. For instance, LDA calculations generally yield smaller equilibrium lattices constants than GGA calculations; for example, we find 3.22 Å in LDA for a $MoSe_2$ monolayer compared to 3.28 Å in GGA (see Tab. A.1), while the experimental lattice constant for thin films of this material is 3.3 Å [68]. In the same way as for the LDA, different proposals have been made for the *best* GGA functional and we use potentials resulting from the approach presented in Ref. [69].

Pseudopotentials

Some codes for the calculation of the electronic structure, such as FLEUR, explicitly include all electrons in the calculation, while other codes, such as Quantum Espresso, use pseudopotentials which already include the effects of the core electrons. This means that only the chemically active valence electrons are treated explicitly in pseudopotential calculations while the contributions of the energetically lower and spatially more centered core electrons are approximated by the pseudopotential. Pseudopotentials come in especially handy when a code uses plane waves as a basis set, as it is the case in Quantum Espresso, since a description of the large gradients near the nucleus via plane waves is difficult.

We have used norm-conserving pseudopotentials for all our calculations in Quantum Espresso. These potentials are constructed in such a way that the resulting wave functions have the same norm as the corresponding all-electron functions inside of a certain cutoff radius. Furthermore, the wave functions are identical to the all-electron functions outside this radius.

The pseudopotentials we use for the electron-structure calculations of each material in Quantum Espresso are given in Appx. A. We always choose the potential in such a way that the calculations run smoothly and that the results are reasonable, i.e., similar to experimental results or results from higher-level theories. For example, this means that we have to take a GGA potential for the calculations of $MoSe_2$ since a LDA potential yields an indirect band gap for the monolayer, which is not found experimentally, see Sec. 3.1.1.

2.3. Coulomb interaction and screening

In this section we deal with the general description of the Coulomb interaction between electrons. If not stated differently, the formulas apply not only to the two-dimensional systems discussed in this thesis, but to general electronic systems. The real space potential for one electron in the presence of another electron at distance r, both with charges e, is given by

$$U(r) = \frac{e^2}{4\pi\varepsilon_0 r} \tag{2.45}$$

with the vacuum permittivity ε_0. For our purposes, it is more convenient to work with a representation of the Coulomb interaction in reciprocal space. This is given by the

Fourier transform of Eq. (2.45) which in the case of three spatial dimensions leads to

$$U(q) = \frac{4\pi e^2}{q^2} \tag{2.46}$$

where we use units in which $\varepsilon_0 = 1/(4\pi)$. In two dimensions, the result is different,

$$U(q) = \frac{2\pi e^2}{q}. \tag{2.47}$$

The last equations show the so-called bare interaction betweeen two electrons in vacuum. Of course, a real system contains more than two interacting electrons. Thus, one electron does not feel the full potential of a second electron, but rather a screened potential that is usually reduced due to the presence of the atomic cores and the other electrons. Since it is usually not feasible or desirable to take all electrons of a solid state system into account, one focusses on a subsystem of interest. In its simplest form, the effective screening by the other parts outside of the subsystem, which are not explicitly taken into acount, can be given in the form of a dielectric constant ε_r, so that the effectively screened interaction is given by

$$V(q) = \frac{U(q)}{\varepsilon_r}. \tag{2.48}$$

This approach of a constant screening that is not wave-vector or frequency dependent can yield reasonable results, especially if one is only interested in macroscopic properties and deals with semiconductors or insulators in the long-wavelength limit. We use it in this thesis to describe the dielectric properties of the environment around the two-dimensional layers of interest, see Figs. 4.1 and 4.6.

The use of an effective screening given by a dielectric constant is, of course, rather limited. To realistically describe the screening, especially in a metallic subsystem with free electrons, one has to go beyond this macroscopic or classical treatment and look at the microscopic effects. To this end, one has to solve the Dyson equation [cf. Eq. (2.25)] for the screened[6] interaction

$$\mathbf{W}(\boldsymbol{q},\omega) = \mathbf{V}(\boldsymbol{q}) + \mathbf{V}(\boldsymbol{q})\Pi(\boldsymbol{q},\omega)\mathbf{W}(\boldsymbol{q},\omega) \tag{2.49}$$

with the polarization $\Pi(\boldsymbol{q},\omega)$ of the material, see Eq. 2.63. This polarization can be

[6] In this thesis, the notation is always the following: the bare Coulomb interaction is denoted by U, the interaction that takes into account some or all of the screening effects from outside of the subsystem of interest is denoted by V, and the interaction that includes all screening effects is denoted by W.

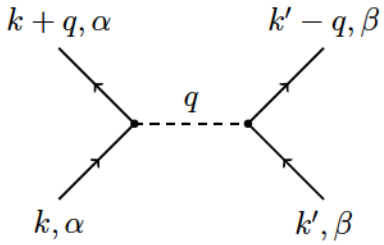

Figure 2.2.: Coulomb interaction between two electrons with momenta k and k' and quantum numbers α and β. This form of the interaction includes momentum conservation.

calculated in various ways; we use the Random Phase Approximation, see Sec. 2.3.1. In this context, the screening is defined as

$$\varepsilon(\boldsymbol{q},\omega) = \mathbb{1} - \Pi(\boldsymbol{q},\omega)\cdot\mathbf{V}(\boldsymbol{q}) \tag{2.50}$$

and is equivalent to the dielectric function which describes the response of the system to an additional or external electric field or charge distribution. The fully screened interaction is calculated via

$$\mathbf{W}(\boldsymbol{q},\omega) = \mathbf{V}(\boldsymbol{q})\varepsilon(\boldsymbol{q},\omega)^{-1} \tag{2.51}$$

which is equivalent to Eq. (2.49).

The Coulomb interaction between two electrons with momenta k and k' is symbolically shown in Fig. 2.2 and was already used for the Hamiltonian in second quantization in Eq. (2.13). When interaction matrix elements are used in this way, one always has to make sure that they are appropriately screened. This means that the screening effects of electrons outside of the (sub)system of interest have to be considered effectively, but the effects of the electrons that are treated explicitly by the Hamiltonian have to be left out of the effective treatment to prevent double-counting, cf. Sec. 2.3.2.

Let us make a short comment on terminology: In the section on DFT, see Sec. 2.2 and Eq. (2.38), we already distinguished between the different terms of the Coulomb interaction like the Hartree and the exchange term. The Hartree term, which mediates the interaction between the densities of two electronic states, n_α and n_β, and is therefore sometimes called density-density term, has a classical analogon; all other terms are purely quantum mechanical. The exchange term describes an interaction in which electronic quantum numbers are exchanged, e.g. the orbital character. This can be depicted by changing the quantum numbers α and β for the outgoing states in Fig. 2.2.

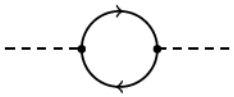

Figure 2.3.: So called *bubble*-diagrams of electron-hole excitations are summed up to get the polarization in the Random Phase Approximation.

2.3.1. Random Phase Approximation

The Random Phase Approximation (RPA) was originally presented by Bohn and Pines in 1953 [70]. It is a method to describe the response of an electronic system to an external perturbation using two-particle excitations. We employ the method in the way that was described in Ref. [71]. For a detailed derivation of the RPA formulas, see the corresponding chapter in Ref. [38]. Plasmons and electron-hole excitations are accounted for in RPA by the roots of the dielectric function, see Sec. 4.4.

The underlying principle of the RPA is that the electronic polarization Π as introduced in Eq. (2.49) is approximated by a summation of so-called *bubble*-diagrams, see Fig. 2.3. This means that the states with one particle and one hole are used to describe possible excitations to the Fermi sphere of the many-body system.[7] One performs a summation over the corresponding product of free electronic Green's functions $G_0(\boldsymbol{k}+\boldsymbol{q})G_0(\boldsymbol{k})$, cf. Eq. (2.23). Alternatively, the polarization can be obtained from the time derivative of the electron-hole excitation $c^\dagger_{\boldsymbol{k}+\boldsymbol{q}}c_{\boldsymbol{k}}$. Expectation values of the form $c^\dagger_{\boldsymbol{k}+\boldsymbol{q}}c_{\boldsymbol{k}+\boldsymbol{q}'}$ arising in this derivative are only kept if $\boldsymbol{q}=\boldsymbol{q}'$. The argument behind this is that all other contributions average out due to their randomly distributed phase factors, which is why this approximation is called Random Phase Approximation.

The Lindhard formula [72] is the final result for the electronic polarization of a free, non-interacting system with a single, spin-degenerate band. It reads

$$\Pi_0(\boldsymbol{q},\omega) = \sum_{\boldsymbol{k},\sigma} \frac{f_{\boldsymbol{k}} - f_{\boldsymbol{k}+\boldsymbol{q}}}{\hbar\omega + \mathrm{i}0^+ + \varepsilon_{\boldsymbol{k}} - \varepsilon_{\boldsymbol{k}+\boldsymbol{q}}} \tag{2.52}$$

where f is the Fermi function, ω is the frequency of the excitation, and ε describes one-particle energies. The infinitesimal quantity 0^+ was previously already used for the Green's functions in Eqs. (2.23) and (2.24). The use of the RPA means that we set $\Pi(\boldsymbol{q},\omega) = \Pi_0(\boldsymbol{q},\omega)$ in the calculation of the screening in Eq. (2.50) or the fully screened interaction via Eq. (2.49), respectively. The full charge response function is discussed later in Sec. 5.4.1 and Eq. (5.14).

[7] Excitonic effects are not considered in this approximation.

In the case of realistic materials as discussed in the following chapters of this thesis, one has to go beyond the single-band model of Eq. (2.52). For our case, this generalization was previously discussed in Refs. [71] and [73]. The general formula for the polarization of a multi-band and multi-orbital model such as the one we use for the TMDCs later in this thesis is given by the fourth rank tensor

$$\Pi_0^{\alpha\beta\gamma\delta}(\boldsymbol{q},\omega) = \sum_{\boldsymbol{k},\sigma,\lambda_1\lambda_2} M_{\lambda_1\lambda_2}^{\alpha\beta\gamma\delta} \frac{f_{\boldsymbol{k},\sigma}^{\lambda_1} - f_{\boldsymbol{k}+\boldsymbol{q},\sigma}^{\lambda_2}}{\hbar\omega + \mathrm{i}\eta + \varepsilon_{\boldsymbol{k},\sigma}^{\lambda_1} - \varepsilon_{\boldsymbol{k}+\boldsymbol{q},\sigma}^{\lambda_2}} \tag{2.53}$$

where $\alpha, \beta, \gamma, \delta$ are orbital indices, λ_1, λ_2 are band indices, and the broadening parameter η is the same as the infinitesimal 0^+ in previous equations. The involved overlap matrix elements are calculated via

$$M_{\lambda_1\lambda_2}^{\alpha\beta\gamma\delta} = \left(c_{\boldsymbol{k},\lambda_1}^{\alpha}\right)^* \left(c_{\boldsymbol{k}+\boldsymbol{q},\lambda_2}^{\beta}\right)^* c_{\boldsymbol{k}+\boldsymbol{q},\lambda_2}^{\gamma} c_{\boldsymbol{k},\lambda_1}^{\delta} \tag{2.54}$$

where the stars represent the complex conjugate. The scalars c are the expansion coefficients of the eigenfunctions corresponding to band energies $\varepsilon_{\boldsymbol{k}}^{\lambda}$ in the orbital basis. In all of our calculations using the RPA polarization, except for the Kernel L involved in the calculation of the spin susceptibility in Sec. 5.4.3, we only involve density-density matrix elements and do not take into account exchange and other higher-order terms of the Coulomb interaction. In this case, the polarization in Eq. (2.53) simplifies to

$$\Pi_0^{\alpha\beta}(\boldsymbol{q},\omega) = \Pi_0^{\alpha\beta\beta\alpha}(\boldsymbol{q},\omega). \tag{2.55}$$

So far, we did not account for the spin degeneracy of the models we use later on. For spin-degenerate electronic bands, the partial polarization is the same for up- and down-spin, and the summation over σ in Eq. (2.53) leads to the multiplication by a factor of two.

In many cases, one is just interested in the static and long wavelength limit, $\omega = 0$ and $q \to 0$, of the polarization. This limit leads to the Thomas-Fermi formula for the dielectric function in 3D

$$\varepsilon_{\mathrm{TF}}(q) = 1 + \frac{q_{\mathrm{TF}}^2}{q^2} \tag{2.56}$$

with Thomas-Fermi wave vector $q_{\mathrm{TF}} = \sqrt{4\pi e^2 \partial n/\partial\mu}$ and chemical potential μ. In 2D, the different formula for Coulomb interaction, see Eq. (2.47), results in a different

Thomas-Fermi screening

$$\varepsilon_{\mathrm{TF}}(q) = 1 + \frac{q_{\mathrm{TF}}}{q} \tag{2.57}$$

with a Thomas-Fermi wave vector $q_{\mathrm{TF}} = 2\pi e^2 N(E_{\mathrm{F}})$ [74] and a constant density of states at the Fermi level $N(E_{\mathrm{F}})$. The latter is the Thomas-Fermi limit of the polarization,

$$\Pi_0(q \to 0, \omega = 0) = -N(E_{\mathrm{F}}). \tag{2.58}$$

Another limit that can be of interest is that of a free electron gas. In this case, an analytic description of the polarization is possible, which was discussed for the two-dimensional case in Refs. [75, 76].

2.3.2. Constrained Random Phase Approximation

We shortly discuss the constrained Random Phase Approximation (cRPA) as described in Refs. [77–81]. The cRPA can be used if one aims at describing the Coulomb interaction explicitly only in a part of the (electronic) system to, for example, describe effects in this part on a higher or more detailed level of theory. The model at hand is restricted to a certain subspace of interest in the orbitals or bands, for example the electronic d-orbitals [79], while the rest of the system is already effectively included in the values of the interaction. This means that the polarization from RPA is split up into two parts,

$$\Pi \approx \Pi^{\mathrm{sub}} + \Pi^{\mathrm{rest}}, \tag{2.59}$$

with the polarization of the subsystem Π^{sub} and the polarization of the rest Π^{rest}. Only the latter, which includes all screening effects by the rest of the full electronic system, is calculated in a first cRPA step. To this end, specified electronic bands are excluded from the cRPA calculation to prevent double-counting in later calculations of the subsystem. The effective interaction between the electrons in the subspace of interest is then given by

$$\mathbf{V}_{\mathrm{eff}} = \mathbf{U}\left(\mathbb{1} - \Pi^{\mathrm{rest}} \cdot \mathbf{U}\right)^{-1} \tag{2.60}$$

with the bare interaction $\mathbf{U}$. After computing the polarization of the subsystem in a second step which only involves the bands or orbitals of this part, the fully screened interaction can be calculated similar to Eq. (2.51) via

$$\mathbf{W} = \mathbf{V}_{\mathrm{eff}}\left(\mathbb{1} - \Pi^{\mathrm{sub}} \cdot \mathbf{V}_{\mathrm{eff}}\right)^{-1}. \tag{2.61}$$

In our calculations, we make assumptions beyond Eq. (2.59) and take the only the polarization of the subsystem to be dynamic while assuming the polarization of the rest to be static,

$$\Pi^{\text{rest}} = \Pi^{\text{rest}}(q). \tag{2.62}$$

This means that also $\mathbf{V}_{\text{eff}} = \mathbf{V}_{\text{eff}}(q)$. For the metallic TMDCs, see chapter 4, the electronic band around the Fermi energy is excluded from the calculations for the partially screened effective Coulomb interaction $\mathbf{V}_{\text{eff}}$ using the Spex code [82, 83] with Wannier functions (see Sec. 2.1.6) while the fully screened interaction $\mathbf{W}$ is computed using our own RPA code on top of that. For the semiconducting TMDCs, no band is excluded since the cRPA calculation is done for the undoped systems, and Π^{sub} accounts only for the screening effects due to additional doping charges. Especially in the latter case, the cRPA approach is only justified up to a certain energy or frequency ω in the polarization and the interaction since transitions between additional doping electrons in the subsystem and bands of the rest are not accounted for; furthermore, the assumption in Eq. 2.62 is not valid at high energies.

2.4. GW approximation

While DFT can give good results for the ground state of a system, it is in general not suited to correctly describe excited-state properties[8]. One approach that can be used to obtain these properties is the GW approximation [84–86] which was first described by Hedin in 1965 [87]. For the calculations of the partially screened Coulomb matrix elements in cRPA and RPA, we use the GW-code Spex [82, 83].

The calculation in this framework starts with a set of self-consistent equations that were derived by Hedin

$$\begin{aligned} G(1,2) &= G_0(1,2) + G_0(1,1')\Sigma(1',2')G(2',2) \\ W(1,2) &= U(1,2) + U(1,3)\Pi(3,4)W(4,2) \\ \Sigma(1,2) &= \mathrm{i}G(1,3)\Gamma(3,2,4)W(4,1) \\ \Pi(1,2) &= -\mathrm{i}\Gamma(3,4,2)G(1,3)G(4,1) \\ \Gamma(1,2,3) &= \delta(1,2)\delta(1,3) + \frac{\delta\Sigma(1,2)}{\delta G(4,5)}G(4,6)G(7,5)\Gamma(6,7,3) \end{aligned} \tag{2.63}$$

where the generalized number indices encompass time, spin and space, G_0 is the single-particle Green's function, see Eq. (2.23), U is the bare Coulomb interaction, and the equations for the Green's function G and the screened Coulomb interaction W are the same as the Dyson equations (2.25) and (2.49). This means that the calculation of the self-energy Σ is performed via the term

$$\Sigma = \mathrm{i}GW\Gamma. \tag{2.64}$$

So far, the Hedin equations (2.63) are a formally exact solution to the many-body problem. The omission of vertex corrections and terms of higher order in G and W, i.e., setting $\Gamma = 1$, leads to the GW approximation for the self-energy

$$\Sigma = \mathrm{i}GW. \tag{2.65}$$

Furthermore, the polarization Π is then given by the diagram in Fig. 2.3 and the screened interaction is calculated within the RPA, see Sec. 2.3.1.

[8] Although eigenenergies of Kohn-Sham functions often agree rather well with quasiparticle energies obtained from photoemission experiments, there is no theoretical justification for such an equalization and the electronic band gap is often found to be off in DFT calculations [84].

As a simple approach to or starting point for the self-energy, one often retains just the first part of the Dyson series in G and W which leads to

$$\Sigma = \mathrm{i} G_0 W_0 \tag{2.66}$$

with non-iterated Coulomb interaction W_0 and single-particle Green's function G_0. If one takes the bare Coulomb interaction U and not the dynamically screened interaction W in the calculation of the self-energy, the self-energy is equal to the Hartree-Fock exchange potential. Thus, the GW approximation can be viewed as an extension of the Hartree-Fock method. For weakly screened systems like atoms or molecules, the results of the two approaches can lie closely together and performing GW calculations on top of Hartree-Fock calculations can lead to improved results [86, 88].

The GW method gives a good description of the excited-state properties of systems with small or moderate electronic correlation. For example, the description of the electronic band gap in semiconductors is improved compared to DFT. In many cases, it is useful to first calculate the ground-state properties using DFT and then use GW to go further, as it is done by the combination of the codes Fleur [62] and Spex [82, 83] that we use. For systems with large electronic correlations, GW calculations can be insufficient and more advanced methods like GW+DMFT [89] or Dual Boson [90, 91] are useful.

2.5. Lattice dynamics

Lattice vibrations are very important to understand solids since they determine many properties of solid materials such as infrared, Raman and neutron diffraction spectra, sound velocities, specific heat, elasticity, and thermal expansion. The quasiparticles of the lattice vibrations are called phonons. In this section, we describe the basic properties of phonons, give an overview of the basic ideas of Densitiy Functional Perturbation Theory, which we use to calculate phononic spectra, and discuss electron-phonon coupling.

2.5.1. Acoustic and optical phonons

Phonons are quantized lattice vibrations which can in many cases be described by harmonic oscillators

$$H_{\mathrm{ph}} = \sum_k \hbar\omega_k \left(b_k^\dagger b_k + \frac{1}{2} \right) \tag{2.67}$$

where ω_k defines the dispersion of a phonon with wave vector k. Due to this possible description, phonons are bosonic quasiparticles. One phonon can be interpreted as a normal mode for which all atoms of the crystal lattice vibrate with a single frequency. All other vibrations can be constructed by superimposing several phonon modes.

To illustrate their behavior, the first description of phonons in lectures and books is often done for a one-dimensional atomic chain. In this case, the phonon dispersion for a periodic chain with n different atoms consists of one acoustic branch, which is characterized by $\omega_k \to 0$ for $k \to 0$, and $n-1$ optical branches, which have a higher and finite frequency for $k \to 0$. Regular two- or three-dimensional lattices have three acoustic branches and $3n-3$ optical branches for n atoms in the unit cell. The generalization of the Hamiltonian in Eq. (2.67) for this case is given by

$$H_{\mathrm{ph}} = \sum_{\boldsymbol{k},\lambda} \hbar\omega_{\boldsymbol{k},\lambda} \left(b_{\boldsymbol{k},\lambda}^\dagger b_{\boldsymbol{k},\lambda} + \frac{1}{2} \right) \tag{2.68}$$

with three-dimensional wave vector $\boldsymbol{k}$ and branch index λ. The acoustic branches describe the dispersion resulting from simultaneous movements of all atoms of the unit cell in the same transverse or longitudinal direction with respect to the other unit cells of the crystal. The slope at small k of the linear dispersion $\omega_{\boldsymbol{k},\lambda} = v_\lambda k|_{k\to 0}$ of an acoustic long-wavelength phonon gives the sound velocity v_λ in this direction of the lattice. The optical branches result from oscillations of one or more atoms in the unit cell relative to other atoms in the same unit cell, such as the stretching of bonds. Optical phonons are often described with so-called Einstein modes, which means that, due to their often flat dispersion, their frequency is assumed to be constant [see for example the Hubbard-Holstein model, Eq. (2.16)].

In general, lighter atoms in the crystal lattice lead to higher frequencies of the phonon dispersions. This comes from the fact that in the harmonic approximation, the phonon

frequency can be calculated via

$$\omega_{\boldsymbol{k},\lambda} = \sqrt{\frac{K_{\boldsymbol{k},\lambda}}{M}} \tag{2.69}$$

with atomic mass M and force constant $K_{\boldsymbol{k},\lambda}$. Thus, the phonon frequency is in general proportional to the inverse of $M^{1/2}$.

To obtain the result in Eq. (2.69), one defines displacements $u_\alpha(\mathbf{R}_i)$ in spatial direction $\alpha = x, y, z$ around the equilibrium atomic positions $\mathbf{R}_i$ and uses the Taylor expansion[9] of the potential energy U of the atoms,

$$U = U_0 + \frac{1}{2}\sum_{\mathbf{R}_1\mathbf{R}_2}\sum_{\alpha\beta} u_\alpha(\mathbf{R}_1)\frac{\partial^2 U}{\partial u_\alpha(\mathbf{R}_1)\partial u_\beta(\mathbf{R}_2)}u_\beta(\mathbf{R}_2). \tag{2.70}$$

This leads to the definition of the force strength matrix

$$\Phi_{\alpha\beta}(\mathbf{R}_1 - \mathbf{R}_2) = \frac{\partial^2 U}{\partial u_\alpha(\mathbf{R}_1)\partial u_\beta(\mathbf{R}_2)}. \tag{2.71}$$

The Fourier transform of this matrix is called the dynamical matrix

$$D_{\alpha\beta}(\boldsymbol{k}) = \sum_{\mathbf{R}} \Phi_{\alpha\beta}(\mathbf{R})\mathrm{e}^{-i\boldsymbol{k}\mathbf{R}}. \tag{2.72}$$

The dynamical matrix is the basic quantity one uses to investigate the phonon properties of a material. Its eigenvalues are the force constants $K_{\boldsymbol{k},\lambda}$ which determine the phonon frequency in Eq. (2.69) via the use of an equation of motion for the atoms

$$\mathbf{D}(\boldsymbol{k})\epsilon_{\boldsymbol{k},\lambda} = M\omega^2\epsilon_{\boldsymbol{k},\lambda} = K_{\boldsymbol{k},\lambda}\epsilon_{\boldsymbol{k},\lambda} \tag{2.73}$$

with the polarization vectors $\epsilon_{\boldsymbol{k},\lambda}$ which are the eigenvectors of the dynamical matrix.

As a side note, we mention the Debye model, which aims at a description of the heat capacitance $C_V = \partial E/\partial T$ of a crystal lattice in a simple model. It uses a suitable average with the same linear dispersion relation for all branches in the extended zone

[9] In this thesis, we do not go beyond the harmonic approximation in the calculation of the phonons, which means that only the second derivative of the potential is included, which is done in most of the literature. The first derivative vanishes due to vanishing forces in the equilibrium, see Eq. 2.75.

scheme to achieve this. The result is

$$C_V^{\text{ion}}(T) = 9N_{\text{ion}}k_{\text{B}}\left(\frac{T}{\Theta_{\text{D}}}\right)^3 \int_0^{\Theta_{\text{D}}/T} \frac{x^4 \mathrm{e}^x}{(\mathrm{e}^x - 1)^2}\mathrm{d}x \tag{2.74}$$

which leads to $C_V \propto T^3$ for small temperatures and $C_V = 3N_{\text{ion}}k_{\text{B}}$ for large temperatures. This model is often used because it contains only one free, material-dependent parameter, namely the Debye temperature Θ_{D} which also appears in the calculation of the critical temperature of superconductivity via Eq. (2.105). The Debye temperature is the temperature at which every vibrational mode is excited; it is related to the Debye frequency via $\Theta_{\text{D}} = \hbar\omega_{\text{D}}/k_{\text{B}}$.

2.5.2. Density Functional Perturbation Theory

Density Functional Perturbation Theory (DFPT) is a way to calculate the properties of lattice vibrations [92, 93]. It is, for instance, implemented in Quantum Espresso [61]. The underlying approximation of the DFPT is the Born-Oppenheimer approximation, see Sec. 2.1.2, with Eq. (2.9) describing the motion of the atoms.

In the equilibrium, all forces acting on individual atoms vanish, i.e.,

$$\boldsymbol{F}_i = \frac{\partial E_{\text{el}}(\boldsymbol{R})}{\partial \boldsymbol{R}_i} = 0 \tag{2.75}$$

where $E_{\text{el}}(\boldsymbol{R})$ is the Born-Oppenheimer energy surface and $\boldsymbol{R}_i$ is the changeable position of the i-th atom. Vibrations of the lattice with frequency ω are then given by displacements of atoms from this equilibrium. They can be calculated via the Hessian matrix of interatomic force constants

$$\det\left|\frac{1}{\sqrt{M_i M_j}}\frac{\partial^2 E_{\text{el}}(\boldsymbol{R})}{\partial \boldsymbol{R}_i \partial \boldsymbol{R}_j} - \omega^2\right| = 0 \tag{2.76}$$

which is similar to the force strength matrix Φ in Eq. (2.71), scaled by the atomic masses.

To obtain the matrix in Eq. (2.76) and the corresponding dynamical matrix, DFPT makes use of the Hellman-Feynman theorem

$$\frac{\partial E_\lambda}{\partial \lambda} = \left\langle \psi_\lambda \middle| \frac{\partial H_\lambda}{\partial \lambda} \middle| \psi_\lambda \right\rangle \tag{2.77}$$

which connects the derivative of the total energy E with respect to a parameter λ to the expectation value of the derivative of the Hamiltonian with respect to the same parameter. In our case, this means that we can use derivatives of the many-body Hamiltonian with respect to the atomic positions, which act as parameters in the case of the Born-Oppenheimer Hamiltonian, see Eq. (2.7). Only the interaction between the electrons and the atomic cores $V_{\mathrm{el-at}}$ and the interaction between different atomic cores $V_{\mathrm{at-at}}$ depend on these positions. This leads to the Hellman-Feynman forces

$$\boldsymbol{F}_i = -\int n_{\mathbf{R}}(\boldsymbol{r}) \frac{\partial V_{\mathrm{el-at}}(\boldsymbol{r})}{\partial \boldsymbol{R}_i} \mathrm{d}\boldsymbol{r} - \frac{\partial V_{\mathrm{at-at}}(\boldsymbol{R})}{\partial \boldsymbol{R}_i} \tag{2.78}$$

since the electron-atom interaction only couples to electronic degrees of freedom via the charge density $n_{\mathbf{R}}(\boldsymbol{r})$ of the electrons for the unperturbed system [cf. Eq. (2.38)]. The derivatives of the Hellman-Feynman forces lead to the Hessian in Eq. (2.76) via

$$\begin{aligned} \frac{\partial^2 E_{\mathrm{el}}(\boldsymbol{R})}{\partial \boldsymbol{R}_i \partial \boldsymbol{R}_j} &= -\frac{\partial \boldsymbol{F}_i}{\partial \boldsymbol{R}_j} \\ &= \int \frac{\partial n_{\mathbf{R}}(\boldsymbol{r})}{\partial \boldsymbol{R}_j} \frac{\partial V_{\mathrm{el-at}}(\boldsymbol{r})}{\partial \boldsymbol{R}_i} \mathrm{d}\boldsymbol{r} + \int n_{\mathbf{R}}(\boldsymbol{r}) \frac{\partial^2 V_{\mathrm{el-at}}(\boldsymbol{r})}{\partial \boldsymbol{R}_i \partial \boldsymbol{R}_j} \mathrm{d}\boldsymbol{r} + \frac{\partial^2 V_{\mathrm{at-at}}(\boldsymbol{R})}{\partial \boldsymbol{R}_i \partial \boldsymbol{R}_j}. \end{aligned} \tag{2.79}$$

One can see that the ground-state electron-density and its linear response to perturbations, i.e., displacements of the atoms, are needed in order to calculate the force constant matrix or the dynamical matrix. The DFPT is a way to obtain the linear response within the framework of DFT, see chapter 2.2. To this end, one linearizes Eqs. (2.38), (2.40) and (2.41) with respect to variations of the wave function, the density and the potential, and uses first order perturbation theory.

We mention that there are other methods besides DFPT that are able to calculate the phonon properties. One popular example is the frozen phonon method which employs explicit displacements of some atomic cores according to the symmetry of the phonon at hand. Due to the fact that these calculations need a super cell corresponding to the inverse of the phonon wave vector, this method is mainly limited to phonons in the Brillouin zone center or on its boundary.

A severe limitation of the DFPT as discussed here and used in this thesis is the fact that no anharmonic effects are included. This, for example, leads to the prediction of an instability in the phonon dispersion of bulk NbS_2, cf. Fig. 5.2, which is not observed experimentally and can be lifted by including anharmonic effects, see Sec. 5.4.1. Furthermore, screening effects arising from the environment of the system are only

accounted for in this thesis when it comes to the Coulomb interaction of the electrons, see Sec. 4.2, while their possible influence on the phonons is discarded.

2.5.3. Electron-phonon coupling

The interaction of electrons and phonons is an important quantity since it can result in the formation of superconducting or CDW instabilities as discussed in chapter 5. The coupling was already included in the Hubbard-Holstein model, see Eq. (2.16), in the form of a constant coupling g. In general, however, the coupling depends on the momenta of the involved electron and phonon as well as the phonon branch. The electron-phonon coupling coefficient for electrons with wave function in state $\boldsymbol{k}$ and phonons with wave vector $\boldsymbol{q}$ in mode ν can be defined by

$$g_{q,\nu}(\boldsymbol{k}) = \left(\frac{\hbar}{2M\omega_{q,\nu}}\right)^{1/2} \left\langle \psi_{\boldsymbol{k}} \left| \frac{\partial V_{\text{el-at}}}{\partial u_{q,\nu}} \right| \psi_{\boldsymbol{k}+\boldsymbol{q}} \right\rangle \tag{2.80}$$

which describes the scattering of an electron to state $\boldsymbol{k}+\boldsymbol{q}$ due to the interaction with a lattice vibration and, thus, a change in the atomic potential. Since the variation of the potential is calculated within DFPT, the electron-phonon coupling coefficients can be also be obtained within this framework.

An important function for the description of conventional superconductivity is the electron-phonon spectral function [94]

$$\alpha^2F(\omega) = \frac{1}{N(E_\text{F})} \sum_{\boldsymbol{k}\boldsymbol{q},\nu} |g_{q,\nu}(\boldsymbol{k})|^2 \delta(\varepsilon_{\boldsymbol{k}} - E_\text{F}) \delta(\varepsilon_{\boldsymbol{k}+\boldsymbol{q}} - E_\text{F}) \delta(\omega - \omega_{q,\nu}) \tag{2.81}$$

which is the product of the phonon DOS

$$F(\omega) = \sum_{q,\nu} \delta(\omega - \omega_{q,\nu}) \tag{2.82}$$

and the averaged squared electron-phonon coupling α^2. This spectral function defines the effective coupling parameter of superconductivity via

$$\lambda = 2 \int_0^\infty \frac{\alpha^2F(\omega)}{\omega} \mathrm{d}\omega \tag{2.83}$$

which is used in Eqs. (2.105) and (2.106).

An alternative way to describe the electron-phonon interaction is the use of polarons [95]. These are the quasiparticles describing an electron in a lattice and the surrounding self-induced polarization cloud. The discussion of polarons often makes use of the Fröhlich Hamiltonian

$$H = \frac{\boldsymbol{p}^2}{2m} + \omega_{\mathrm{LO}} \sum_{\boldsymbol{k}} b_{\boldsymbol{k}}^\dagger b_{\boldsymbol{k}} + \sum_{\boldsymbol{k}} \left(V_{\boldsymbol{k}} b_{\boldsymbol{k}} \mathrm{e}^{i\boldsymbol{k}\boldsymbol{r}} + V_{\boldsymbol{k}}^* b_{\boldsymbol{k}}^\dagger \mathrm{e}^{-i\boldsymbol{k}\boldsymbol{r}} \right) \tag{2.84}$$

where the first term describes the kinetic energy of the bare electron via its momentum $\boldsymbol{p}$ and mass m, the second term describes the energy of longitudinal optical phonons with frequency ω_{LO}, and the third term describes the polarization cloud via the Fourier components $V_{\boldsymbol{k}}$ of the electron-phonon coupling. Using the Fröhlich Hamiltonian, one can derive how the properties of a polaron differ from those of a usual band electron.

2.6. Superconductivity

Superconductivity was first observed by Heike Kammerling Onnes in 1911 when he cooled mercury down below the boiling point of liquid helium [96]. In the following years, several theories were put forward to describe this new phase, with the BCS approach being the first to yield a correct explanation via the electron-phonon coupling and the formation of Cooper pairs, see Sec. 2.6.1. The two most important macroscopic properties of the superconducting state are the vanishing electrical resistance and the Meissner-Ochsenfeld effect. The latter describes the expulsion of an external magnetic field from the interior of the superconductor below the transition temperature. Raising the magnetic field above a critical value leads to the sudden breakdown of the superconducting state via a first-order phase transition in so-called type-I superconductors. In type-II superconductors, there are two critical field strengths and the magnetic field is only fully expelled from the sample below the lower strength, while magnetic vortices form inside the superconductor in the regime between the two strengths.

Besides the conventional electron-phonon coupled superconductors, there are also a variety of unconventional superconductors with a sometimes much higher critical temperature. This class consists of two main families, namely the cuprates, where high-T_{c} superconductivity was first found in 1986 [97], and the iron-based compounds [98]. These materials have in common that they exhibit a change in the phase diagram upon doping and/or pressure from an antiferromagnetic to a superconducting phase. The pairing

mechanism responsible for the formation of Cooper pairs in these materials is unclear and has received a lot of research interest. While several possible pairing mechanisms such as spin fluctuations or strong effective antiferromagnetic pairing have been discussed, no general mechanism has been found yet (see Refs. [99, 100] and Sec. 5.3).

We call all kinds of superconductivity that are not mediated by electron-phonon coupling *unconventional*. The charge carriers in all *conventional* superconductors and at least most of the unconventional superconductors are Cooper pairs consisting of two bound electrons. The pairing mechanisms or effective, attractive interactions that are needed for the formation of this bond are, however, different.

In addition to the books [38, 40], our description of the BCS theory and the Eliashberg theory for conventional superconductors in the two following sections is guided by Refs. [101] and [102].

2.6.1. BCS theory

The BCS theory of superconductivity was published by Bardeen, Cooper and Schrieffer in 1957 [103, 104]. Before this date, there were several phenomenological approaches for the description of the superconducting phase. One approach worth mentioning are the London equations [105] which are able to describe the Meissner effect.

The success of the BCS theory was that it was the first theory to correctly explain the formation of the superconducting phase, which gained the three authors the Nobel prize in 1972. The underlying assumption of the theory is that the charge carriers in a superconducting material are Cooper pairs [106] formed by two electrons. Responsible for the formation of these bound pairs is an effective attraction between the electrons which is mediated by phonons.

The Hamiltonian of the BCS theory is given by

$$H = \sum_{\boldsymbol{k},\sigma} \varepsilon_{\boldsymbol{k}} c^{\dagger}_{\boldsymbol{k}\sigma} c_{\boldsymbol{k}\sigma} - V \sum_{\boldsymbol{k},\boldsymbol{k}'} c^{\dagger}_{\boldsymbol{k}'\uparrow} c^{\dagger}_{-\boldsymbol{k}'\downarrow} c_{-\boldsymbol{k}\downarrow} c_{\boldsymbol{k}\uparrow} \tag{2.85}$$

which describes electrons with dispersion $\varepsilon_{\boldsymbol{k}}$ and includes the effective attraction V between two electrons of opposite spin and momentum forming a Cooper pair via the exchange of a momentum $\boldsymbol{q} = \boldsymbol{k}' - \boldsymbol{k}$ as shown in Fig. 2.4. The simplifications that ones uses here are that only electrons with opposite spin and momentum in a range of the Debye frequency ω_{D} around the Fermi level participate in the interaction and that

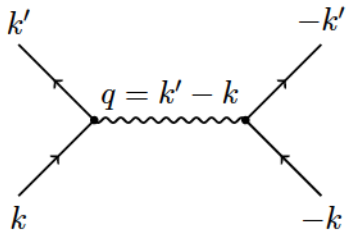

Figure 2.4.: Schematic representation of the formation of a Cooper pair via the exchange of a phonon with momentum q.

the effective interaction is a simple constant. The BCS Hamiltonian can be treated by several methods like the original variational ansatz or the Bogoliubov transformation.

These mean-field treatments for small V yield a self-consistent equation for the order parameter of the superconducting phase, the gap

$$\Delta = \frac{V\Delta}{2} \sum_{k} \frac{1}{E_k} \tanh \frac{\beta E_k}{2} \tag{2.86}$$

where the energy is $E_k = \sqrt{\varepsilon_k^2 + \Delta^2}$ and β is the inverse temperature. In the normal metallic state we get $\Delta = 0$ while for a superconducting state we find $\Delta \neq 0$. Going to small temperatures and using a constant electronic density $N(E_\mathrm{F})$ in the range $\hbar\omega_\mathrm{D}$ around the Fermi level leads to an approximation for the gap

$$\Delta(T = 0) \approx 2\hbar\omega_\mathrm{D} \mathrm{e}^{-1/[VN(E_\mathrm{F})]}. \tag{2.87}$$

The most important quantity to describe a superconducting material is probably the critical temperature T_c at which the superconducting phase sets in. This temperature can be derived by setting $\Delta \approx 0$ in Eq. (2.86) and assuming that $\hbar\omega_\mathrm{D} \gg k_\mathrm{B}T_\mathrm{c}$, since the Debye temperature is typically of the order of room temperature and the critical temperature is usually a few Kelvin. This leads to

$$T_\mathrm{c} = 1.14\,\Theta_\mathrm{D} \mathrm{e}^{-1/[VN(E_\mathrm{F})]}. \tag{2.88}$$

We see that both the critical temperature and the superconducting gap depend exponentially on the inverse of the interaction parameter

$$\lambda_\mathrm{BCS} = VN(E_\mathrm{F}). \tag{2.89}$$

As found previously in Eq. (2.69), the typical phonon frequency is proportional to the inverse of the square root of the atomic mass. Since T_c is proportional to the Debye frequency, this leads to

$$T_c \propto \frac{1}{\sqrt{M}}. \tag{2.90}$$

Thus, different isotopes of the same chemical element have different critical temperatures, which is called the isotope effect. Finding the isotope effect in experiments is regarded as an indication that the material at hand is a conventional superconductor. We mention that the highest temperatures in electron-phonon superconductors are generally possible when hydrogen atoms are included in or responsible for the electron-phonon coupling.[10]

While providing a simple and intuitive picture for the understanding of conventional superconductivity and being able to calculate the superconducting properties of simple materials, there are severe limitations to the BCS theory. It is only a mean field theory for weak electron-phonon coupling, and this coupling is only taken into account in an effective way. Furthermore, no Coulomb interaction between the electrons is (explicitly) included in the BCS theory. Thus, an extension in form of the Eliashberg theory is needed.

2.6.2. Eliashberg theory

The Eliashberg theory of superconductivity [94, 108] was first put forward in 1960 [109]. It is basically an extension of the BCS theory which deals with strong electron-phonon coupling $\lambda \sim 1$ and also includes the Coulomb interaction explicitly.

The Eliashberg theory is conveniently derived using the Nambu formalism [110] which treats the electron operators in the form of spinors

$$\psi_k = \begin{pmatrix} c_{k\uparrow} \\ c^\dagger_{-k\downarrow} \end{pmatrix}, \quad \psi^\dagger_k = (c^\dagger_{k\uparrow},\ c_{-k\downarrow}). \tag{2.91}$$

From this notation one can already see that the starting point of this theory is similar to the BCS theory since it also uses Cooper pairs composed of electrons with opposite spin and momenta. The general Hamiltonian for electrons, phonons and their interactions

[10] Sulfur hydrides have gained a lot of interest recently due to the finding of a superconducting phase with T_c of up to 203 K [107].

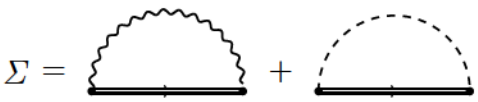

Figure 2.5.: Self energy diagrams with electron-phonon and electron-electron interaction that are included in the Eliashberg theory.

reads in this notation

$$H = \sum_{\boldsymbol{k}} \varepsilon_{\boldsymbol{k}} \psi^\dagger_{\boldsymbol{k}} \sigma_3 \psi_{\boldsymbol{k}} + \sum_{\boldsymbol{q}\lambda} \omega_{\boldsymbol{q},\lambda} b^\dagger_{\boldsymbol{q},\lambda} b_{\boldsymbol{q},\lambda} + \sum_{\boldsymbol{k}\boldsymbol{k}'\lambda} g_{\boldsymbol{k}-\boldsymbol{k}',\lambda}(\boldsymbol{k}) \phi_{\boldsymbol{k}-\boldsymbol{k}',\lambda} \psi^\dagger_{\boldsymbol{k}'} \sigma_3 \psi_{\boldsymbol{k}} + \frac{1}{2} \sum_{\boldsymbol{k}_1\boldsymbol{k}_2\boldsymbol{k}_3\boldsymbol{k}_4} \langle \boldsymbol{k}_3\boldsymbol{k}_4 | W | \boldsymbol{k}_1\boldsymbol{k}_2 \rangle (\psi^\dagger_{\boldsymbol{k}_3} \sigma_3 \psi_{\boldsymbol{k}_1})(\psi^\dagger_{\boldsymbol{k}_4} \sigma_3 \psi_{\boldsymbol{k}_2}). \quad (2.92)$$

with electronic dispersion $\varepsilon_{\boldsymbol{k}}$, phonon frequency $\omega_{\boldsymbol{q},\lambda}$, electron-phonon coupling $g_{\boldsymbol{q},\lambda}(\boldsymbol{k})$, (appropriately screened) static Coulomb interaction W, and the phonon operator in the Nambu formalism $\phi_{\boldsymbol{q},\nu} = b_{\boldsymbol{q},\nu} + b^\dagger_{-\boldsymbol{q},\nu}$. The Pauli matrices are

$$\sigma_1 = \begin{pmatrix} 0 & 1 \\ 1 & 0 \end{pmatrix}, \quad \sigma_2 = \begin{pmatrix} 0 & -\mathrm{i} \\ \mathrm{i} & 0 \end{pmatrix}, \quad \sigma_3 = \begin{pmatrix} 1 & 0 \\ 0 & -1 \end{pmatrix}. \quad (2.93)$$

To obtain information on the state of the system, one has to solve the Dyson equation (2.25) for the 2×2 Green's function matrix of the electrons

$$\mathbf{G}(\boldsymbol{k}, \tau) = -\langle T_\tau \psi_{\boldsymbol{k}}(\tau) \psi^\dagger_{\boldsymbol{k}}(0) \rangle. \quad (2.94)$$

The most important ingredient is the self-energy of the electrons. Usually, the self-energy in the framework of Eliashberg theory is found by using a theorem by Migdal [111] which states that vertex corrections can be omitted since $\sqrt{m_{\mathrm{eff}}/M} \sim \omega_{\mathrm{D}}/E_{\mathrm{F}} \ll 1$ with effective electron mass m_{eff} and atomic mass M, i.e., because electrons and phonons live on different energy scales. The only remaining contributions to the self-energy are shown in Fig. 2.5. This diagram leads to

$$\Sigma(\boldsymbol{k}, \mathrm{i}\omega_n) = -\frac{1}{\beta} \sum_{\boldsymbol{k}'n'\nu} \sigma_3 G(\boldsymbol{k}', \mathrm{i}\omega_{n'}) \sigma_3 \left[|g_{\boldsymbol{k}-\boldsymbol{k}',\nu}(\boldsymbol{k})|^2 D_\nu(\boldsymbol{k}-\boldsymbol{k}', \mathrm{i}\omega_n - \mathrm{i}\omega_{n'}) + W(\boldsymbol{k}-\boldsymbol{k}') \right] \quad (2.95)$$

where the phonon Green's function $D_\nu(\boldsymbol{q}, \mathrm{i}\omega_n)$ in imaginary frequencies is the Fourier transform of $D_\nu(\boldsymbol{q}, \tau) = -\langle T_\tau \phi_{\boldsymbol{q},\nu}(\tau) \phi^\dagger_{\boldsymbol{q},\nu}(0) \rangle$. Splitting up the self-energy into odd and

even parts with respect to the Matsubara frequency $\mathrm{i}\omega_n$ leads to

$$\Sigma(\boldsymbol{k}, \mathrm{i}\omega_n) = \mathrm{i}\omega_n[1 - Z(\boldsymbol{k}, \mathrm{i}\omega_n)]\mathbb{1} + \chi(\boldsymbol{k}, \mathrm{i}\omega_n)\sigma_3 + \phi(\boldsymbol{k}, \mathrm{i}\omega_n)\sigma_1 + \overline{\phi}(\boldsymbol{k}, \mathrm{i}\omega_n)\sigma_2. \tag{2.96}$$

One now uses the one-particle Green's functions for electrons, Eq. (2.23), and inserts them into the Dyson equation for the full Green's function together with the self-energy. If we then put the full electronic Green's function and the one-particle Green's function for the phonons, Eq. (2.24), into Eq. (2.95), and compare to Eq. (2.96), we get the equations for the individual components.[11] Afterwards, several approximations are used; one assumes that the components of the self-energy are only non-zero around the Fermi level and that it is, thus, senseful to take the average over the Fermi surface k_F and omit wave vector dependencies. Furthermore, one uses a constant electronic DOS $N(E_\mathrm{F})$ and sets $\chi = 0$ due to the fact that it only brings about a small shift of the energy scale. In the end, the self-energy equations that have to be solved self-consistently read

$$\begin{aligned} \mathrm{i}\omega_n[1 - Z(\mathrm{i}\omega_n)] &= -\frac{\pi}{\beta}\sum_{n'} \frac{\mathrm{i}\omega_{n'} Z(\mathrm{i}\omega_{n'})}{\Xi(\mathrm{i}\omega_{n'})} [\lambda(\mathrm{i}\omega_n - \mathrm{i}\omega_{n'}) - \mu] \\ \phi(\mathrm{i}\omega_n) &= \frac{\pi}{\beta}\sum_{n'} \frac{\phi(\mathrm{i}\omega_{n'})}{\Xi(\mathrm{i}\omega_{n'})} [\lambda(\mathrm{i}\omega_n - \mathrm{i}\omega_{n'}) - \mu] \end{aligned} \tag{2.97}$$

with

$$\Xi(\mathrm{i}\omega_n) = \sqrt{\omega_n^2 Z^2(\mathrm{i}\omega_n) + \phi^2(\mathrm{i}\omega_n)} \tag{2.98}$$

and the effective electron phonon coupling

$$\lambda(\mathrm{i}\omega_n - \mathrm{i}\omega_{n'}) = 2\int \frac{\omega\alpha^2 F(\omega)}{(\omega_n - \omega_{n'})^2 + \omega^2}\mathrm{d}\omega \tag{2.99}$$

that includes the electron-phonon spectral function $\alpha^2 F$, see Eq. (2.81). The averaged Coulomb interaction is defined by

$$\mu = \frac{1}{N(E_\mathrm{F})}\sum_{\boldsymbol{k}\boldsymbol{k}'} W_{\boldsymbol{k}\boldsymbol{k}'}\delta(\varepsilon_{\boldsymbol{k}} - E_\mathrm{F})\delta(\varepsilon_{\boldsymbol{k}'} - E_\mathrm{F}). \tag{2.100}$$

If the Coulomb interaction is purely local, $W_{\boldsymbol{k}\boldsymbol{k}'} = \overline{W}$, this leads to the simple formula[12]

[11] Details on the derivation of the Eliashberg equations can, for example, be found in Refs. [112] and [113].

[12] Note that in this effective way, Coulomb repulsion and BCS electron-phonon interaction are described very similar, see Eq. (2.89).

$$\mu = N(E_\mathrm{F})\overline{W}. \tag{2.101}$$

In the form of the Eliashberg theory presented in Eq. (2.97), the gap is defined by

$$\Delta(\mathrm{i}\omega_n) = \frac{\phi(\mathrm{i}\omega_n)}{Z(\mathrm{i}\omega_n)}. \tag{2.102}$$

Besides the effective electron-phonon interaction λ, see Eq. (2.83), there are two important quantities that are often used to describe the superconducting phase in Eliashberg theory, namely the effective or typical phonon frequency

$$\omega_\mathrm{log} = \exp\left[\frac{2}{\lambda}\int \alpha^2F(\omega)\frac{\ln(\omega)}{\omega}\mathrm{d}\omega\right] \tag{2.103}$$

and the retarded Coulomb potential, sometimes called Coulomb pseudopotential or Morel-Anderson parameter [114],

$$\mu^* = \frac{\mu}{1+\mu\ln\left(\frac{E_\mathrm{F}}{\omega_\mathrm{log}}\right)}. \tag{2.104}$$

The latter takes care of the fact that the static Coulomb repulsion between electrons is reduced due to the retardation of the electron-phonon interaction. Commonly, μ^* is assumed to be in the range $\mu^* = 0.1 - 0.2$, but it can also have significantly different values, see Sec. (5.1.3).

McMillan and Allen-Dynes approximation

In this thesis as well as many other works on electron-phonon superconductivity, approximative formulas for the critical temperature are used instead of solutions to the full Eliashberg equations. We use the formula by Allen and Dynes [115], which is an improvement of the work by McMillan [116]. The latter employed fits to numerical results for Nb that lead to the expression for the critical temperature

$$T_\mathrm{c} = \frac{\Theta_\mathrm{D}}{1.45}\exp\left[\frac{-1.04(1+\lambda)}{\lambda(1-0.62\mu^*)-\mu^*}\right] \tag{2.105}$$

where Θ_D is again the Debye temperature, λ is calculated via Eq. (2.83), and μ^* is calculated via Eq. (2.104). The improvement by Allen and Dynes led to

$$T_c = \frac{\hbar\omega_{log}}{1.2\, k_B} \exp\left[\frac{-1.04(1+\lambda)}{\lambda(1-0.62\mu^*)-\mu^*}\right] \tag{2.106}$$

where the phonon frequency ω_{log} is calculated via Eq. (2.103). Allen and Dynes used a value of $\mu^* = 0.1$ for all metals. The exponential dependence on λ was previously also found by solving the BCS equations. Taking an effective coupling of $\lambda_{eff} = (\lambda - \mu^*)/(1+\lambda)$ approximately recovers the BCS equation for the critical temperature (2.88).

The use of three rather simple parameters and the simplified calculation of the critical temperature led to the success of the above equations for T_c and to the fact that they are often used synonymously with Eliashberg theory. However, they suffer from some severe limitations. Among these is the fact that they cannot account for anisotropy in the coupling and, thus, in the gap function or the critical temperature. Additionally, the calculation of the effective phonon frequency via Eq. (2.103) is no longer possible for a non-vanishing electron-phonon coupling and a non-zero $\alpha^2F(\omega)$ at frequencies $\omega \leq 0$, and the equations for the critical temperature are not applicable in this case.

3. Electronic properties of two-dimensional materials

Two-dimensional materials have received a lot of scientific attention in recent years. In contrast to earlier discussions of the properties of quasi-two-dimensional situations like surfaces or interfaces [117], purely 2D materials consisting of a single atomic layer can now be produced experimentally by exfoliation via the scotch-tape technique [3] or on a larger scale by chemical vapor deposition [118]. Not only are these materials important when it comes to studying fundamental physics, but they can also be utilized to make ultrathin devices for the use in such fields as (opto)electronics, catalysis or photovoltaics [119, 120]. Here, we show only a few aspects of the properties of these materials relevant for the work presented in the later parts of the thesis. Detailed discussions for both graphene and the transition metal dichalcogenides can be found in the literature, e.g. in Refs. [9, 121, 122].

3.1. Transition metal dichalcogenides

Transition metal dichalcogenides (TMDCs) have the chemical formula MX_2, with the monolayers consisting of a layer of transition metal atoms M sandwiched between two layers of chalcogen atoms X. The lattice structure is similar to the honeycomb lattice of graphene, see Sec. 3.2, with the transition metal atoms on one sublattice and the chalcogen atoms on the other in the 2H phase. Thus, the inversion symmetry is broken in monolayer TMDCs. About 40 different TMDCs exist [123]; we focus on the six materials with Mo, W and Nb as a transition metal and S or Se as a chalcogen and only deal with the 2H phase as depicted in Fig. 3.1. In this thesis, we do not discuss the 1T phase where the positions of the chalcogen atoms change and TMDCs that are semiconducting in the 2H phase exhibit metallic character; for a comprehensive discussion of the electronic structure of many TMDCs in both phases see for example Ref. [124].

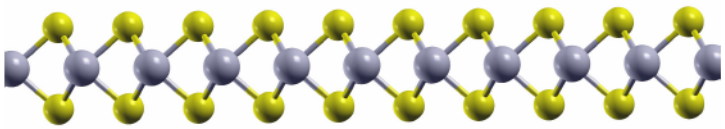

Figure 3.1.: Structure of a TMDC in the 2H phase. The chalcogen atoms are colored yellow, the transition metal atoms are colored grey.

One example for the practical use of TMDCs that has been studied for a rather long time are lubricant applications, where MoS_2 was investigated most intensively [125]. Recently, due to the possibility of creating thin layers and the variety of opportunities for functionalization, tuning, and combination that is inherent to low-dimensional materials [126], a lot of other applications have been proposed and are a major topic of research [127, 128]. They include the use in photovoltaic and other devices for energy conversion and storage [129–131] and in digital electronic devices such as field effect transistors [7, 132, 133] as well as several other physical, chemical and industrial fields, especially upon doping [134].

3.1.1. Density of states and band structure

While the electronic properties of the TMDCs can encompass a wide range from semiconducting to superconducting [120], their basic descriptions like the band structure look similar. Here, we demonstrate some of the typical and important features of these basic electronic properties using the example of $MoSe_2$; instabilities like superconductivity and CDWs are discussed later on in chapter 5.

First we look at the density of states (DOS) as obtained from DFT calculations[1], see Fig. 3.2. The DOS shows sharp features at the van-Hove singularities, which we will discuss in more detail later on, as well as at the band edges, and has values in the range between 2 and $5\,\mathrm{eV}^{-1}$ otherwise. Its 2D character is obvious in the lower picture of Fig. 3.2, where one can clearly see the singularities around 0.4 eV, and in the steps above 3 eV and around 0 eV in the upper picture. These steps arise because two-dimensionality leads to a constant DOS for a single electronic valley which can be described by a quadratic dispersion, in constrast to the square root shape of the DOS in 3D. This is the case here: below $E_\mathrm{F} < 0.15\,\mathrm{eV}$, only the valley around the K point in reciprocal space is relevant

[1]For details on the parameters in these and other calculations, see Appx. A. The Fermi energy is set to the minimum of the conduction band in all pictures for undoped, i.e., semiconducting $MoSe_2$.

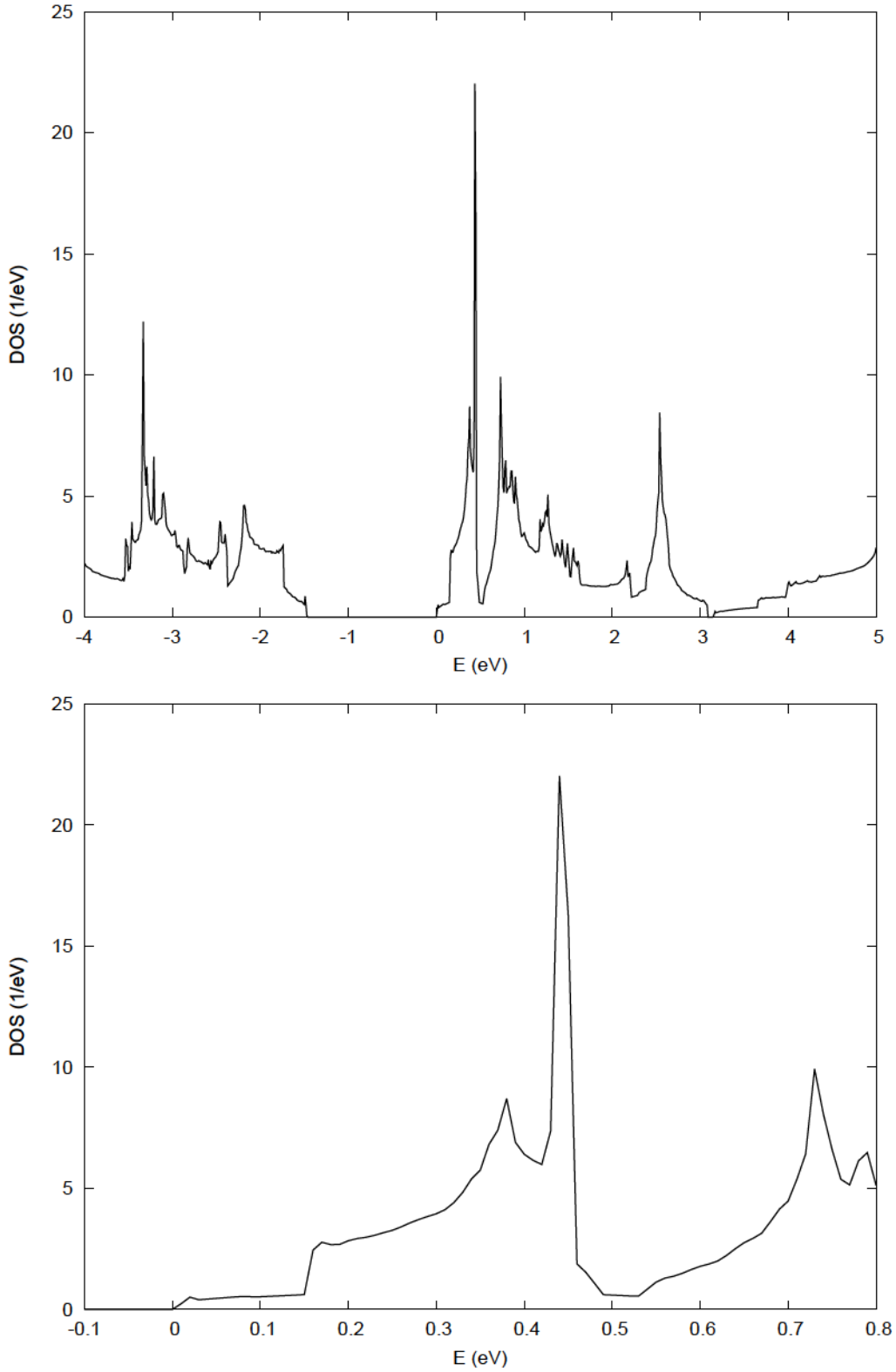

Figure 3.2.: (Top) Density of states for $MoSe_2$ obtained using the tetrahedron method [135]. (Bottom) Closer look at the densitiy of states of the lowest conduction bands.

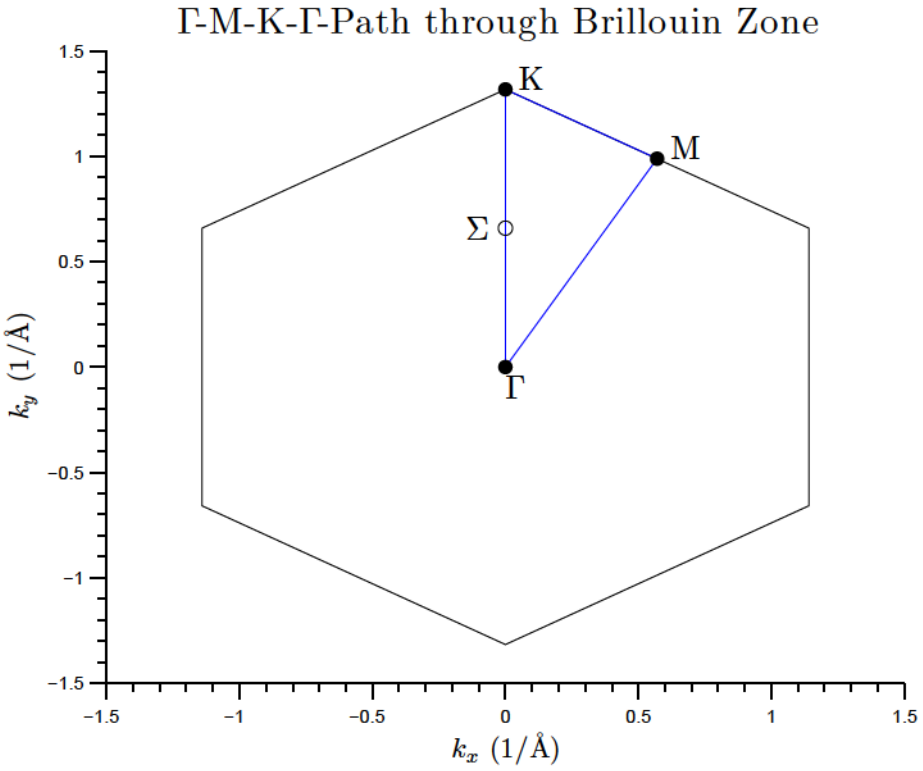

Figure 3.3.: Path through the 2D-Brillouin zone including high symmetry points. Taken from [113].

and the density is constant $n \approx 0.5\,\mathrm{eV}^{-1}$. Above this energy, both K- and Σ-valleys are relevant and $n \gtrsim 2.5\,\mathrm{eV}^{-1}$.

Next, we plot the electronic bands along the high symmetry path through the first Brillouin zone shown in Fig. 3.3. The full band structure of $MoSe_2$ is depicted[2] in Fig. 3.4. The bands of inner shell electrons lie at 14 eV below the Fermi energy and lower. At higher energies, one can identify a set of outer shell valence bands between -7 eV and -2 eV. Above the Fermi level we see four conduction bands. Between the six TMDCs discussed in this thesis, the most important differences in the band structure are the position of the Fermi energy, which lies in the band gap for the semiconductors and in the upmost valence band for the metals, and the position of the highest valence band. This valence or conduction band is more or less *entangled* with the lower valence bands;

[2]Please note that we used a GGA potential for $MoSe_2$ since this yields the direct band gap in the monolayer which was found experimentally [136]. A LDA potential would yield an indirect band gap. For every material we use a potential that yields a reasonable electronic structure and makes the calculation run smoothly, see Appx. A.

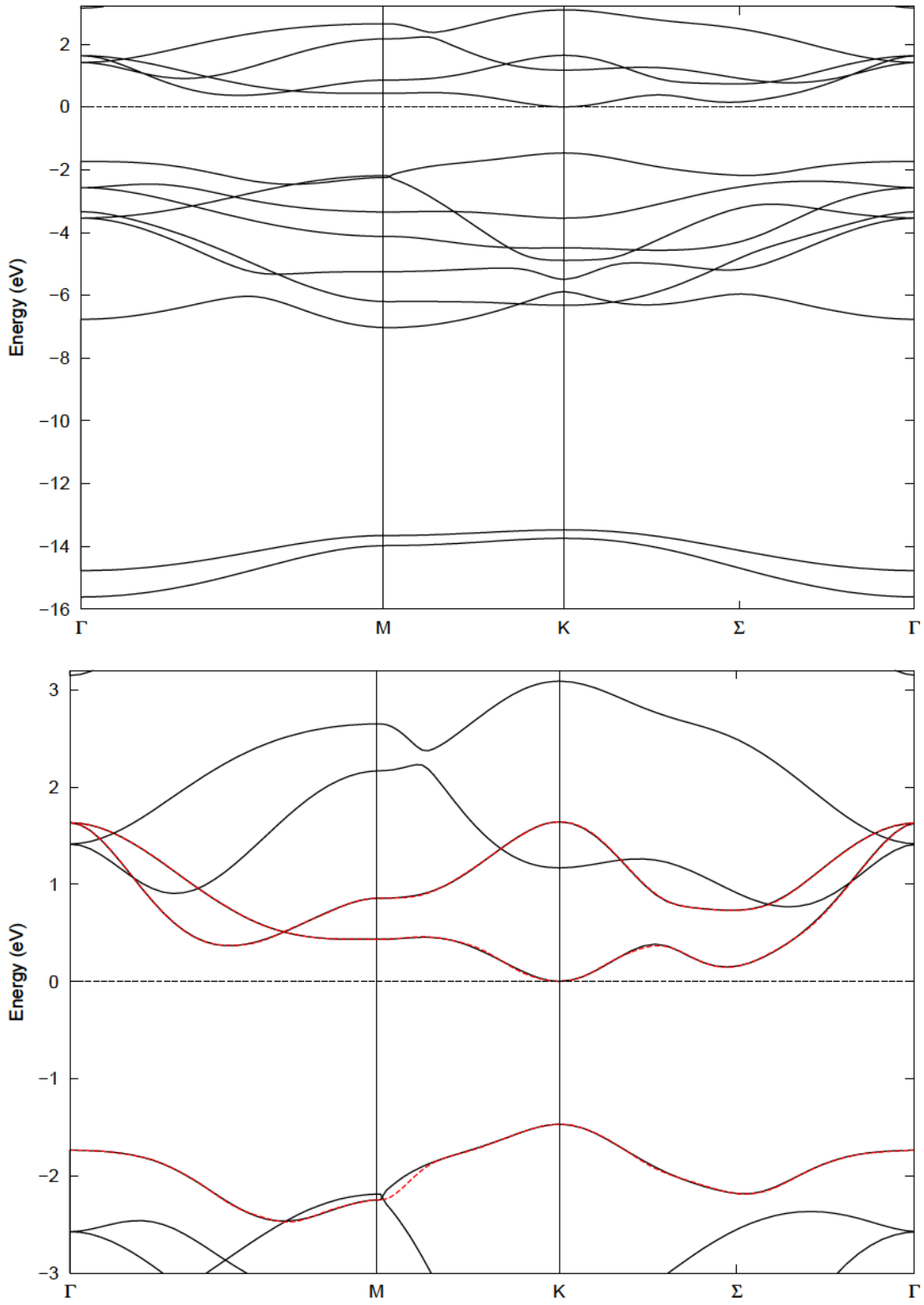

Figure 3.4.: (Top) Full band structure of $MoSe_2$. (Bottom) Bands around the Fermi level. The red lines show the Wannier model of the three important bands around the Fermi level as described in Sec. 3.1.2.

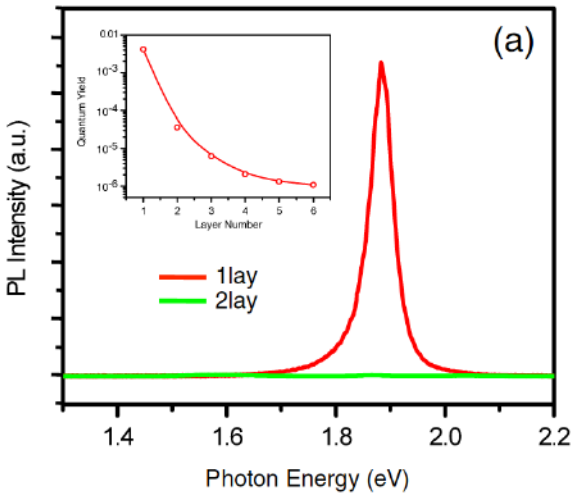

Figure 3.5.: Experimental result for the photoluminescence of MoS_2. The peak in the intensity in the monolayer limit signals a change from an indirect do a direct semiconductor with decreasing layer number. Picture taken from [137].

for example, it is not seperated from the lower bands in $MoSe_2$, see Fig. 3.4, while it is clearly decoupled from these bands in NbS_2, see Fig. 3.9.

Semiconductors

The four materials considered here, MoS_2, $MoSe_2$, WS_2 and WSe_2, are all indirect semiconductors in the bulk and few-layer systems, while they become direct semiconductors in the monolayer limit, which was first found experimentally for MoS_2 by Mak et al., see Fig. 3.5. The optical band gap[3] is between 1.5 and 2 eV [136, 137, 139]. The change from an indirect to a direct band gap happens due to quantum confinement [15, 140] which influences the maxima of the valence band at K and Γ as well as the minima of the conduction band at K and Σ; it can be experimentally observed in photoluminescence spectra [141].

The instabilities of superconductivity and CDWs that are discussed in chapter 5 can of course only arise in a metallic system, or rather a system with free conduction electrons. Metallic phases can be established in the semiconducting TMDCs via chemical doping as well as field effect gating [126]. In our DFT calculations, we do not explicitly consider chemical doping and limit ourselves to an effective treatment of the doping by including

[3] One has to bear in mind that the electronic band gap seen in our figures of the band structure is well known to be underestimated by DFT calculations; better results are obtained using *GW*-calculations, see for example [138].

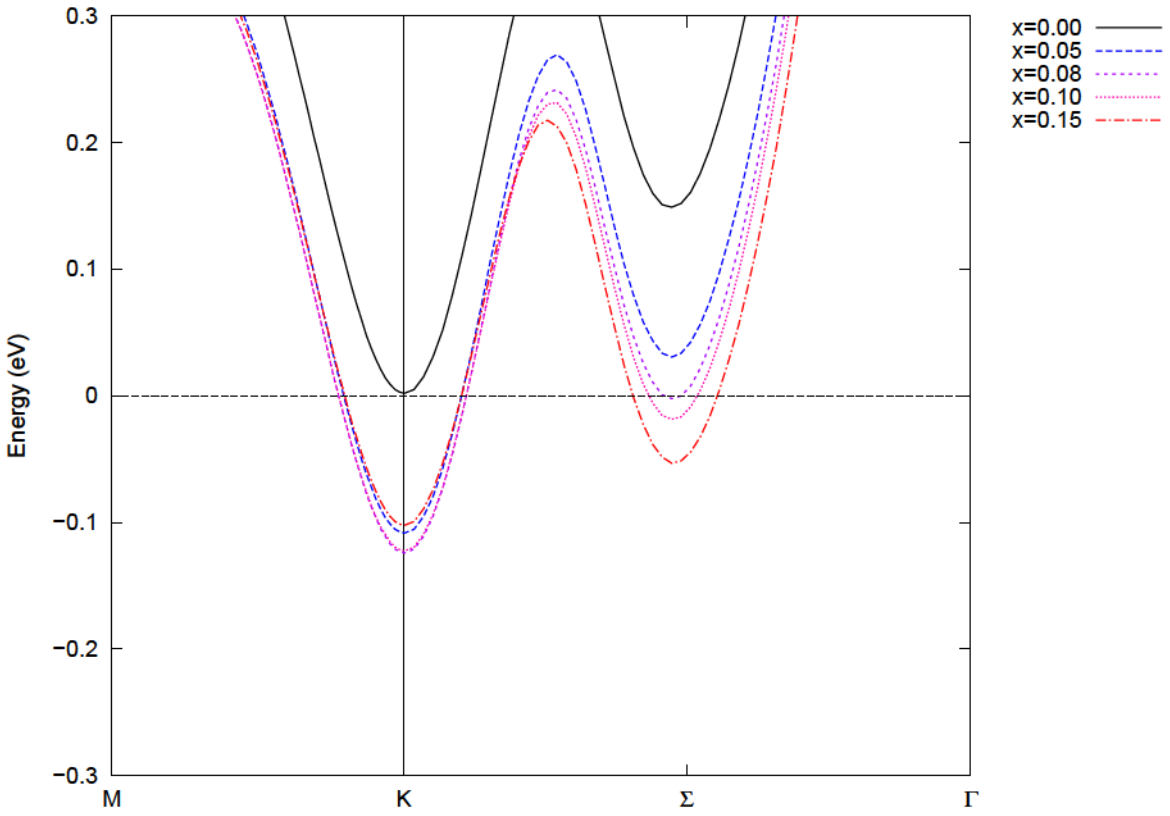

Figure 3.6.: Change of the band structure at the Fermi level with electron doping x for $MoSe_2$. The Lifschitz transition towards a larger number of Fermi pockets happens around $x = 0.08$.

a non-zero total charge that is compensated by a jellium background [cf. Eq. (2.13)]. This effective electron doping[4] x leads to a change of the Fermi level as well as the valley structure of the conduction bands as can be seen in Fig. 3.6. The lowest conduction band has two prominent minima at the K-point and the point $\Sigma = \frac{1}{2}\overline{\Gamma K}$ in reciprocal space. The valleys at both points have parabolic dispersions close to the minima, which makes an effective mass description possible, see Refs. [113, 142]. Upon electron doping, first the valleys at the K-points and afterwards the Σ-valleys are filled with electrons. This Lifschitz transition [143] to a larger number of Fermi pockets is depicted in Fig. 3.7. Its importance, for example concerning the superconducting phase, is discussed later on in this thesis. The value of the critical doping at which the transition takes place is approximately $x_{\text{xrit}} = 0.08$ for $MoSe_2$ in DFT, but can be different for the other TMDCs. In general, the values lie between $x = 0.05$ and $x = 0.10$.

[4]The doping is always quantized as the amount of additional electrons x per unit cell.

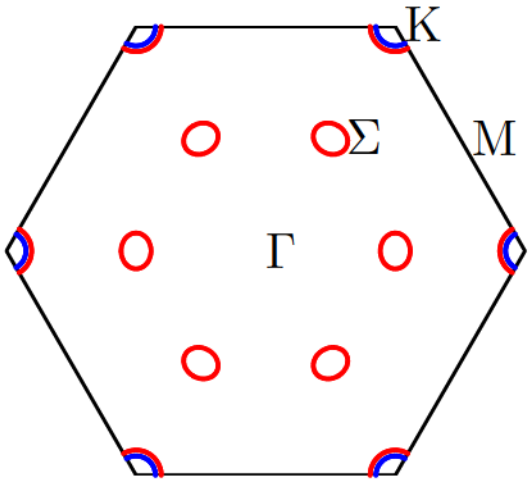

Figure 3.7.: Schematic picture for the change of the Fermi surface with electron doping in the semiconducting TMDCs if no spin-orbit coupling is included. Blue is *low* doping while red shows *high* doping.

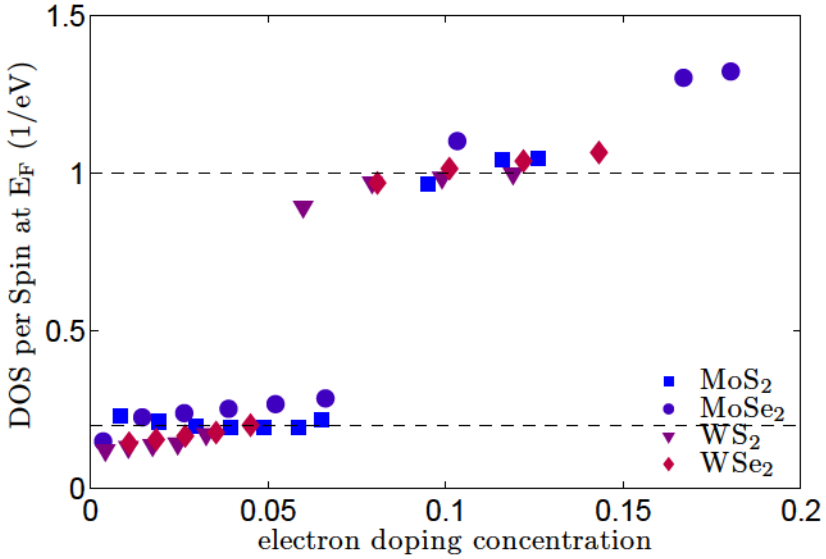

Figure 3.8.: Development of the density of states at the Fermi energy with electron doping in several TMDCs. Data is obtained from calculations involving the Wannier models described in Sec. 3.1.2. The two dashed lines represent values of 0.2 and 1.0, respectively.

From Fig. 3.6 one can further see that the two minima experience not only a shift with respect to the Fermi energy, but also a relative change of their positions. The latter change will be included in the phonon calculations in Sec. 5.1, but not in our calculations on the Coulomb interaction presented in Secs. 4.3, 4.4, 5.1.3, and 5.3. Whether the treatment of the doping as a rigid shift done there is justified can be questioned and will be discussed in the respective sections.

Lastly, we look at how the DOS at the Fermi level $N(E_\mathrm{F})$ changes upon electron doping for the different semiconducting TMDCs, see Fig. 3.8. The Lifshitz transition is obvious in this picture, with a change of $N(E_\mathrm{F})$ at the transition from ~ 0.2 per eV and spin to $\gtrsim 1.0$ per eV and spin in all four materials. Where exactly the transition occurs depends, however, on the specific material. Furthermore, the concrete values change slightly, with $N(E_\mathrm{F})$ being generally a little larger in $MoSe_2$ and lying below 0.2 in the tungsten materials at low doping.

As a side note, we mention that no spin-orbit coupling (SOC) is discussed in this thesis. SOC can be strong in TMDCs with splittings between 150 and 500 meV at the top of the valence band at the K point and is much stronger in tungsten based materials than in molybdenum based materials because of the larger atomic mass [144]. Furthermore, combining spin and valley degrees of freedom can be useful for studying physics and applications [145].

Metals

For the metallic TMDCs $NbSe_2$ and NbS_2, we have a half filled lowest conduction band which has a similar structure to the highest valence bands in the semiconducting materials. Its structure is shown for NbS_2 in Fig. 3.9. Since the materials are already metallic, we do not discuss the effects of doping. The Fermi energy lies close to the van-Hove singularity [146] that occurs at the M-point of the Brillouin zone where the electronic dispersion is flat and has a vanishing derivative. This singularity shows up as a large peak in the density of states, which can have profound effects on the screening and other properties of the material.

Fig. 3.10 shows the Fermi surface of NbS_2. We can identify rather large Fermi pockets around Γ and each K point. At the K points, the pockets have an ellipsoidal shape while the shape is circular around Γ.

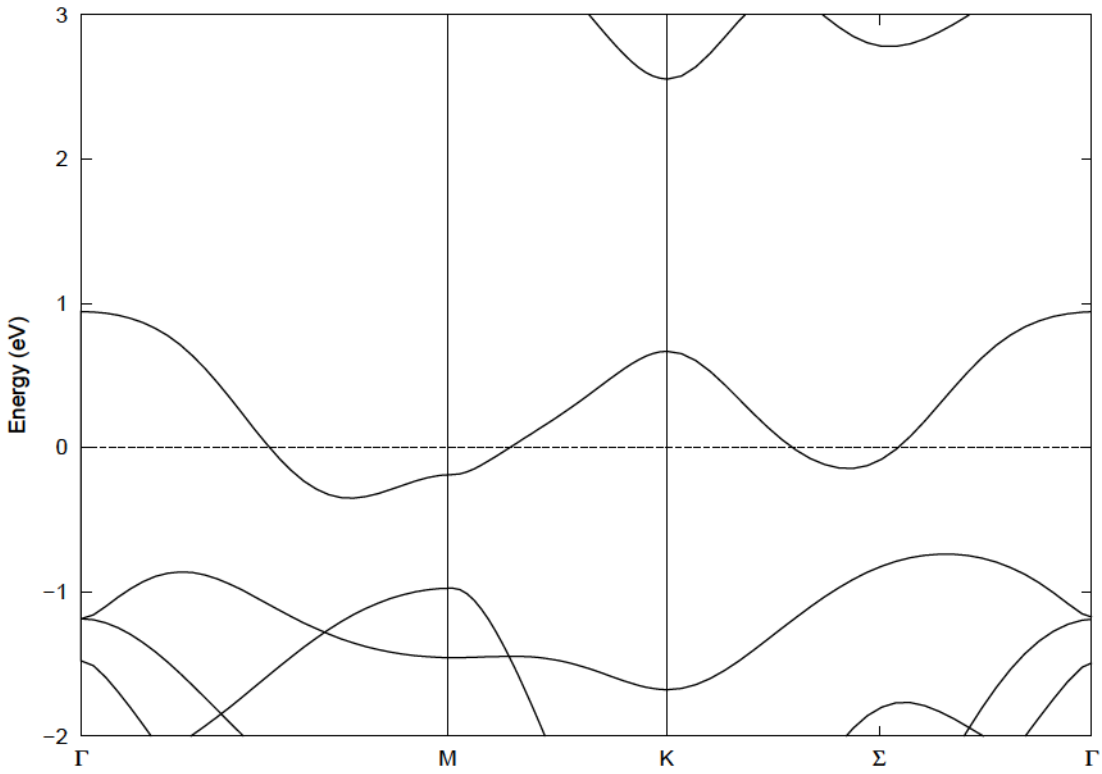

Figure 3.9.: Band structure of the half filled conduction band and surrounding bands for undoped NbS_2.

3.1.2. Minimal three-band model

In order to obtain a model that is at the same time material realistic and easy to handle, we turn to the question whether a simplified description of the band structure is possible. Superconductivity and other low-energy physics considered in this thesis mainly take place close to the Fermi level. For the TMDCs, Figs. 3.4 and 3.9 show that essentially only three bands are relevant to describe the electronic dispersion in this area. As was previously shown in Refs. [73, 147, 148], these three bands arise from the d-orbitals of the M-atoms for the TMDC MX_2. Fig. 3.11 shows that they can be efficiently described using only the d_{z^2}, d_{xy} and $d_{x^2-y^2}$ orbitals. Thus, to get a simple and accurate model for the three important bands of each TMDC, we employ a Wannier construction which includes only these three orbitals. The tight-binding hopping matrix elements are obtained from projections of the results for the DFT band structure onto the three orbitals. We use a disentanglement procedure inside of an outer energy window, but do not involve the maximal localization scheme in order to preserve the symmetry and orbital character (see Sec. 2.1.6 and [52]).

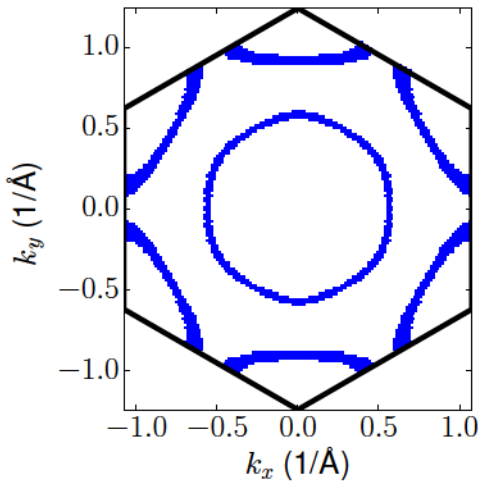

Figure 3.10.: Schematic picture of the Fermi surface of undoped NbS_2. The black lines correspond to the boundaries of the first Brillouin zone.

An example of the resulting three-band structure is depicted for $MoSe_2$ in Fig. 3.12. Wannier models were obtained for the other five TMDCs as well. While the construction of these models is very accurate if the highest valence band is not entangled with the lower valence bands, as it is the case for example in NbS_2, see Fig. 3.9, problems can arise and the description can be inaccurate at certain points in reciprocal space for the case of entangled valence bands. As can be seen in Fig. 3.4 (Bottom), these inacurracies are overall still small for the band structure of $MoSe_2$ and mainly present around the K and Σ points as well close to the crossing bands at the M point. The Wannier models described here are used for the calculations involving the Coulomb interaction in Secs. 4.4, 5.1.3, 5.3, and 5.4.

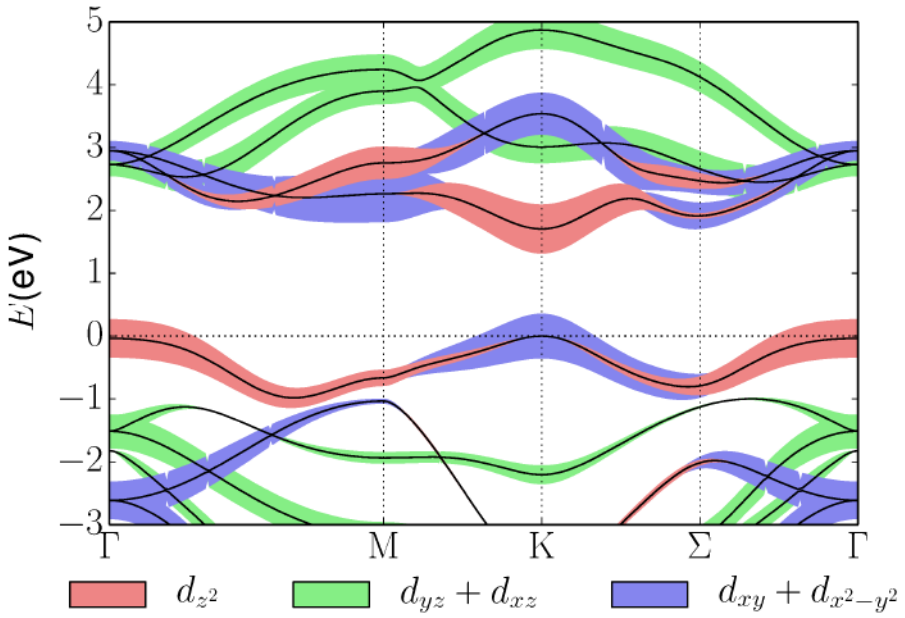

Figure 3.11.: Band structure and orbital characters for MoS_2; picture by Malte Rösner, [73].

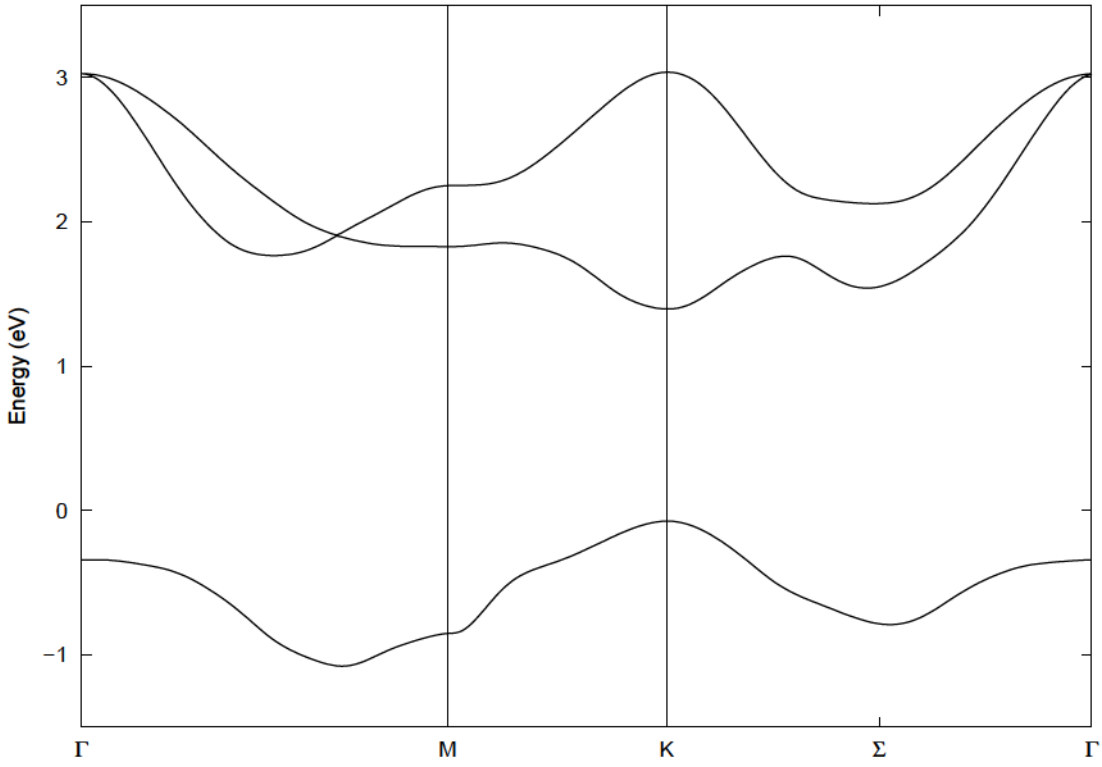

Figure 3.12.: Electronic dispersion from three-band Wannier model for $MoSe_2$.

3.2. Functionalized graphene

The isolation of carbon as a stable, purely two-dimensional monolayer called graphene was first performed by Novoselov et al. [2, 3]. It led to a lot of research on graphene and to the discovery of such interesting physics as exorbitant mechanical strength, very large intrinsic mobility and Dirac electrons [10, 149, 150]. Besides the insight into fundamental physics that can be gained from the example of graphene, there have also been a lot of proposals to use the material in electronic, photonic or other applications [151, 152].

In graphene, the carbon atoms are arranged in a honeycomb lattice structure with two different sublattices. Pristine graphene can be viewed as a semiconductor with a vanishing electronic gap. Directly at the Fermi level, electrons obey a linear dispersion, called the Dirac cone, and the low-energy quasiparticle excitations can be described via an effective Hamiltonian for massless Dirac fermions [9, 151]. This unusual electronic dispersion is one of the reasons for the strong interest in graphene.

Because of the absence of a band gap, some optical and other applications are not possible in pristine graphene. As a result, a lot of research has been focussed on searching for a graphene related material with a sizeable band gap. This has lead to the experimental and theoretical work on several functionalizations of graphene, where hydrogenated graphene, called graphane [153], and fluorinated graphene, called fluorographene [154], are two of the most common examples.

As mentioned earlier in Sec. 2.6.1, hydrogen is especially interesting for superconducting compounds. Due to their low atomic mass, hydrogen atoms lead to large phonon frequencies which can result in large critical temperatures of the superconducting phase, cf. Eqs. (2.69) and (2.90). For example, critical temperatures of up to 203 K were recently found in sulfur hydrides [107]. The possibility of high critical temperatures is one reason for us to discuss the example of partially hydrogenated graphene C_8H_2 in this thesis. Additionally, this structure is especially interesting since it can be produced experimentally [156] and leaves the side of graphene that is not occupied by hydrogen atoms open for further tuning or functionalization.

We use the geometry that was described for the undoped system in Ref. [155] with the parameters of the calculations given in Appx. A.2. In this material, the two hydrogen atoms per supercell are on the same side of the graphene layer and occupy the opposite sides in a hexagon, so that they are on different sublattices, see Fig. 3.13. The system can be described as an arrangement of C_6 hexagons connected by CH molecules. We

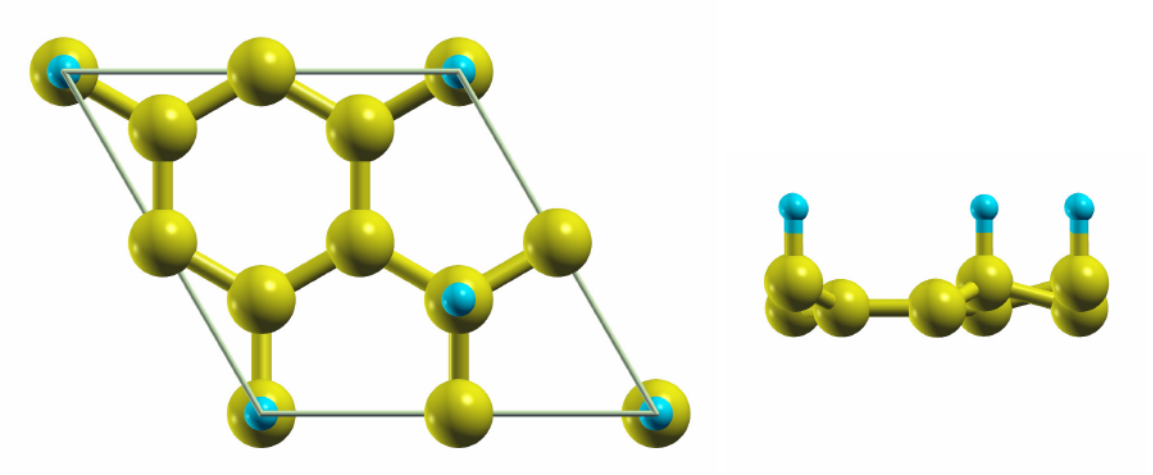

Figure 3.13.: (Left) Unit cell of functionalized graphene C_8H_2 that we use for our calculations with carbon atoms in yellow and hydrogen atoms in blue. Wehling et al., [155], calculate this to be the geometry realized for low doping concentrations. (Right) Side view showing the relaxed z-positions of the atoms.

do not fully relax the atomic structure, but only relax the z-position to preserve this symmetry[5], see Fig. 3.13. Due to this approach, the C_8H_2 structure described in this thesis is metastable, as can be seen from the phonon dispersions in Sec. 5.2.

3.2.1. Band structure

While pristine graphene is a semiconductor with a vanishing band gap, the functionalization with hydrogen atoms opens up a band gap of several eV. In the electronic dispersion obtained from our DFT calculations, we see two high valence bands and two lower conduction bands, separated by an indirect band gap of 3.4 eV, see Fig. 3.14. Both bands are rather flat, while the surrounding lower valence and higher conduction bands have a stronger dispersion that is quadratic around Γ. The most discussed features of the typical graphene band structure, i.e., the Dirac cone and the π-bands, are pushed upwards in energy by more than 3 eV as a result of the functionalization with hydrogen atoms and hybridization.

Next, we discuss the effects of doping, and look at the case of electron doping first, see Fig. 3.15. We see that for small electron doping levels $x = 0.1$ per super cell of C_8H_2,

[5] A fully relaxed atomic structure would, among other effects, lead to computational problems such as very long time scales in the calculation of the phonon dispersion and the electron-phonon interaction, see Fig. 5.11. This is due to the fact that the q-mesh of the phonon calculation can be reduced if the system has a high symmetry, cf. Appx. A.2.

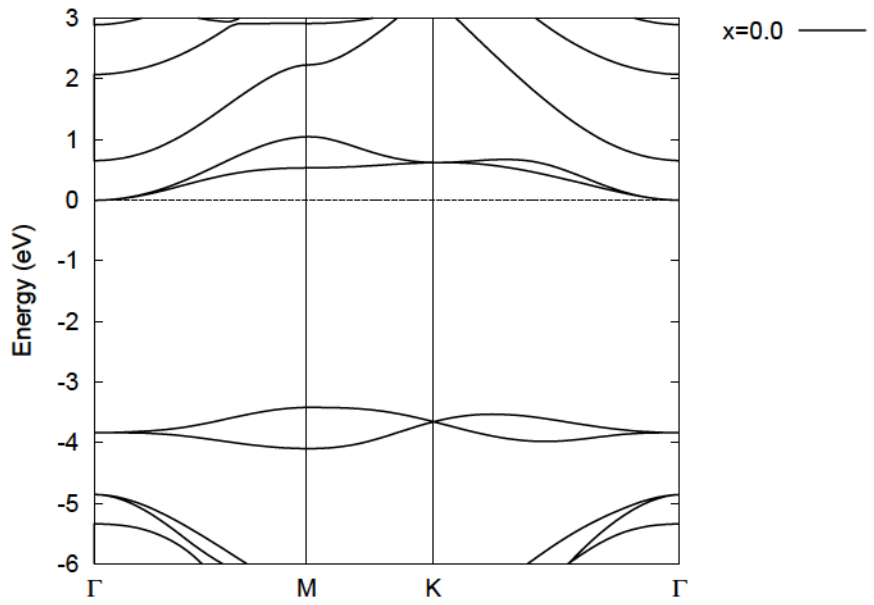

Figure 3.14.: Band structure of C_8H_2 without doping from DFT calculations.

two degenerated Fermi pockets around Γ exist. For larger concentrations, an additional pocket appears, stemming from a quadratic band that is rapidly pushed downwards with increased doping. It hybridizes with the two lowest, formerly separated conduction bands and additional electrons mainly occupy this band for $x \gtrsim 0.2$. Thus, a Lifshitz transition like the one that was already observed in the semiconducting TMDCs upon doping occurs here, too.[6]

Upon hole doping, the situation is a little different. Due to flat dispersion and the resulting high density of states at the M-point maximum, already small changes in the Fermi level require a rather large doping level, so that one needs $x \sim 0.3$ removed electrons to get a clear hole pocket around the valence band maximum, see Fig. 3.16. Further hole doping changes the shape of the two valence bands and leads to another Lifshitz transition at $x \sim 0.9$ where additional pockets appear at a point between K and Γ in reciprocal space.[7] The dispersion around this point is also rather flat and similar to a van-Hove singularity.

As a last step, we look at the orbital character of the relevant valence and conduction

[6] See the discussion at the end of this section.

[7] It is important to note that in Ref. [155], $x < 0.4$ electrons per super cell or $x < 0.05$ electrons per carbon atom was calculated to be the regime where the C_8H_2 structure discussed here is the equilibrium geometry. Furthermore, we do not take into account chemical doping which could experimentally be necessary to achieve such high doping concentrations as $x \sim 0.9$ holes or electrons. Thus, the results for large electron or hole doping presented here have to be taken carefully.

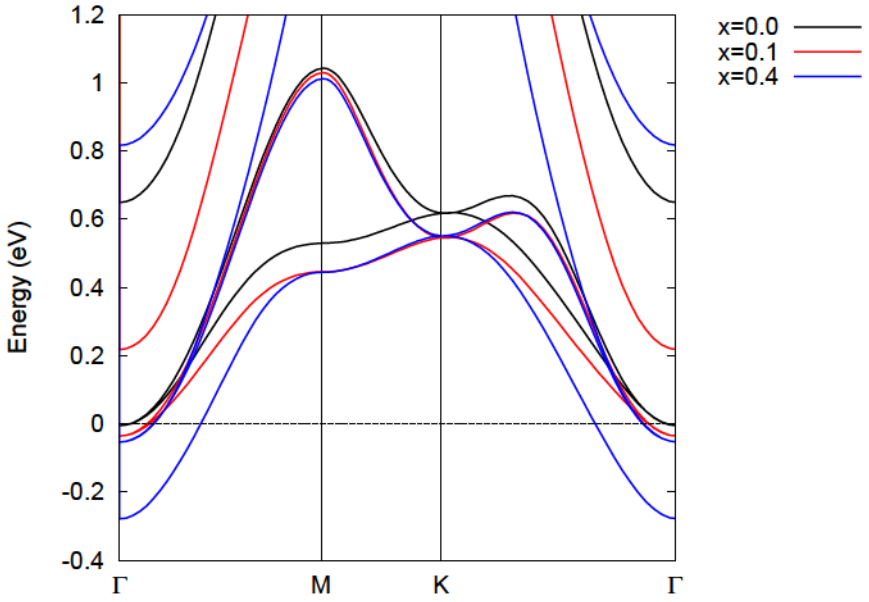

Figure 3.15.: Band structure of the conduction bands in C_8H_2 under electron doping x per super cell.

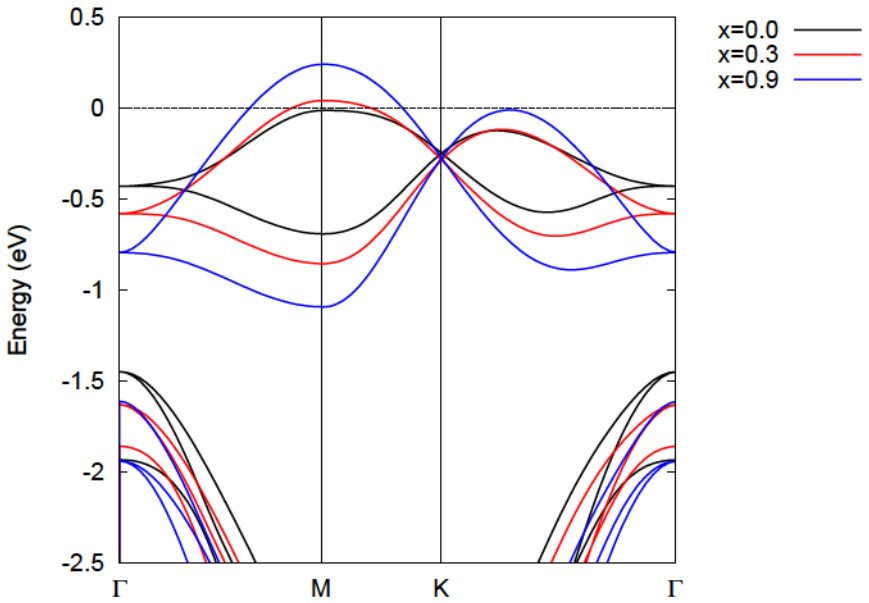

Figure 3.16.: Band structure of the valence, i.e., partially filled bands in C_8H_2 under hole doping x per super cell.

bands. These bands are composed of the p-orbitals of the carbon atoms as well as the s-orbitals of the hydrogen atoms. In Fig. 3.17, one can see that the p_x- and p_y-orbitals have only a small contribution, mainly for small wave vectors around Γ, while the hydrogen s-orbitals are present for larger wave vectors. Most of the orbital character of the considered bands, however, stems from the carbon p_z-orbitals. This means that in the case of electron doping into the conduction bands, only the carbon p-orbitals are relevant, especially because the band that is pushed downwards in energy has only p_z-character. Upon hole doping, only the p_z-orbitals and the hydrogen s-orbitals play a role since the hole pockets arise at the M point and between Γ and K.

One important issue that has not been adressed so far is the problem of nearly free electrons with quadratic bands. One might ask if electron dopings beyond the Lifshitz transition in C_8H_2 just fill these quadratic bands. We can state that from our calculations of the orbital character as shown in Fig. 3.17, the band that is pushed downwards and filled with electrons still has a well defined orbital p_{z^2}-character which means that it should not belong to nearly free electrons. Still, by using only data from our DFT calculations, we cannot decide whether the observed Lifshitz transition is an artifact of our calculations; furthermore, the transition may occur at a different doping level in experiments.

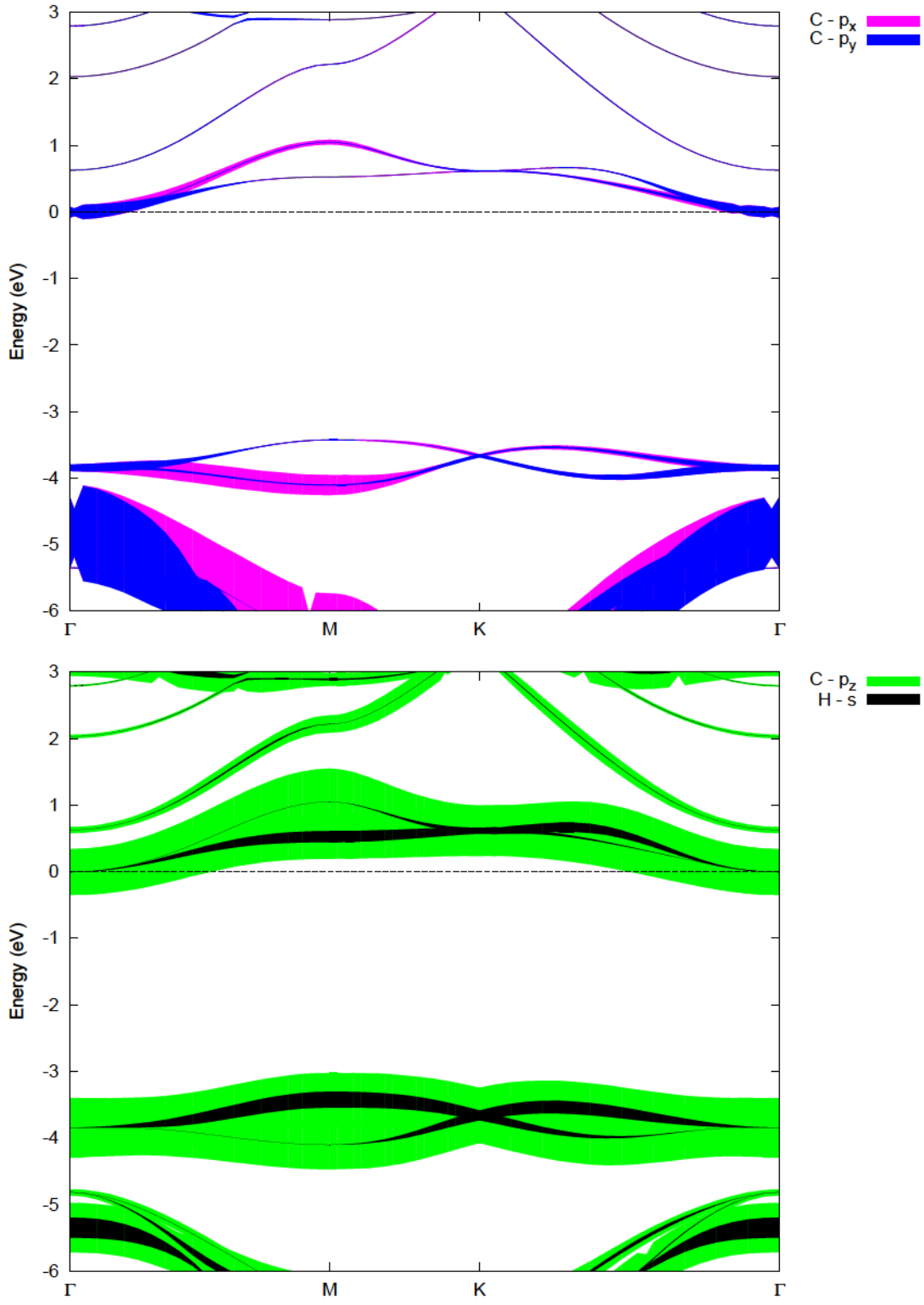

Figure 3.17.: Band structure of C_8H_2 without doping. (Top) Weight of the p_x- and p_y-orbitals of the carbon atoms. (Bottom) Weight of the p_z- orbitals of the carbon atoms and s-orbitals of the hydrogen atoms.

4. Quantification of Coulomb interaction and screening in TMDCs

In this chapter, we present our model for the Coulomb interaction and focus on 2D TMDCs. The other material class of interest to us, (functionalized) graphene, was already investigated in Refs. [34, 81] and is discussed in Secs. 3.2 and 5.2 concerning its electronic and phononic properties, respectively.

As mentioned in the introduction, the Coulomb interaction in TMDCs and its effects, especially on the many-body properties of the materials, are not well understood. On the other hand, the interaction influences a lot of properties like superconducting order, charge order and spin order more or less strongly. In order to be able to describe these properties in chapter 5 and account for the influence of the interaction, we need a material-realistic description. Furthermore, this detailed and quantitative description of the interaction is important to examine the general claim of a strong Coulomb interaction in two dimensions.

Here, we first make some remarks on why the Coulomb interaction can be different in 2D compared to 3D materials. The main part of this chapter follows in Sec. 4.2 where we give details on our fitting procedure and present the results for the Coulomb interaction. Although the details of this scheme can be technical, they are important to understand the advantages and shortcomings of our approach. Afterwards, we show results for the screening in both semiconducting and metallic systems and discuss the plasmonic spectra or Electron Energy Loss Spectra (EELS) of the TMDCs.

4.1. Coulomb interaction in two dimensions

As already mentioned, the Coulomb interaction in 2D materials can behave qualitatively and quantitatively different compared to three-dimensional bulk materials. The most obvious difference is probably the possibility to influence the interaction inside of the layer from outside by changing the dielectric environment. In a simplified picture, this can be understood by the fact that the field lines of the interaction between two seperated charges do not only pass through the layer, but also enter the environment, see Fig. 4.1; this effect is stronger the larger the distance between the two charges is.

If the material is surrounded by vacuum, this means that especially the long-range part of the dielectric screening is reduced compared to the bulk case, which in general leads to an enhanced Coulomb interaction. On the other hand, we can put the material into a dielectric environment and in this way enhance the screening. If we enclose the layer for example in a metallic environment, this could even reduce the interaction to values lower than those for the bulk. Since experiments on 2D materials are usually done on substrates, it is important to include substrate effects in our calculations to get comparable results. Beyond that, substrates can be used to functionalize materials and tune their properties. One example is the creation of heterostructures with a spatially changing band gap, see Ref. [31].

In reciprocal space, the bare Coulomb interaction is also different to three dimensions because the Fourier transform of the $1/r$-potential leads not to a $1/q^2$ dependence as in 3D, see Eq. (2.46), but rather to a $1/q$ dependence, see Eq. (2.47). This different behaviour will be used in the following section to obtain fitting models to the ab-initio results for the Coulomb interaction.

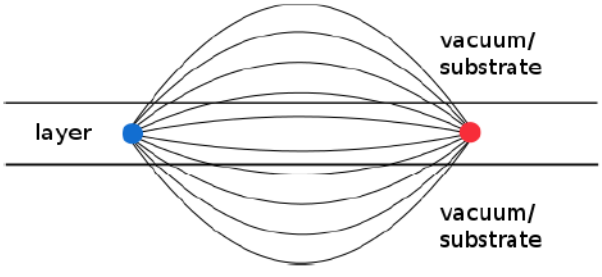

Figure 4.1.: Electric field lines between two charges in a two-dimensional layered material. Picture by Malte Rösner, edited by the author.

4.2. Fits to ab-initio Coulomb interaction

In this section, we present our fitting routine for the Coulomb interaction in 2D TMDCs. To get an accurate, yet simple model describing the interaction in the relevant bands around the Fermi energy, we employ the three-band model described in Sec. 3.1.2. The dielectric screening and Coulomb interaction of the materials discussed in this thesis was in parts also investigated in Refs. [157, 158].

Instead of using a fit routine, one could, in principle, also directly use the ab-initio values of the Coulomb interaction to describe its influence on the many-body properties, similar to our use of the onsite interaction in Sec. 5.4.3. Yet, our approach has several advantages: with the fit model, we obtain a description of the Coulomb interaction that is easier to interpret and to handle than the ab-initio data. Furthermore, it is very difficult and computationally demanding to include the effects of dielectric environments and doping in the ab-initio calculations, while this is much easier using the fit model. Lastly, in combination with the Wannier Hamiltonian (cf. Sec. 3.1.2), we obtain a simple description of the TMDCs that can be interpolated on arbitrary wave-vector grids.

4.2.1. Fitting procedure

Simple Model

Most of the fitting procedure presented here was described and published by the author in Ref. [159]. Additionally, parts of our calculations on and parametrization of the Coulomb interaction in MoS_2 were previously described in Ref. [142]. Here, we follow a similar procedure and make use of the Wannier function continuum electrostatics approach (WFCE) developed by Malte Rösner et al., [81], to include the screening effects of substrates, as described in the following.

The results for the bare and the interband screened interaction are obtained via *GW* (see Sec. 2.4) and RPA or cRPA calculations (see Secs. 2.3.1 and 2.3.2) using the Spex software code [82, 83] on the basis of DFT calculations in FLEUR [62]. Details on the procedure and the parameters for these calculations can be found in Appx. A.1.2.

In a first step, the bare interaction matrix $U_{\alpha\beta}(q)$ in the basis consisting of orbitals $\alpha, \beta \in \{d_{z^2}, d_{xy}, d_{x^2-y^2}\}$ of the transition metal atoms is obtained for the freestanding

undoped material. To parametrize the Coulomb interaction, we use the sorted eigenbasis of the bare interaction to diagonalize the latter

$$\mathbf{U}^{\text{diag}}(q) = \begin{pmatrix} U_1^{\text{diag}}(q) & 0 & 0 \\ 0 & U_2^{\text{diag}} & 0 \\ 0 & 0 & U_3^{\text{diag}} \end{pmatrix}. \tag{4.1}$$

Here, the diagonal matrix elements are given by

$$U_i^{\text{diag}} = \langle e_i | \mathbf{U} | e_i \rangle \tag{4.2}$$

using the eigenvectors[1] of $\hat{U}$ in the long-wavelength limit $q \to 0$,

$$e_1 = \begin{pmatrix} 1/\sqrt{3} \\ 1/\sqrt{3} \\ 1/\sqrt{3} \end{pmatrix}, e_2 = \begin{pmatrix} \sqrt{2/3} \\ -1/\sqrt{6} \\ -1/\sqrt{6} \end{pmatrix}, e_3 = \begin{pmatrix} 0 \\ 1/\sqrt{2} \\ -1/\sqrt{2} \end{pmatrix}. \tag{4.3}$$

$U_1^{\text{diag}}(q)$ is the leading eigenvalue of the bare interaction. The other two eigenvalues only have a weak, anisotropic q-dependence and are, thus, assumed to be approximately constant; their values in our model are calculated by averaging the ab-initio values, see Fig. 4.3.

In most cases in this chapter and the next one, we look at the macroscopic values of the quantities of interest. This means that we use those values which are obtained by a transformation using the eigenvector e_1 of the bare interaction that corresponds to its leading eigenvalue. In this definition, the macroscopic value of some quantity A is given by

$$A_{\text{mac}} = \langle e_1 | A | e_1 \rangle. \tag{4.4}$$

For the leading eigenvalue of the interaction, we obtain a fit of the form

$$U_1^{\text{diag}}(q) = \frac{3e^2}{2\varepsilon_0 A} \frac{1}{q(1+\gamma q)} \tag{4.5}$$

with the area of the 2D hexagonal unit cell $A = \frac{\sqrt{3}}{2}a^2$ and the lattice constant a. The values for a can be found in Appx. A.1.2. The factor 3 is new in Eq. (4.5) compared to

[1] One might also try to fit the possible wave vector dependencies of these eigenvectors; the comparison of the ab-initio data for the eigenvectors to the analytic values given above in Eq. (4.3) is shown in Fig. C.1.

Eq. (2.47) and arises from the fact that we use three orbitals to describe the system and treat the Coulomb interaction in the eigenbasis of the bare interaction. γ describes how the effective height affects short wavelengths, which means that it is a structure factor and becomes important at large wave vectors close to $1\,\text{Å}^{-1}$ where q and q^2 are of the same order.

The screened matrix elements in the eigenbasis of the bare interaction are obtained for the undoped system via[2]

$$V_i^{\text{diag}}(q) = \left[\varepsilon_i^{\text{diag}}(q)\right]^{-1} U_i^{\text{diag}}(q) \tag{4.6}$$

where $\varepsilon_i^{\text{diag}}(q)$ accounts for the screening that results from the material specific interband polarizability and the polarizability of the substrate. In the philosophy of cRPA (see Sec. 2.3.2), this means that we do not involve intraband or metallic screening effects in the fitting procedure presented here and include them later on when we calculate the fully screened interaction W. The diagonal represantation of the interband and substrate screening is given by

$$\varepsilon^{\text{diag}}(q) = \begin{pmatrix} \varepsilon_1(q) & 0 & 0 \\ 0 & \varepsilon_2 & 0 \\ 0 & 0 & \varepsilon_3 \end{pmatrix} \tag{4.7}$$

where the constants ε_2 and ε_3 describe *microscopic* local screening effects which are similar to the bulk material and essentially unaffected by the dielectric environment of the monolayer. The *macroscopic* effects are described by the leading eigenvalue via

$$\varepsilon_1(q) = \varepsilon_\infty \frac{1 - \beta_1\beta_2 \mathrm{e}^{-2qd}}{1 + (\beta_1 + \beta_2)\mathrm{e}^{-qd} + \beta_1\beta_2\mathrm{e}^{-2qd}} \tag{4.8}$$

with factors

$$\beta_i = \frac{\varepsilon_\infty - \varepsilon_{\text{sub,i}}}{\varepsilon_\infty + \varepsilon_{\text{sub,i}}} \tag{4.9}$$

describing the influence of semi-infinite bulk materials on the screening inside of the monolayer. Eq. (4.8) was derived in Ref. [160] for a general case and applied to the situation described here in Ref. [81]. The involved parameters are an effective height d and the value of the screening at large wave vectors ε_∞. The values are derived from fits

[2]Please note that the calculation of the interband screened interaction V via Eq. 4.6 presents an approximation to the full ab-initio values of this interaction. It is not guaranteed that V is diagonal in the eigenbasis of the bare interaction U [see Eq. (4.3)] which can lead to additional errors beyond those of our fitting scheme for the bare interaction and the screening. The comparison of the ab-intio values to the fit values for the background screened interaction is done in Appx. C.

to the ab initio calculations for the freestanding layer. The surrounding substrates are approximated by dielectric constants $\varepsilon_{\text{sub},1}$ above and $\varepsilon_{\text{sub},2}$ below the monolayer which can be varied using Eq. (4.9). Note that we do not take into account possible frequency or wave vector dependencies of the substrate screening in our approach, which at the same time limits its accuracy but also gives us a model that is not restricted to a specific material and substrate, like MoS_2 on graphene [30].

In the case of vacuum surrounding the monolayer ($\varepsilon_{\text{sub},1} = \varepsilon_{\text{sub},2} = 1$), Eq. (4.8) simplifies to

$$\varepsilon_1(q) = \varepsilon_\infty \frac{\varepsilon_\infty + 1 - (\varepsilon_\infty - 1)\mathrm{e}^{-q\,d}}{\varepsilon_\infty + 1 + (\varepsilon_\infty - 1)\mathrm{e}^{-q\,d}}. \tag{4.10}$$

Once we have obtained the diagonal dielectric matrix $\varepsilon^{\text{diag}}(q)$, we can calculate the screened Coulomb interaction in the eigenbasis using Eq. (4.6) together with Eqs. (4.1) and (4.5) and the parameters in Tab. 4.1 (for $MoSe_2$; see Appx. B for values of the other TMDCs). Afterwards, we can transform to the orbital basis using the eigenvectors in Eq. (4.3). This analytic description allows to evaluate the bare and screened Coulomb matrix elements at arbitrary momenta q and for arbitrary dielectric environments.

Pseudo-Resta model

To be able to understand the limitations of our model description of the bare and interband screened Coulomb interaction, we turn to the Thomas-Fermi model for semiconductors by Resta, [161], and modify it to better describe the macroscopic part of the interband screening. First of all, we try to improve our fit of the largest eigenvalue of the bare interaction by introducing a cubic factor in Eq. (4.5), leading to

$$U^{\text{diag}}_{1,\text{Resta}}(q) = \frac{3e^2}{2\varepsilon_0 A} \frac{1}{q(1 + \gamma q + \delta q^2)} \tag{4.11}$$

with the new fit constant δ. This leads to the largest changes in $U_1^{\text{diag}}(q)$ when large values of q are considered. The description of the other two eigenvalues of the bare interaction is not changed.

Second of all, we employ a pseudo-Resta model for the macroscopic screening, which incorporates not two fitting parameters like the simple model in Eq. (4.8) but rather five fitting parameters a, b, c, d, e. We still rely on the fitting model for $\varepsilon_1(q)$, but make

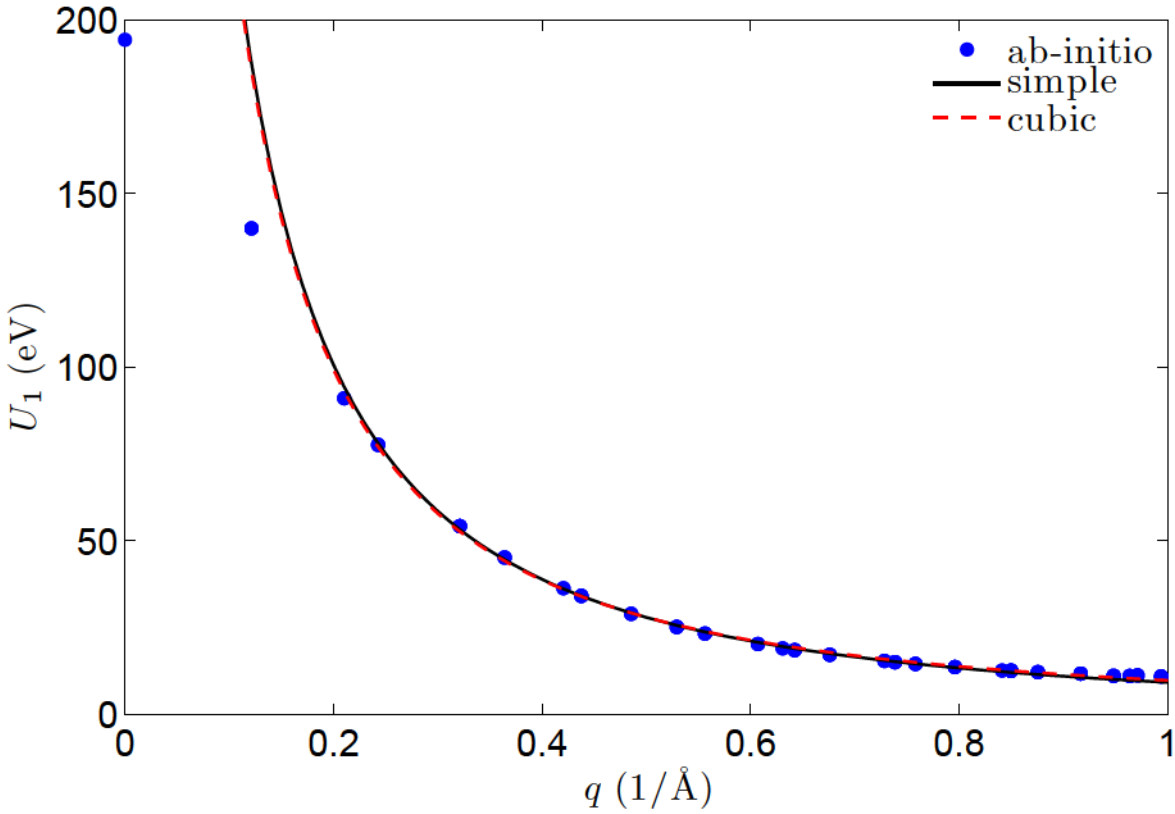

Figure 4.2.: Fit of the leading, macroscopic eigenvalue U_1 of the bare interaction U in $MoSe_2$. Circles show the ab-initio data, the black line shows the quadratic fit and the red dashed line the cubic pseudo-Resta fit.

the former constant ε_∞ wave vector dependent

$$\varepsilon_\infty^{\text{Resta}}(q) = \frac{a + q^2}{\frac{a}{b}\frac{\sin(qc)}{qc} + q^2} + e. \tag{4.12}$$

The results of this model are shown and compared to the simple model in Figs. 4.2, 4.4, 4.13, and 5.8.

4.2.2. Discussion of results

Now that we have discussed our approach to obtain a model for the Coulomb interaction of the relevant bands in 2D TMDCs, we present the results of the fits. The focus here lies on one example, $MoSe_2$, but most of the results are very similar for the other members of this material class. The specific fit parameters for all TMDCs can be found in Appx. B.

Table 4.1.: Parameters of Coulomb interaction in $MoSe_2$.

bare U	
leading EV, quadratic	
γ (Å)	2.061
leading EV, cubic	
γ (Å)	2.232
δ (Å^2)	-0.356
microscopic EV	
U_2 (eV)	0.837
U_3 (eV)	0.376

dielectric ε	
leading EV, simple	
ε_∞	10.238
d (Å)	9.615
leading EV, pseudo-Resta	
a (1/Å^2)	1.605
b	13.181
c (Å)	5.772
d (Å)	3.499
e	7.508
microscopic EV	
ε_2	3.148
ε_3	2.510

As described above, our first step is to fit Eqs. (4.5) and (4.11) to the ab-initio results for the largest, macroscopic eigenvalue of the bare interaction which we obtain from calculations with FLEUR and Spex [62, 83] using the RPA or the cRPA approach, see Secs. 2.3.1 and 2.3.2. The results are shown in Fig. 4.2 and Tab. 4.1. For wave vectors $q > 0.2\,\text{Å}^{-1}$, both fit models describe the ab-initio data very well[3]. At this point, the difference between the two fit models is almost negligible; the cubic fit has slightly more accurate results only for large q close to $1\,\text{Å}^{-1}$ since it can describe the flattening of the ab-initio values by a negative prefactor for the q^3-term (see δ in Tab. 4.1). Both models are not able to describe the trend of the ab-initio values of U_1 for $q \to 0$, but this is no problem because these values result partly from a finite vacuum height of all supercells involved in the calculations. Furthermore, finite values of the Coulomb interaction for $q = 0$ are not physical in non-metallic systems, which means that the results of the calculations cannot be trusted for $q \approx 0$; this sets a natural limit for the lower end of our fit range which excluded the point at $q = 0$ in all cases.

For the full description of the bare interaction, we also need the eigenvectors according to Eq. (4.3) and the two microscopic eigenvalues of U, which are shown in Fig. 4.3. We observe that that the average values of the two eigenvalues are $U_2 \sim 0.8\,\text{eV}$ and $U_3 \lesssim 0.4\,\text{eV}$ (see Tab. 4.1), which is a general feature for all the TMDCs considered here (see the corresponding tables in Appx. B). To use the average as a model description

[3]Since in the end we are interested mainly in the orbital Coulomb interaction that already involves screening by interband transitions, we will discuss deviations of our fit model from ab-initio results primarily later on in this section and in Appx. C.

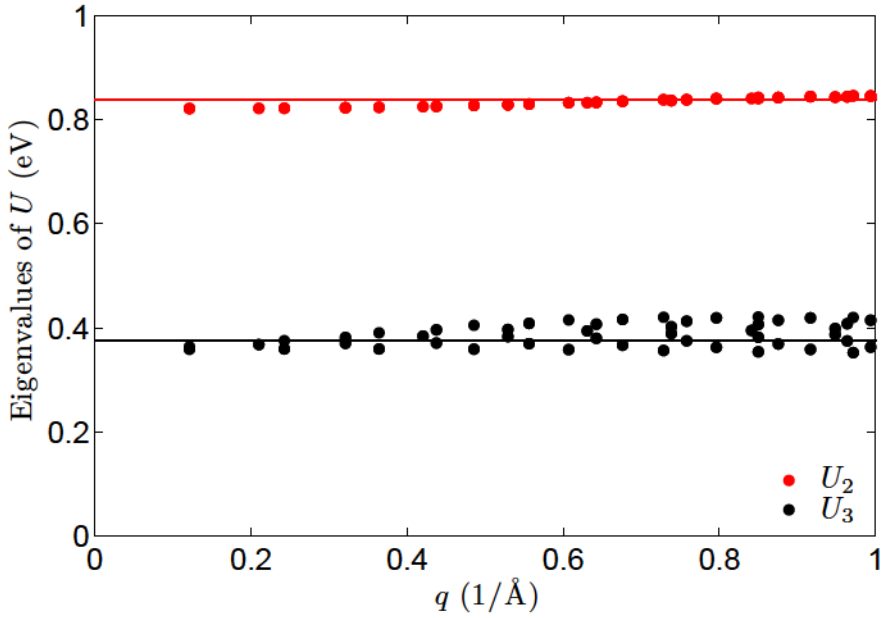

Figure 4.3.: The two microscopic eigenvalues of the bare interaction U in $MoSe_2$. Circles show the ab-initio data, while the lines show the average values that we use in our model.

of the microscopic eigenvalues seems justified because the deviations of the ab-initio data are less than 10 %. Besides that, the anisotropy present in the values of the third eigenvalue renders any kind of scalar fit rather difficult.

Having obtained model parameters for the bare Coulomb interaction, we now discuss the screening. Here, we only give our results for the interband screening; other screening effects are discussed in Sec. 4.3. The ab-initio data and fit results for the interband screening ε_1 of the leading eigenvalue of U without substrates are presented in Fig. 4.4. Starting from $\varepsilon_1 = 1$ at $q = 0$, the screening rises to values $\varepsilon_1 \gtrsim 10$ up to $q \sim 0.5\,\text{Å}^{-1}$ and lowers again for larger q, which looks somewhat similar to a damped sine function. For $q \gtrsim 0.6\,\text{Å}^{-1}$, some anisotropy in the data is visible. With our simple fit model, we can correctly describe the ab-initio values for $q = 0$ and $q > 0.2\,\text{Å}^{-1}$ within a range of 10 %, but the shape of the screening is only reproduced approximately. The somewhat sinoidal behavior, i.e. the rise and decrease of the ab-initio values, cannot be found in this model since its values approach the constant ε_∞ for $q \sim 0.4\,\text{Å}^{-1}$. The pseudo-Resta model on the other hand yields a much better fit of the screening and reproduces both the shape and the values of the ab-initio data. One important disadvantage is though that we lose the simple interpretation of the parameters ε_∞ and d that we have in the simple model, where ε_∞ is a short-wavelength dielectric constant, similar to the bulk

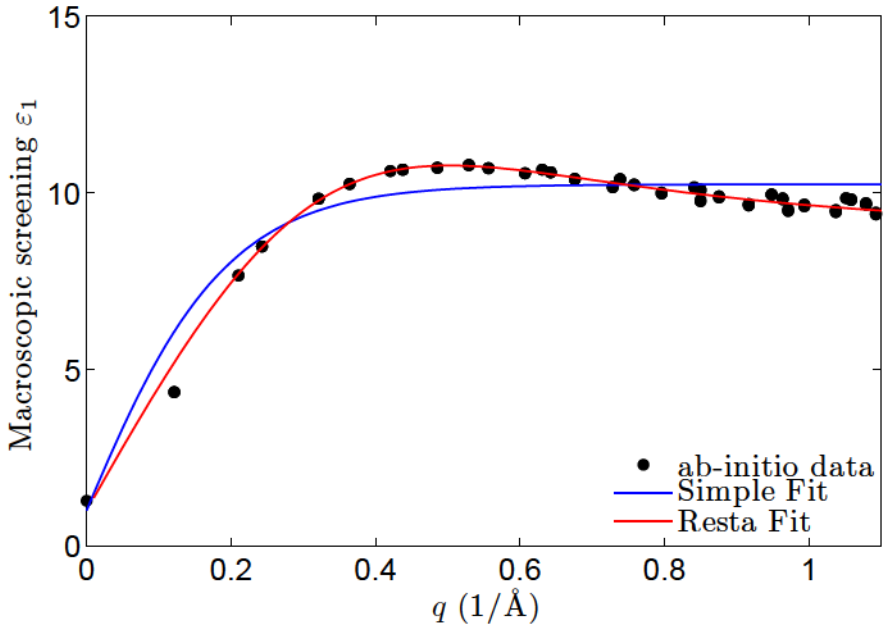

Figure 4.4.: Fits of the macroscopic part $\varepsilon_1(q)$ of the interband screening in $MoSe_2$.

material, and d can be viewed as an effective height of the monolayer.

Alongside with the fit of ε_1, we further need the averages of the two values of the screening ε_2 and ε_3 that belong to the microscopic eigenvalues of U and describe microscopic screening effects occurring locally inside of the monolayer. The corresponding data is shown in Fig. 4.5. The situation here is similar to the microscopic eigenvalues U_2 and U_3; the deviation of the ab-initio data from the average values is 10 % or less and is in large parts due to the anisotropy in the ab-initio values. This is also the reason why a scalar fit would not lead to improved results compared to the simple average. As a last point, we note that the values of $\varepsilon_2 \sim 3$ and $\varepsilon_3 \sim 2.5$ (see Tab. 4.1) are similar for all TMDCs, see the corresponding tables in Appx. B.

Limitations of fit models

While our two fit models are in general a simple, yet accurate way to describe the Coulomb interaction in 2D TMDCs, they have some obvious shortcomings (see also Appx. C). First of all, the exclusion of the half-filled band in the cRPA calculations on metallic TMDCs as well as the exclusion of doping in the RPA ab-initio calculations on semiconducting TMDCs limits the applicability of our models (see Sec. 2.3.2). Since no transitions between the other electronic bands and the three bands of our Wannier model

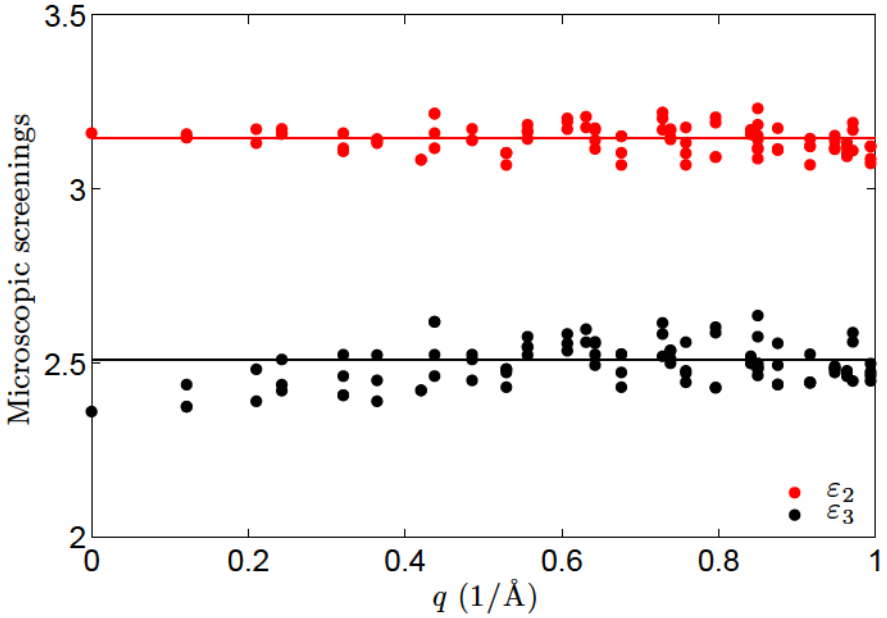

Figure 4.5.: Microscopic parts $\varepsilon_2(q)$ and $\varepsilon_3(q)$ of the interband screening in $MoSe_2$. Ab-initio data is depicted as dots, while the averages for the fit model are shown as lines.

are included in the three-band description, it is only reasonable to apply our model in a certain energy range of less than $\sim 1\,\mathrm{eV}$. Second of all, the use of the eigenvectors of $U(q \to 0)$ over the whole range of wave vectors, cf. Eq. (4.3), may be questioned. Although the variation of the ab-initio values compared to the analytic ones is 10 % or less, see Fig. C.1, a fit of the eigenvectors could improve the Coulomb interaction model.

For the calculations following in Sec. 4.4 and chapter 5, we of course do not use the Coulomb interaction in the eigenbasis, but rather the interband screened interaction in the orbital basis $V_{\alpha\beta}$. Thus, we look at the differences between the results of our models and the ab-initio values in this basis, see Fig. C.2. For the diagonal matrix elements, both fit models describe the ab-initio values quite well with deviations of less than $\pm 20\,\%$ for $q < 0.6\,\text{Å}^{-1}$, while the errors of the simple fit are slighty smaller than for the pseudo-Resta fit. Concerning the off-diagonal matrix elements, the deviations are larger with less than $\pm 25\,\%$ for $q < 0.6\,\text{Å}^{-1}$ and the pseudo-Resta fit works a little better than the simple one. At large q, especially these off-diagonal values of $V_{\alpha\beta}$ become more anisotropic and the errors of our fits get larger, except for the $d_{xy} - d_{x^2-y^2}$ matrix element. This shows that one has to be careful when using the fit models far away from the Brillouin zone center.

In the end, the main issue that one has to deal with when choosing which model to employ is a competion between simplicity and accuracy. Since we cannot guarantee that the results of our ab-initio calculations are perfectly accurate to begin with, we have chosen to stay with the simple fit model for most results presented in this thesis and have for example not fitted the eigenvectors of the bare interaction. The results of the pseudo-Resta model will be shown whenever a comparison between the two models is deemed useful.

4.3. Screening in semiconducting and metallic systems

When we talk about the screening of the Coulomb interaction in this thesis, we distinguish three different screening mechanisms:

- Interband screening that is due to the microscopic polarizability given by transitions between different electronic bands already in the isolated semiconducting and undoped layer. See Eqs. (4.7) and (4.10).
- Substrate screening due to the dielectric environment; this can be metallic. See Eq. (4.9).
- Metallic screening inside the monolayer due to a partially filled conduction band. See Eq. (2.50).

Only the influence of the interband screening was discussed in the previous section. Here, we describe the other two screening channels.

In Fig. 4.6, we show the full background screening, i.e., the combination of the interband screening and the substrate screening according to Eq. (4.8), for dielectric constants $\varepsilon_{\text{sub}} = 1, 5, 10, 50, \infty$ of the encapsulating environment as sketched in the right part of the figure. One can see that the influence of the environment is most important for small wave vectors. At $q < 0.2\,\text{Å}^{-1}$ the background screening $\varepsilon_1(q)$ is largely determined by the dielectric environment; for very large wave lengths $q \to 0$, it is solely determined by the substrates, i.e., $\varepsilon_1(q \to 0) = \varepsilon_{\text{sub}}$. One important point here is that the screening inside the layer can be metallic, $\varepsilon_1(q \to 0) \to \infty$, solely due to a metallic environment and without the monolayer itself being metallic. With increasing q, the background screening in our model approaches the material specific constant ε_∞. At $q > 0.6\,\text{Å}^{-1}$, the substrates have nearly no influence, $\varepsilon_1 = \varepsilon_\infty$. This behavior of the screening for

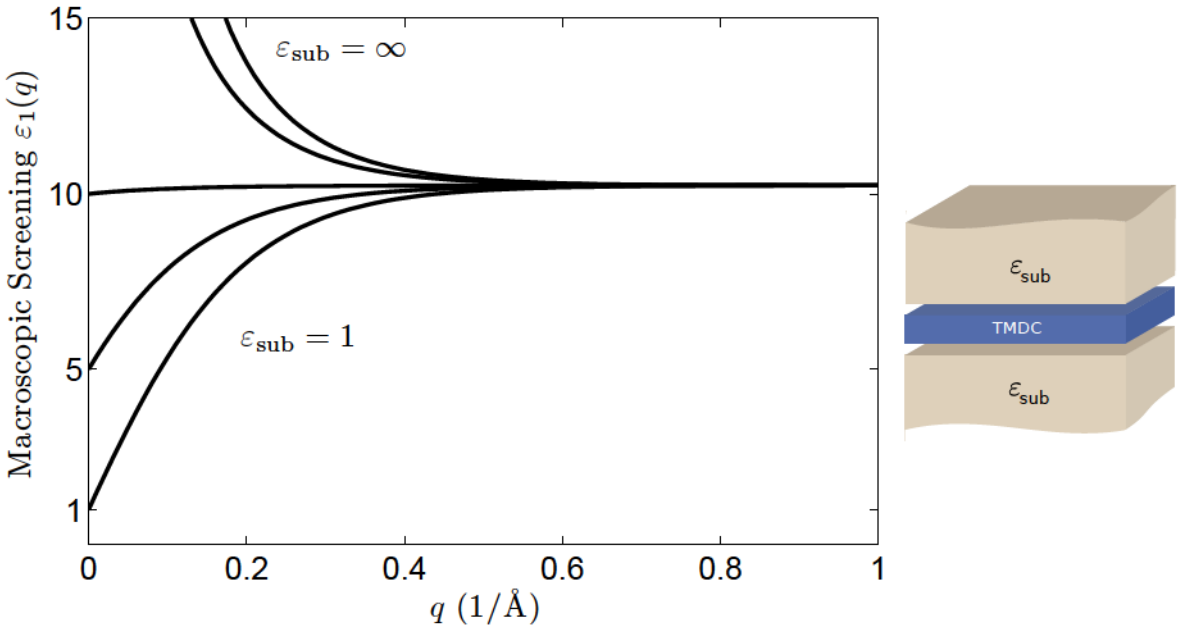

Figure 4.6.: (Left) Macroscopic screening for different dielectric environments of $MoSe_2$. (Right) Sketch of the model situation for our calculations.

small and large wave vectors can be intuitively understood if one considers the fact that for small wave vectors, i.e., large distances, most of the electric field lines pass through the surrounding and, thus, the screening is determined by the dielectric environment of the monolayer, cf. Fig. 4.1; for large wave vectors, the charges are close together and the material itself determines the screening.

If we further take into account the screening by conduction electrons inside the material, we find that the screening diverges at small wave vectors q in all metallic cases, see Fig. 4.7. In the case of high electron doping concentrations the screening is strongly enhanced compared to the other cases. It approaches a constant level that is higher than ε_∞ for wave vectors $q > 0.5\,\text{Å}^{-1}$, while it diverges for smaller q. For low electron doping concentrations, we can identify three different ranges. At $q \gtrsim 0.4\,\text{Å}^{-1}$, the screening is close to ε_∞ and basically not influenced by the conduction electrons. For smaller wave vectors $0.2 \lesssim q \lesssim 0.4\,\text{Å}^{-1}$, the additional screening by the conduction electrons is stronger than ε_∞ but weaker than the screening by a fully metallic environment. Below $q \sim 0.2\,\text{Å}^{-1}$, the screening by the additional conduction electrons becomes effective and is stronger than the metallic substrate screening.

Finally, we show the orbital dependent onsite values in real space of the bare and screened Coulomb interaction in $MoSe_2$ in Tab. 4.2 (see Appx. B for the values of other TMDCs).

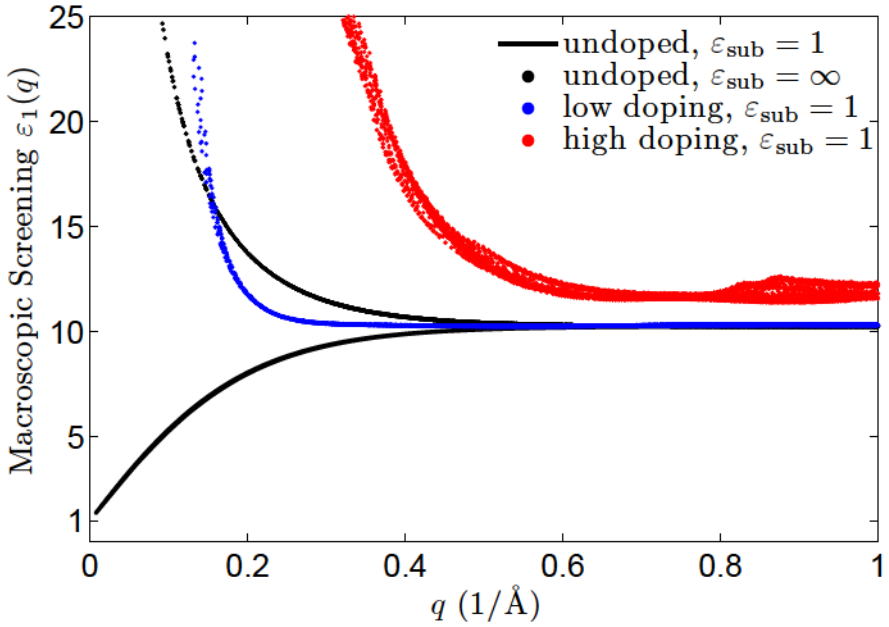

Figure 4.7.: Macroscopic screening in $MoSe_2$ with vacuum and metallic surrounding as well as low ($x \approx 0.02$) and high ($x \approx 0.17$) electron doping with vacuum surrounding.

The values are calculated using a Fourier transformation[4] of the orbital values in k-space which are obtained in the way described in Sec. 4.2.1 with the addition of Eq. (2.51) for the doped metallic case. One can clearly see that the inclusion of interband transitions, i.e., of the screening in the semiconducting layer reduces the bare interaction by a factor of 6 to 7. The corresponding matrix elements V are in general larger for the sulfur compounds than for the selenium compounds, see Appx. B, while no obvious dependence on the transition metal is observable. If we go to the metallic case and include screening by the additional conduction electrons, the onsite interaction is further reduced by a factor of 2 to 3. As a side remark, we mention that the local exchange interaction is $\sim 0.25\,\text{eV}$ between d_{z^2} and one of the other orbitals and $0.15\,\text{eV}$ between d_{xy} and $d_{x^2-y^2}$ for all TMDCs considered in this thesis (see Tab. B.11), i.e., it is insensitive to both material characteristics and screening.

Lastly, we compare the onsite interaction in the TMDCs to the onsite interaction in graphene. Similar calculations to those described here led to values of $17\,\text{eV}$ for the bare interaction in graphene and $9.3\,\text{eV}$ for the interaction that includes screening by all bands but the π-bands [34]. The band width of the π-bands in graphene is on the order of $3t = 8.1\,\text{eV}$ with the hopping $t = 2.7\,\text{eV}$ [9]. Considering the band width of about

[4]Since we discuss only onsite values, which means that the corresponding real space vector is $R = 0$, the Fourier transform simplifies to an average of all reciprocal space values.

Table 4.2.: Bare onsite U as well as background screened onsite V and fully screened onsite Coulomb matrix elements W for the three important orbitals of $MoSe_2$. Values for W are in the range of low electron doping $x \approx 0.03$ in the fifth (W_{low}, K is occupied) and for high electron doping $x \approx 0.17$ in the last column (W_{high}, K and Σ are occupied).

orbitals		bare	undoped	doped	
		U (eV)	V (eV)	W_{low} (eV)	W_{high} (eV)
d_{z^2}	d_{z^2}	8.95	1.41	0.77	0.56
d_{z^2}	d_{xy}	8.11	1.14	0.52	0.33
d_{z^2}	$d_{x^2-y^2}$	8.11	1.14	0.52	0.33
d_{xy}	d_{xy}	8.72	1.35	0.75	0.55
d_{xy}	$d_{x^2-y^2}$	8.34	1.20	0.60	0.40
$d_{x^2-y^2}$	$d_{x^2-y^2}$	8.72	1.35	0.75	0.55

1.6 eV for the lowest conduction band of $MoSe_2$, see Fig. 3.4, we can conclude that the relation between the (partially) screened Coulomb interaction and the band width is on the order of 1 in both the TMDCs and graphene.

4.4. Plasmons and EELS

Plasmons are quasiparticles describing collective excitations of the electrons in a material; they may be thought of as oscillations of the charge density. They are given by the roots of the dielectric function $\varepsilon(\boldsymbol{q}, \omega)$, see Eq. (2.50). While the plasmon dispersion is determined by

$$\operatorname{Re}\left[\varepsilon(\boldsymbol{q}, \omega)\right] = 0 \tag{4.13}$$

for damping rates that are much smaller than the plasmonic frequency ω_{p}, we also need the imaginary part to be zero to have a long-lived plasmonic mode; otherwise, the imaginary part determines the lifetime of the plasmon. In the following, we plot the Electron Energy Loss Spectrum (EELS) to show the plasmon dispersions,

$$EELS(\boldsymbol{q}, \omega) = -\operatorname{Im}\left[\frac{1}{\varepsilon(\boldsymbol{q}, \omega)}\right], \tag{4.14}$$

since it can be measured directly in experiments [162] and shows plasmonic, but also single-particle resonances such as electron-hole excitations. We use the macroscopic value of the dielectric function ε, i.e., the largest eigenvalue with respect to the bare Coulomb interaction, see Eq. (4.4).

Depending on the dimensionality of the system - and, thus, the q-dependence of the Coulomb interaction, cf. Sec. 4.1 and Eq. (2.47) therein - the plasmon dispersion behaves differently already on the general level of non material-specific, bare interaction. In the long-wavelength limit $q \to 0$, the plasmons have no dispersion and a finite frequency ω_p in 3D, while they follow a square root dispersion in 2D and a linear dispersion in 1D; see for example [163]. For a 2D electron gas in this limit, the dispersion is

$$\omega_\mathrm{p}(q) = \sqrt{\frac{2\pi e^2}{m} q} \tag{4.15}$$

which we will find as a limit in the numerical results presented later on in this section. It has, for example, also been found in theoretical investigations of doped graphene [164]. As a sidenote, we remark that there can be multiple plasmon modes in the electron gas of layered materials; depending on the out-of-plane wave vector q_z, they follow dispersions that lie between the square root dispersion and a constant frequency [165, 166].

Plasmonic resonances can be utilized in different ways, and surface plasmons of bulk materials have an especially high and long discussed potential for optical sensing and the characterization of thin films and interfaces [167]. Lately, the application of plasmons in the context of information technology and electronics, called plasmonics, has been a major point of research [168]. Plasmonics in graphene have attracted a lot of attention since the plasmon dispersion in this material can be tuned via doping and electric field gating [169–171]. Another interesting topic is that, because of their low energies in 2D, plasmon modes might be benefitial for plasmon-mediated or plasmon-assisted superconductivity, see for example [166, 172–174].

Various ways are possible to calculate the plasmon dispersion; here, we use RPA to obtain the dielectric function from our three-orbital models for the Coulomb interaction and the electronic properties of the the TMDCs. This means that we include only Landau damping which occurs due to the excitation of single particle-hole pairs; other damping effects like electron-phonon or electron-electron scattering, [175, 176], are not explicitly included. However, the finite broadening η in the equation for the RPA/Lindhard polarization, Eq. (2.53), amounts to a phenomenological description of these processes.[5]

In the following, we present the results for the EELS of doped semiconducting and metallic TMDCs, with a focus on $MoSe_2$ and NbS_2, respectively. We show how the

[5] We use a value of $\eta = 1\,\mathrm{meV}$.

plasmon dispersions depend on both electron doping and the dielectric environment. Note that we did not include spin-orbit coupling in our calculations, which can be a severe limitation depending on the effect one wants to discuss [71].

4.4.1. Doped semiconductors

The plasmonic dispersions of semiconducting TMDCs have been investigated before [71, 177, 178], but sofar other materials than MoS_2 have received little attention and the influences of substrates have not been investigated. Here, we improve on this by explicitly discussing the effects of substrates and by calculating the EELS of all four semiconducting TMDCs discussed in this thesis. First, we look at the EELS for doped $MoSe_2$ along the high symmetry path through the Brillouin zone (see Fig. 3.3). In Fig. 4.8, we consider low and high doping concentrations and no substrates, similar to Fig. 4.7. For low doping concentration, where only the K-valley in the electronic band structure is occupied, one can identify a variety of features in the energy range below 0.5 eV. The continuum of electron-hole excitations has minimal positions with $\omega = 0$ at $q = \Gamma$ and $q = \mathrm{K}$, while it reaches its maximum between Γ and M and has two seperate branches at Σ. A plasmon dispersion is visible for very small wave vectors around Γ with energies below 0.2 eV. It approaches the continuum rather rapidly with increasing q. At high doping concentration, where the K- and the Σ-valley in the band structure are both occupied by electrons, a lot of the other features of the EELS get blurred while the plasmon dispersion becomes more pronounced. Following the initial square root rise at very small q, it has a flat shape with $\omega \lesssim 0.5\,\mathrm{eV}$ and enters the continuum at $q \lesssim 0.3\,\mathrm{M}$ and $q \lesssim 0.5\,\Sigma$. In addition to the blurring, some new features also appear in the EELS. The electron-hole continuum has one branch with very large energy around Σ and one with a constant energy $\omega \lesssim 0.3\,\mathrm{eV}$ around K.

Next, we present the dependence of the plasmonic dispersion on doping as well as substrate screening for the path $\Gamma \to \Sigma$, see Fig. 4.9. We observe that the plasmon dispersion is strongly tuneable by doping and the dielectric environment. Both the shape and the energy can be varied. In general, one can see that an increasing dielectric constant *pushes* the dispersion into the continuum, i.e., the initial rise for small q is less steep and the overall shape is less different from a linear function. On the other hand, increased electron doping also changes the shape of the dispersion and leads to a raise of the maximum plasma frequency from between 0.1 and 0.2 eV at $x = 0.02$ to approximately 0.5 eV at $x = 0.17$. In all cases, no clear plasmon dispersion can be identified for $q > 0.5\,\Sigma$.

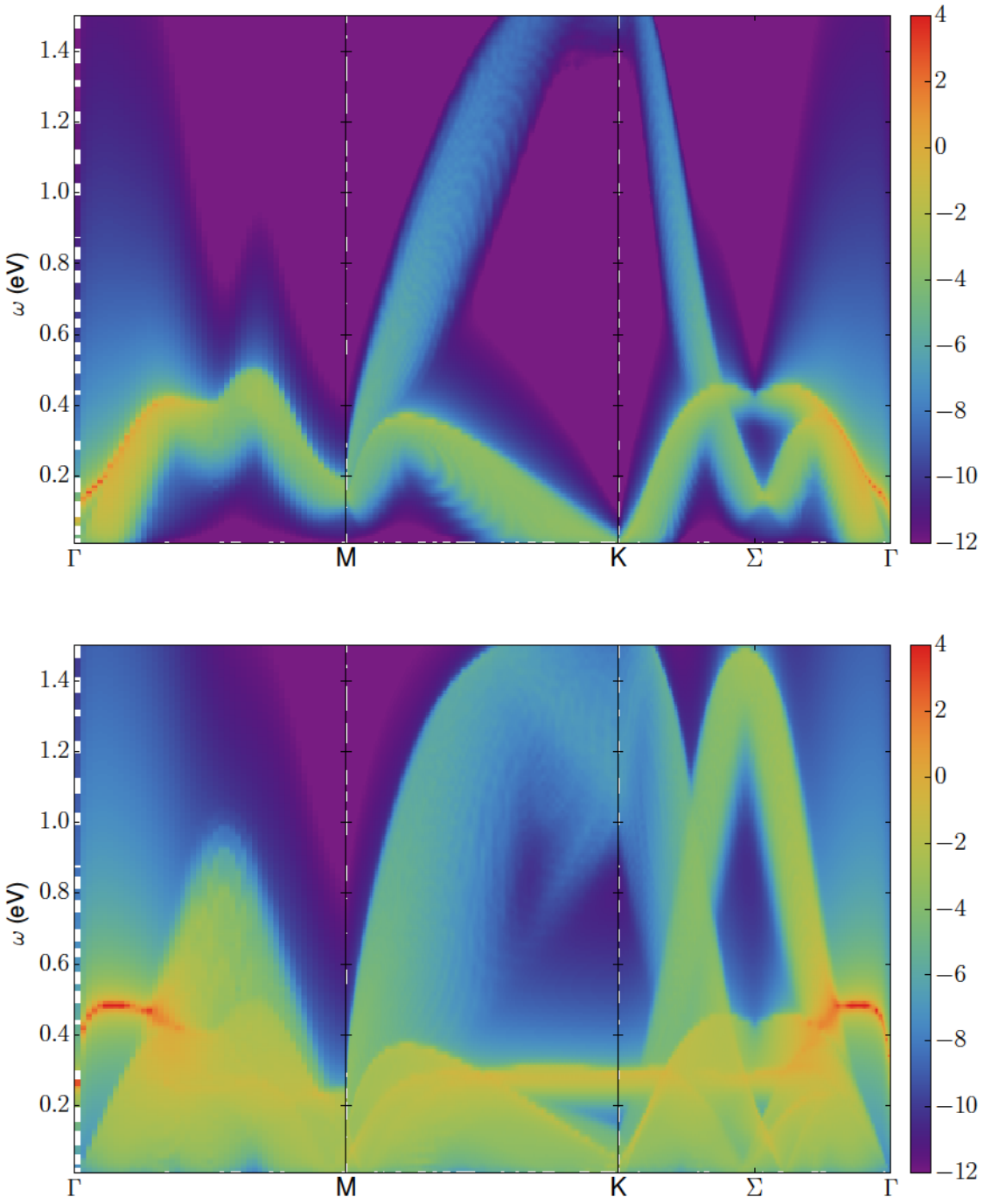

Figure 4.8.: EELS for $MoSe_2$ without substrate for doping concentrations $x = 0.02$ (Top) and $x = 0.17$ (Bottom). The color scale is logarithmic.

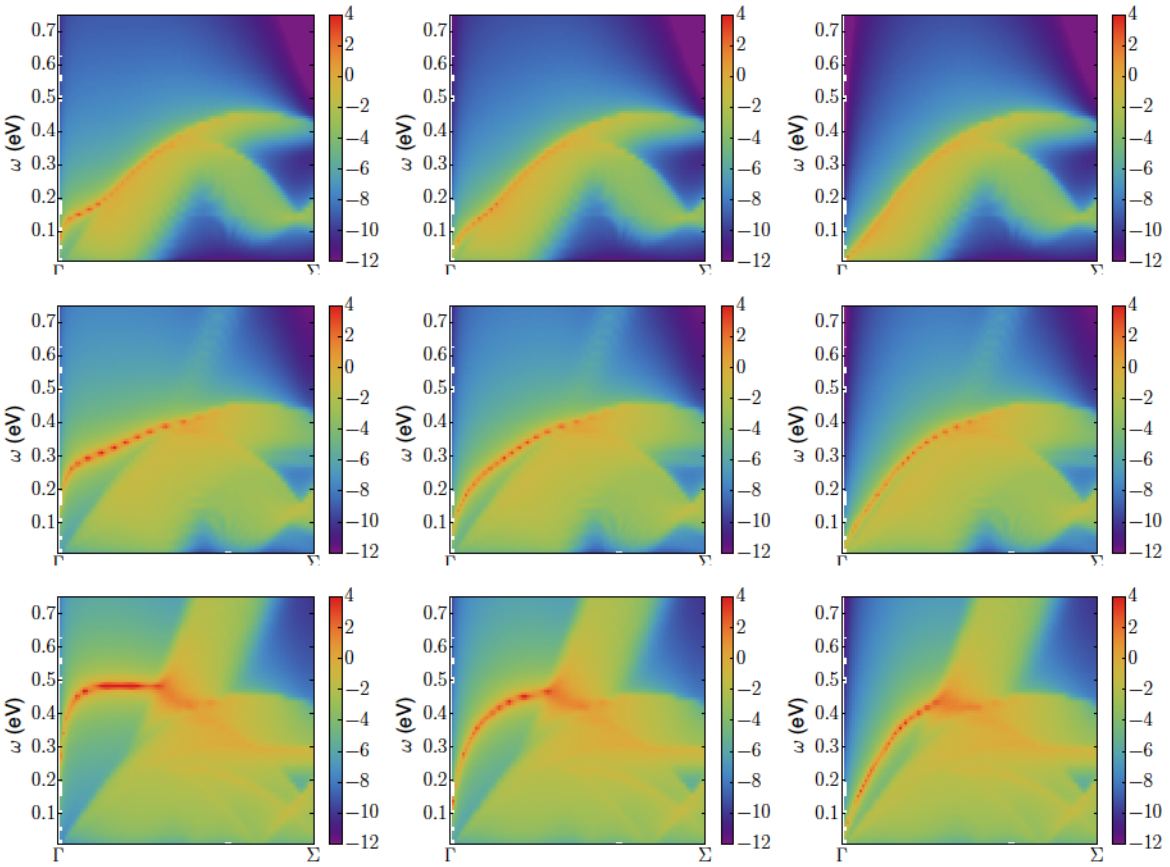

Figure 4.9.: EELS for $MoSe_2$ with doping concentrations $x = 0.02$ (Top), $x = 0.05$ (Middle) and $x = 0.17$ (Bottom) and substrate dielectric constants $\varepsilon = 1$ (Left), $\varepsilon = 5$ (Middle) and $\varepsilon = 50$ (Right). The color scale is logarithmic.

As a last step, we compare the EELS for $MoSe_2$, MoS_2, WSe_2 and WS_2, see Fig. 4.10. We use the path $\Gamma \to K$ and consider the case of electron doping $x \gtrsim 0.09$, where both valleys are occupied, and vacuum surrounding. The four materials all have similar features, such as a plasmon frequency at $\omega \gtrsim 0.4\,\mathrm{eV}$, but the specific shape of the plasmon dispersion and the electron-hole continuum are subject to changes. One can see that the dispersions are similar to the bare 2D square root dispersion in all cases, see Eq. (4.15). For $MoSe_2$, its frequency stays around $0.4\,\mathrm{eV}$, while it undergoes a rise to nearly $0.6\,\mathrm{eV}$ for the other three materials. The EELS also have some structure beyond the plasmon dispersions. Around the Σ point, the electron-hole continuum is split up into three (two for WS_2) regimes with larger intensities, shown by the green color in the logarithmic color scale, and two (one) intermediate frequency regimes with lower intensities. The splitting of the two lower regimes with larger intensity is not clearly visible for $MoSe_2$, while it is similar for MoS_2 and WSe_2 and most pronounced for WS_2.

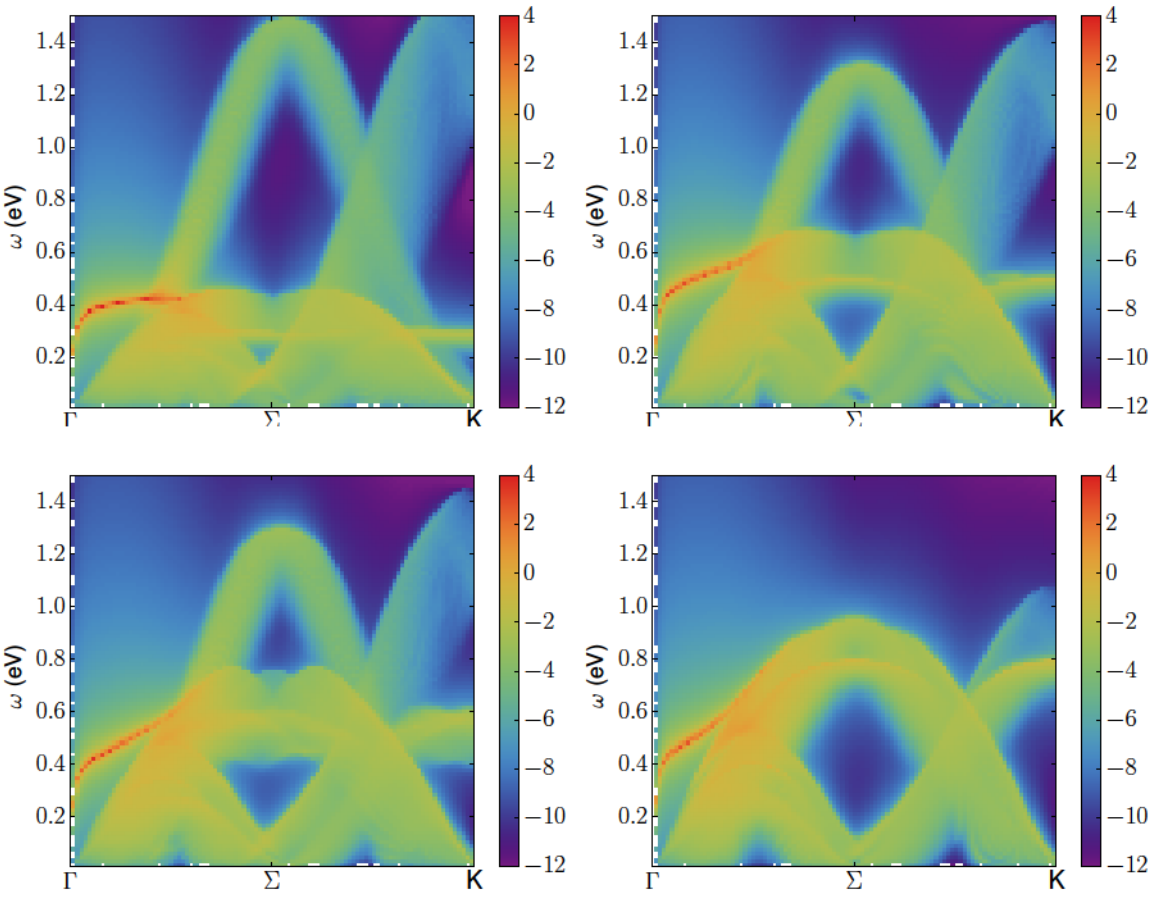

Figure 4.10.: EELS for TMDCs $MoSe_2$ (Top left), MoS_2 (Top right), WSe_2 (Bottom left) and WS_2 (Bottom right) for electron doping $x \gtrsim 0.09$ without substrate. The color scale is logarithmic.

4.4.2. Metals

The plasmonic spectra of several metallic TMDCs have been investigated before in Ref. [179]. Furthermore, a possible influence of charge order on the plasmon dispersion has been studied concerning $NbSe_2$ [180], NbS_2 [181] and other metallic TMDCs such as TaS_2 [182]. Here, we do not include charge order (see Sec. 5.4) and its effects, and we also omit the effects of doping that we looked at in the previous section, although they can be important in metallic TMDCs [183]. However, we include the effects of dielectric substrates, which have not yet been investigated for metallic TMDCs.

First, we show the EELS along the full high symmetry path for undoped, half-filled NbS_2 and $NbSe_2$ with vacuum surrounding in Fig. 4.11. Distinct square root shaped plasmon dispersions can be observed in both cases. NbS_2 has a larger plasmon frequency

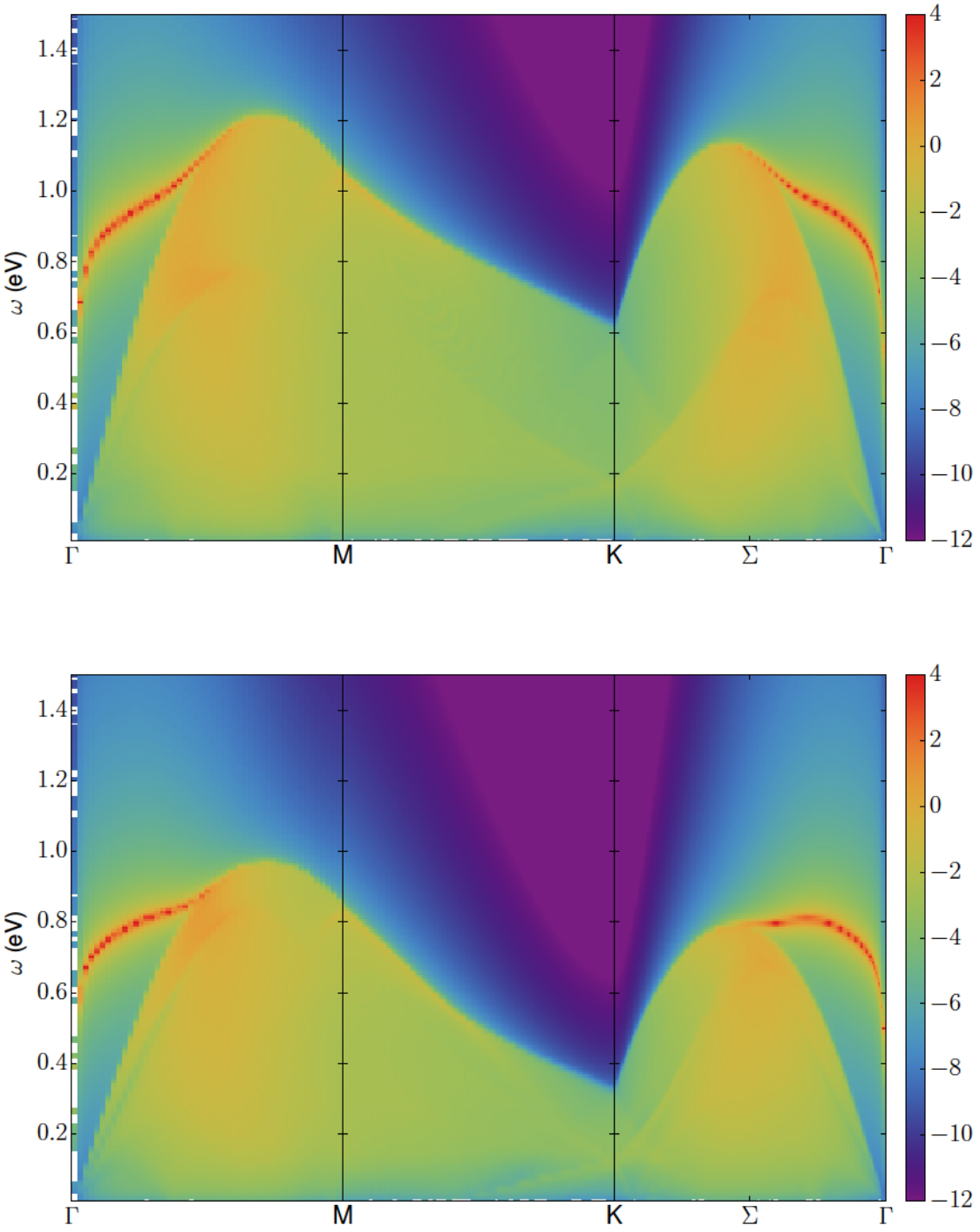

Figure 4.11.: EELS for NbS_2 (Top) and $NbSe_2$ (Bottom) without substrate. The color scale is logarithmic.

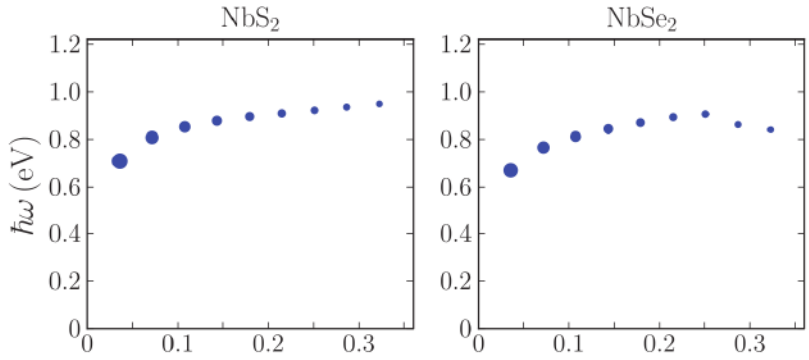

Figure 4.12.: Plasmon dispersions for NbS_2 and $NbSe_2$ as obtained by Andersen et al. in Ref. [179]. The scale of the x-axis is $q(\text{Å}^{-1})$.

$\omega \gtrsim 0.8\,\text{eV}$ and larger slope of the dispersion. In $NbSe_2$, the dispersion has a more constant shape with $\omega \lesssim 0.8\,\text{eV}$. Due to the Fermi surfaces and half filling, the electron-hole continuum has no distinct branches as in the case of the doped semiconductors, and its shape basically follows the band structure of the half-filled band[6], cf. Figs. 3.9 and 3.10.

To verify our method, we compare the EELS for NbS_2 and $NbSe_2$ as obtained from our RPA calculations, see Fig. 4.11, to the plasmon spectra obtained by Andersen et al., see Fig. 4.12. One can see that the initial steep rise of the plasmon dispersion as well as the general shape are similar. Furthermore, both calculations find a large wave-vector range with an only slightly dispersing plasmon frequency which lies above 0.8 eV (NbS_2) and around 0.8 eV ($NbSe_2$). The difference between the two materials is more pronounced in our results than in the ones by Andersen et al. They claim that the dispersions from Γ to M and from Γ to K are very similar, which we do not see in the case of $NbSe_2$. The constant or even negative dispersion that they find for this material is only obtained in the direction from Γ to K in our results.

As a last step, we look at the change of the plasmon dispersion along $\Gamma \to \text{K}$ in NbS_2 with different substrate dielectric constants and compare to the results for the pseudo-Resta model of Eqs. (4.11) and (4.12). From Fig. 4.13, one can see that the shapes of both fit models are different in a small range if no substrate is included, but that their frequencies are very similar. The pseudo-Resta model yields a rather dispersionless mode, while the simple model has a non-vanishing slope. Furthermore, the previously discussed fact that the dielectric environment *pushes* the dispersion into the continuum

[6]The band width is approximately 1.2 eV in NbS_2, while it is less than 1 eV in $NbSe_2$.

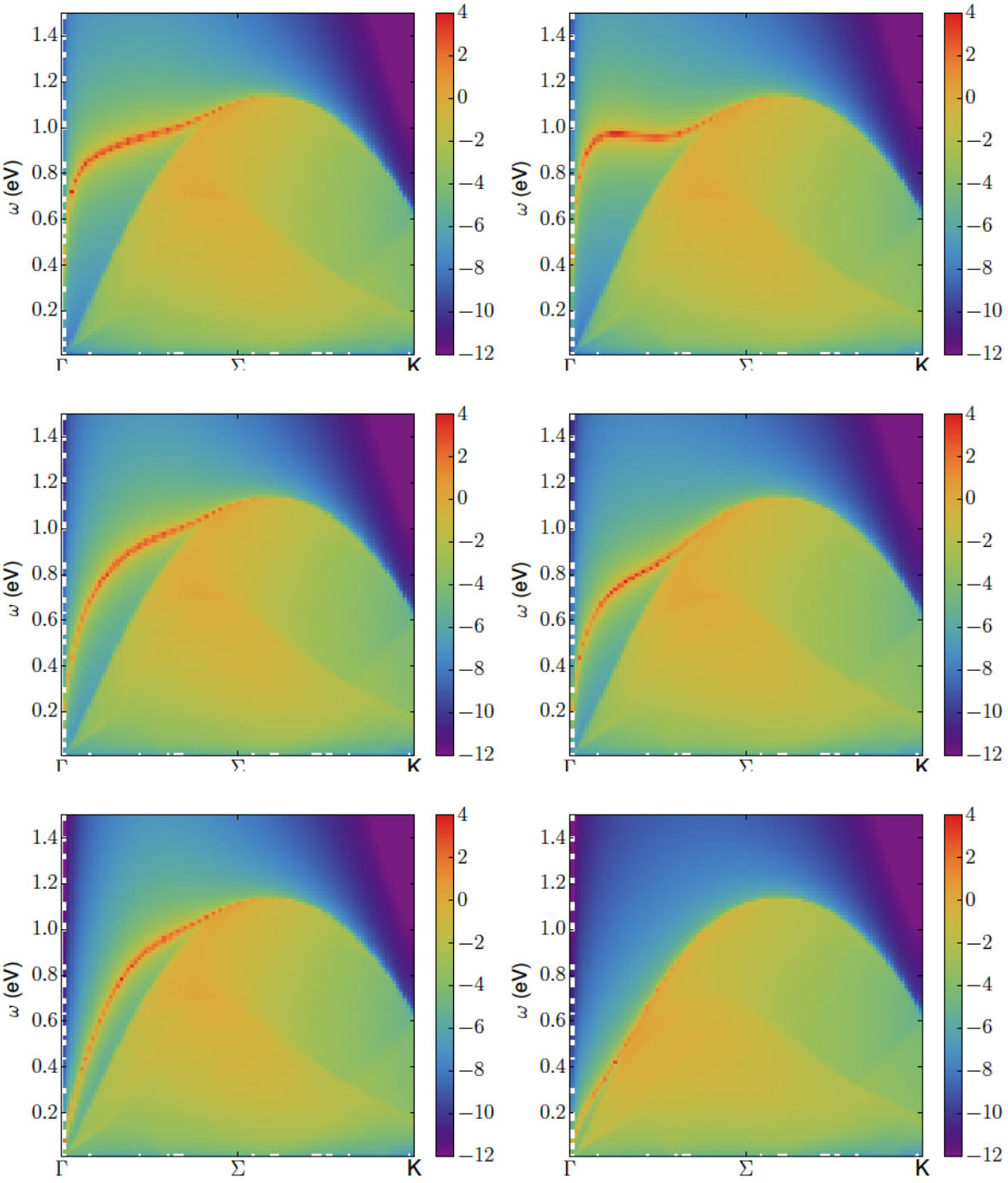

Figure 4.13.: EELS for NbS_2 with substrate dielectric constants $\varepsilon = 1$ (top), $\varepsilon = 5$ (middle) and $\varepsilon = 50$ (bottom). On the left side, we show the results for the simple fit to the Coulomb interaction, while on the right the results for the Pseudo-Resta fit are plotted. The color scale is logarithmic.

can be observed here, too. For the pseudo-Resta model, this happens faster with the dispersion not being distinguishable from the continuum for a large dielectric constant $\varepsilon = 50$.

5. Electronic instabilities in two-dimensional materials

When we talk about instabilities in this thesis, we always discuss the instability of the conduction electrons towards the formation of a long-range ordered phase. In the field of 2D materials and especially TMDCs, several examples such as superconductivity [22, 28], Charge Density Wave (CDW) phases [16, 23] and Spin Density Wave (SDW) phases [184] have been ivestigated so far. Other examples in layered materials include the high-temperature superconductivity and the Mott transition from metal to insulator in the cuprates [97]. The Mott transition was also experimentally observed for 1T-TaS_2 [19] and claimed to occur in monolayer 1T-$NbSe_2$ [185]. Here, we look at conventional superconductivity in the TMDCs (Sec. 5.1) and functionalized graphene (Sec. 5.2), as well as possible unconventional superconductivity in MoS_2 (Sec. 5.3) and at CDW and SDW formation in the TMDCs (Sec. 5.4).

From a theoretical point of view, it has often been argued that superconductivity is not possible in two-dimensional materials. This is due to the so-called Mermin-Wagner theorem which states that in two or less dimensions, no spontaneous breaking of continuous symmetries at finite temperatures is possible.[1] This means, as Hohenberg showed [187], that superconductivity or long-range crystalline order cannot exist in strictly two or less dimensions.

Several reasons can be stated for why superconductivity and other long-range order can indeed exist in 2D; we give two arguments. First of all, although the systems at hand are mostly treated as being effectively two-dimensional in our calculations, they are not purely two-dimensional in the sense that they have a certain height due to the distance between the chalcogen atoms and the transition metal atoms or the hydrogen atoms and the carbon atoms, respectively; furthermore, monolayers of 2D materials often exhibit a crumbling in the z-direction [149]. Secondly, even if the systems are

[1] Mermin and Wagner originally showed that no long-range ferromagnetic or antiferromagnetic order can exist in the Heisenberg model in two dimensions [186].

purely two-dimensional, i.e., also not supported by substrates, and longe-range order is suppressed by thermal fluctuations, they can exhibit quasi-long-range order in the form of a Berezinskii-Kosterlitz-Thouless transition [188, 189]. This can, for example, lead to a superconducting state with a lowered critical temperature [36].

As pointed out before, an important aspect that has not been investigated in detail in the existing literature is the influence of the Coulomb interaction on the instabilities. In the following discussion on the TMDCs, we aim at improving this situation and use the material-realistic Coulomb interaction as derived in the previous chapter to calculate realistic values for the effective Coulomb repulsion and its influence on the superconducting phase, the charge ordered phase and the spin ordered phase. By investigating this influence and additionally taking the interaction between electrons and phonons into account, we build up a database for the TMDCs, similar to the plain values of the Coulomb interaction and the plasmon dispersion discussed in the previous section.

5.1. Conventional superconductivity in TMDCs

The essential ingredient to a superconducting phase are the Cooper pairs which are formed by two electrons as described in Sec. 2.6 and Fig. 2.4. When using the term conventional superconductivity we mean that the binding responsible for this pair formation is mediated by the interaction of electrons and phonons. To theoretically describe this interaction we use Density Functional Perturbation Theory for the lattice dynamics and Eliashberg theory for the superconducting phase, see Secs. 2.5.2 and 2.6.2, respectively. At first, we discuss the phononic properties of the TMDCs using the examples of $MoSe_2$ and NbS_2. Afterwards, we take a look at the electron-phonon and the electron-electron interaction and finally characterize the superconducting phase via the results for the critical temperature. We mention that the phonon calculations presented in this section are fully ab-initio, which means that they include band structure changes beyond rigid shifts on a DFT level.

5.1.1. Phonons

The TMDCs have unit cells with three atoms which results in nine different phononic modes. Three of these modes are acoustic, which means that they have zero frequency ω for vanishing wave vectors $q \to 0$, while the other six have optical character with higher frequencies according to Sec. 2.5.1. Two of the acoustic modes stem from in-plane longitudinal or transversal vibrations (LA and TA). At small wave vectors, they have a linear dispersion and a larger energy than the third, quadratic mode (ZA) that stems from the out-of-plane motion. As we will see later on, these acoustic modes have the largest influence on the superconducting and CDW properties of the materials at hand. We will also see that their dispersion can depend strongly on the electron doping level.

In the metallic regimes upon electron doping (semiconducting TMDCs) or at half filling (metallic TMDCs), the phonon dispersions can become imaginary at wave vectors away from $q \sim 0$. These imaginary frequencies are shown as negative frequencies in the graphs that we plot. They are signs of a lattice instability or CDW phase, which we discuss in Sec. 5.4.1.

As one can see from the corresponding figures in Appx. B and Figs. 5.1 and 5.2, the phonon dispersions of the semiconducting or metallic TMDCs, respectively, are rather similar. Despite the fact that the instability occurs at different wave vectors in the doped semiconducting and the metallic materials, see Sec. 5.4.1, the main difference is the magnitude of the frequencies. In general, lighter atoms lead to higher frequencies, see Sec. 2.5.1 and Eq. (2.69); thus, for example, WSe_2 has smaller frequencies than both WS_2 and $MoSe_2$ because molybdenum is lighter than tungsten and sulfur is lighter than selenium. This trend can be seen for all materials.

Semiconductors

The phononic dispersions of semiconducting TMDCs have previously been calculated in Ref. [191] for MoS_2 and WS_2 and in Ref. [190] for $MoSe_2$. Electron doping in MoS_2 and its effect on the phonons has been investigated in Refs. [192, 193]. For the other semiconducting TMDCs the effects of electron doping on the phonons are studied here for the first time. We look mostly at the example of $MoSe_2$ and show the phonon dispersion in Fig. 5.1.

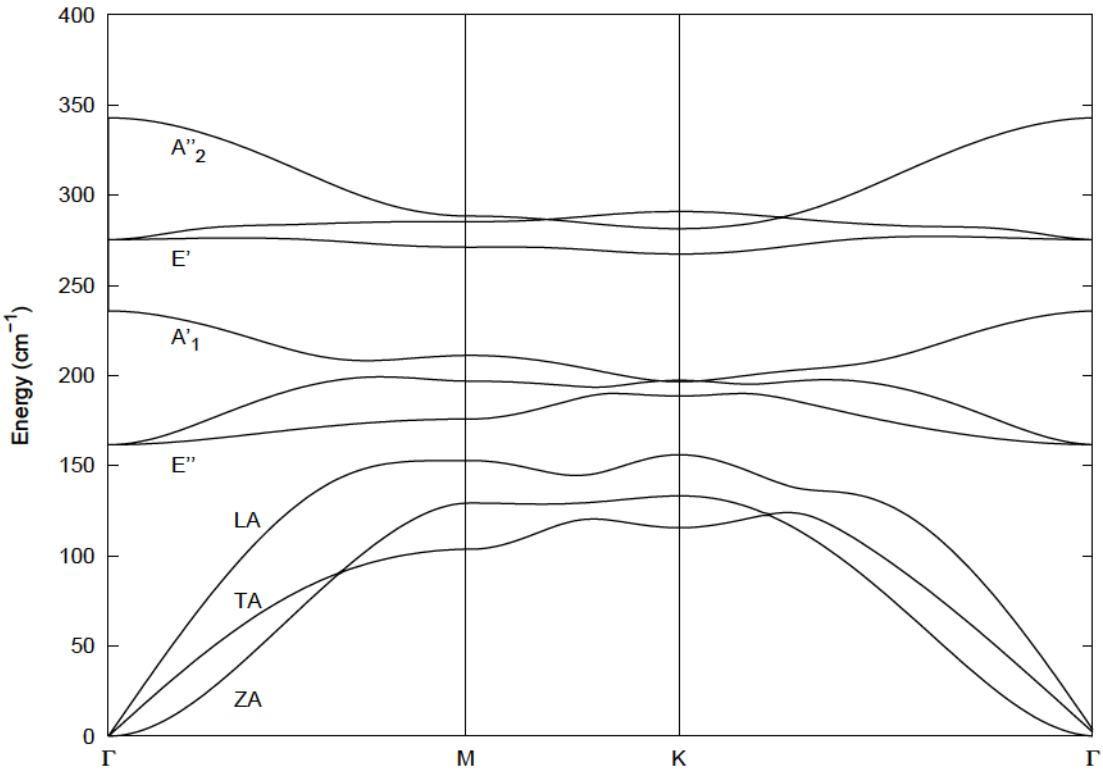

Figure 5.1.: Phononic dispersion in undoped $MoSe_2$ from our DFPT calculations. The annotations indicate the character of the corresponding vibrations or Raman modes, [190].

The three acoustic modes reach their maximum frequency at $\sim$115 cm^{-1} for the TA mode, $\sim$133 cm^{-1} for the ZA mode and $\sim$156 cm^{-1} for the LA mode.[2] The optical phonons are well seperated from the acoustic ones with two distinct groups at higher frequencies. Especially the E" and E' Raman modes [190] have a rather flat dispersion; they are degenerate at $q = 0$ with frequencies $\sim$162 cm^{-1} and $\sim$275 cm^{-1}, respectively. The other two optical modes, called A'$_1$ and A"$_2$, are the only modes with a negative dispersion, i.e., lower frequencies for larger wave vectors. They have frequencies in the range of $\sim$195 cm^{-1} to $\sim$240 cm^{-1} and $\sim$285 cm^{-1} to $\sim$345 cm^{-1}, respectively.

Upon electron doping, the LA phonon mode softens strongly and eventually becomes unstable with imaginary frequencies around the M point (see Figs. 5.3 and 5.16). Parts of the other phonon modes also experience a weaker softening. These softened or imaginary frequencies will be discussed in more detail in Secs. 5.1.2 and 5.4.1.

[2] If one wanted to represent these phonons by a single Einstein frequency for large wave vectors in a Hubbard-Holstein model, a possible choice would be to use the $\sim$16.5 meV of the ZA mode, since this mode is the least normalized by the electrons.

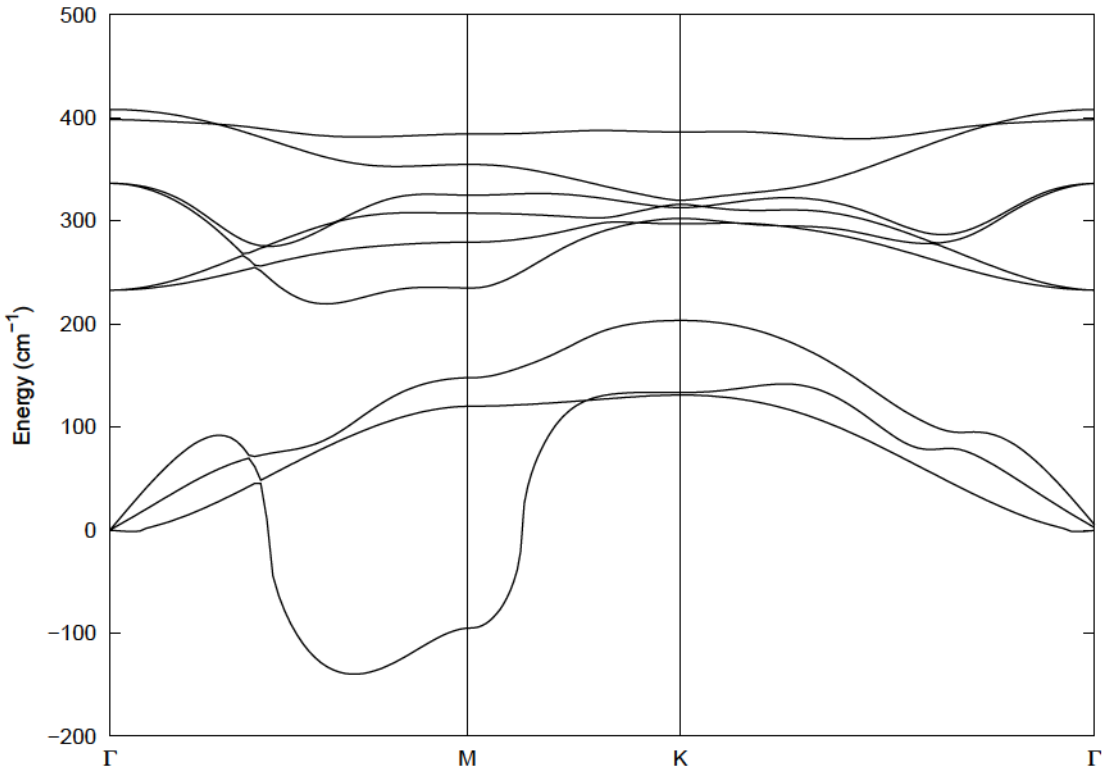

Figure 5.2.: Phononic dispersion in undoped NbS_2.

Metals

While $NbSe_2$ and its phonon dispersion have been investigated before both in the bulk and in the monolayer, [194], the phonon dispersion in NbS_2 has so far only been studied for the bulk material [195] as far as we know. Thus, we focus on NbS_2 and give its phonon dispersion as obtained from DFPT calculations in Fig. 5.2.

A distinct feature in the phonon dispersions of $NbSe_2$ (see Fig. B.3) and NbS_2 are the imaginary frequencies between Γ and M which stem from a strongly softened acoustic mode. They are a sign of a lattice instability as discussed in Sec. 5.4.1. The acoustic phonons are well seperated from the optical bands and have frequencies of up to $\sim 205\,\mathrm{cm}^{-1}$ (TA mode at K point). The optical dispersions do not fall into two groups as it was the case for $MoSe_2$. Instead, they lie between $\sim 220\,\mathrm{cm}^{-1}$ and $\sim 410\,\mathrm{cm}^{-1}$, where the minimal frequency results from a band that is softened similar to the softened acoustic band. At $q = 0$ the optical phonons have two degenerate bands at $\sim 235\,\mathrm{cm}^{-1}$ and $\sim 335\,\mathrm{cm}^{-1}$, respectively, and two nearly degenerate bands around $\sim 400\,\mathrm{cm}^{-1}$.

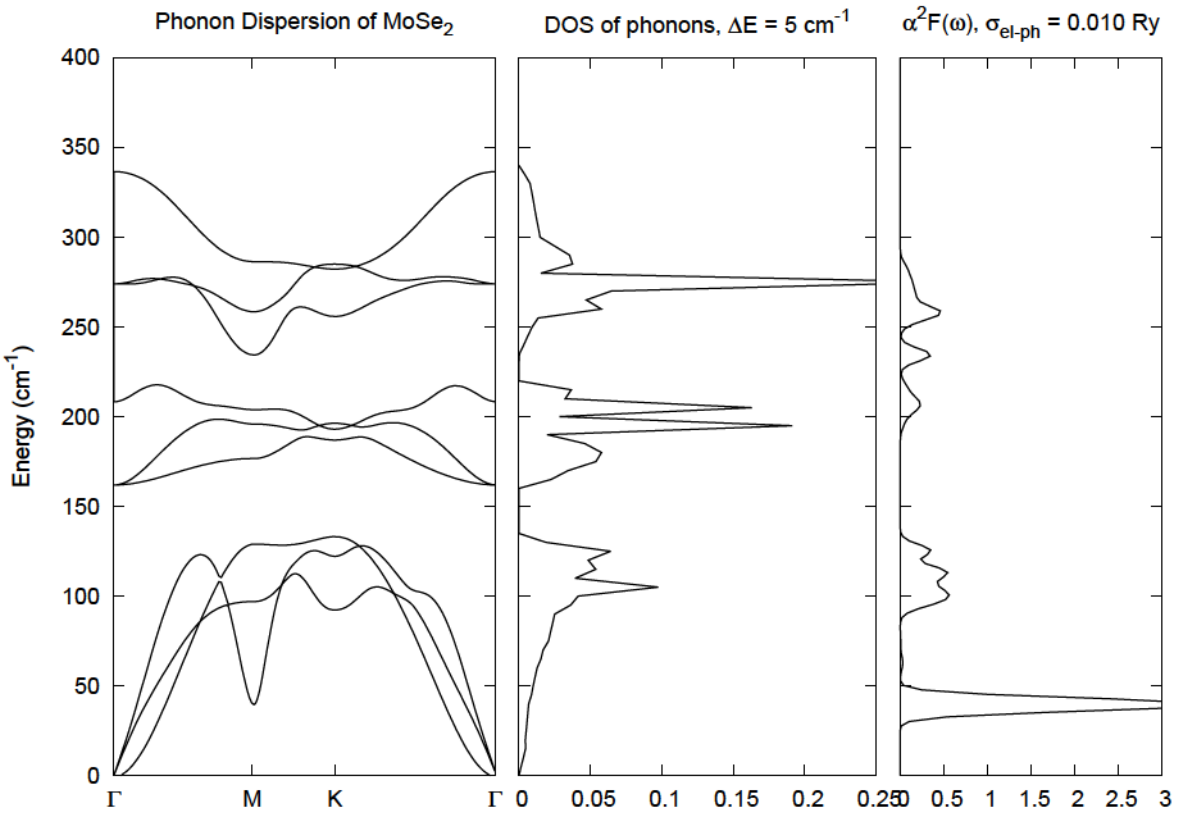

Figure 5.3.: Phononic dispersion, DOS [see Eq. (2.82)] and α^2F [see Eq. (2.81)] for $MoSe_2$ under electron doping $x = 0.08$.

5.1.2. Electron-phonon interaction

Superconductivity in monolayer and few-layer TMDCs has experimentally been investigated by several groups [11, 22, 23, 26, 28, 36], while the theoretical effort to understand the electron-phonon interaction responsible for the superconducting phase has focussed on monolayer MoS_2 [192, 193]. Here, we study again the case of a monolayer of $MoSe_2$ under electron doping. The results for the phonon dispersion, the phononic DOS and the spectral function α^2F that quantifies the electron-phonon interaction [see Eq. (2.81 and Secs. 2.5.3 and 2.6.2] are shown for an examplary doping of $x = 0.08$, i.e., above the Lifshitz transition, in Fig. 5.3.

When comparing to the phonon dispersion of pristine $MoSe_2$ in Fig. 5.1, one can see an overall softening of the phonon dispersion towards lower frequencies at several wave vectors. The acoustic phonons now lie well below $150\,\mathrm{cm}^{-1}$ since the additional electrons have the strongest effect on the LA mode around the M point with a change of more

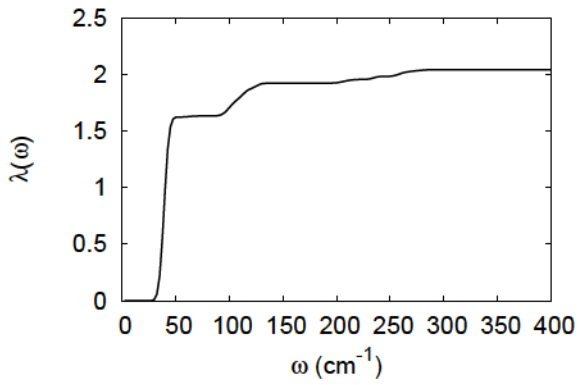

Figure 5.4.: Frequency-dependent electron-phonon interaction $\lambda(\omega)$ in $MoSe_2$ at electron doping $x = 0.08$ obtained by setting the upper boundary of the integration in Eq. (2.83) to ω, which is equal to setting $n = n'$ in Eq. (2.99). For $\omega \to \infty$, the interaction is equal to the value of $\lambda = 2.03$ entering the Allen-Dynes equation, see Tab. 5.3.

than $100\,\mathrm{cm}^{-1}$. The TA mode also softens, but around the K point, while the ZA mode is unaffected. The optical phonons are still split up into two subsets but partly softened. While both the E" modes and the A"$_2$ mode are basically unchanged, the A'$_1$ mode softens at $q = 0$ and the E' modes soften around $q = \mathrm{M}$.

In the middle panel of Fig. 5.3, we see the phononic density of states. There are several peaks around $100\,\mathrm{cm}^{-1}$, $200\,\mathrm{cm}^{-1}$ and $275\,\mathrm{cm}^{-1}$ which correspond to flat regions in the dispersion. The right panel shows the corresponding values of the electron-phonon spectral function α^2F, see Eq. (2.81). Since this function incorporates both the phonon DOS as well as the electron-phonon interaction, we can now distinguish between the influences of these two quantities. We see that α^2F has considerable values of 0.5 and less around the maxima of the acoustic phonons and, less pronounced, in the optical region between $200\,\mathrm{cm}^{-1}$ and $300\,\mathrm{cm}^{-1}$ where the DOS of the phonons is large. This can be seen as a DOS effect which means that the electrons couple rather weakly to the ZA and TA acoustic modes as well as the optical modes. However, we can also identify a very strong coupling to the softened LA mode below $50\,\mathrm{cm}^{-1}$ around M with values exceeding $\alpha^2F \sim 3$. Since the DOS in this region is rather low, this effect is caused by a strong electron-phonon interaction.

For a better justification of and more insight into the claims in the last paragraph, we look at the frequency-dependent electron-phonon interaction $\lambda(\omega)$, which is the integrated weight of the spectral function $\alpha^2F(\omega)$. In this way we can distinguish between the contributions at different frequencies to the full effective electron-phonon interaction λ.

Table 5.1.: Electron-phonon coupling λ [see Eq. (2.83)] and phonon frequency $\omega_{\log}$ [see Eq. (2.103)] in electron doped TMDCs below, directly at and above the Lifshitz transition. Note that the values of the doping x for different materials are not necessarily comparable.

Material	MoS_2	$MoSe_2$	WS_2	WSe_2
x_{below}	0.05	0.05	0.02	0.03
λ_{below}	0.40	0.43	0.26	0.42
$\omega_{\log,\,\text{below}}$ (cm^{-1})	183	118	148	85
x_{at}	0.075	0.08	0.05	0.05
λ_{at}	0.78	2.03	0.65	0.98
$\omega_{\log,\,\text{at}}$ (cm^{-1})	151	50	121	62
x_{above}	0.087	0.09	0.08	0.08
λ_{above}	1.05	*CDW*	1.20	*CDW*
$\omega_{\log,\,\text{above}}$ (cm^{-1})	134	*CDW*	97	*CDW*

From the results in Fig. 5.4, we see that the main contribution, which already amounts to more than three quarters of the full λ, is given by the softened phonon mode which lies slightly below $50\,\text{cm}^{-1}$ for $x = 0.08$. Most of the rest of the effective interaction comes from the acoustic modes in their flat region above $100\,\text{cm}^{-1}$. Finally, about 5 % of the full λ results from the coupling to optical phonons at higher frequencies.

The strong coupling to the LA mode around the M point that softens upon electron doping can be understood when we look at the Fermi surface of doped $MoSe_2$ in Fig. 3.7. Once the Lifshitz transition has occurred, a phonon mode with wave vector M can connect Fermi pockets around K and Σ as well as two Σ pockets. This situation is similar to the so-called (partial) Fermi surface nesting that was often linked to the formation of CDWs [196].

We now look at the evolution of the electron-phonon interaction with doping for the semiconducting TMDCs. In Tab. 5.1, we show the values below, approximately at, and above the Lifshitz transition for the averaged interaction λ [see Eq. (2.83)] and the typical phonon frequency $\omega_{\log}$ [see Eq. (2.103)] that are part of the Allen-Dynes equation [see Eq. (2.106)] which we use to calculate the critical temperature of superconductivity in Sec. 5.1.4. One again sees that the phonon frequency depends on the mass of the atoms involved which means that $MoSe_2$ has a lower frequency than MoS_2 and WSe_2 has a lower frequency than $MoSe_2$ at low doping, i.e., only weak softening. Below the Lifshitz transition, the coupling is $\lambda \sim 0.4$ or less which results in a vanishing critical temperature (see Tab. 5.3). Once the transition takes place, there is a strong enhancement of λ to values above $\lambda \sim 1.0$ which shows that we need a theory that is able to treat strong

coupling such as the Eliashberg theory. The typical frequency is shifted towards $0\,\mathrm{cm}^{-1}$. For the selenide materials, the lattice instability occurs already below $x \sim 0.1$ which means that the calculation of $\omega_{\log}$ is not possible due to the finite values of α^2F at negative, i.e., imaginary frequencies.[3] The Lifshitz transition occurs at lower doping in the two tungsten materials since the valleys around K and Σ are closer together in energy in these materials and the shift of the Σ-valley upon doping is stronger (as predicted from our DFT calculations)[4].

5.1.3. Influence of Coulomb interaction

Although superconductivity has been around for more than a hundred years, the role of the Coulomb interaction in this field is still far from being fully understood. Besides the possibility to get an unconventional superconducting phase purely from the Coulomb interaction between the electrons, which leads to an order parameter with lower symmetry than the standard s-wave (see, for example, Sec. 5.3 and [197]), the interaction can both enhance and suppress the critical temperature in the conventional electron-phonon superconductivity [198]. Here, we focuss on the Coulomb repulsion which reduces T_c in the formalism of Eliashberg theory (see Sec. 2.6.2). The possible enhancement has also been a subject of recent research [199], including discussions of the dynamic, i.e., plasmonic part of the Coulomb interaction [173, 174].

In standard BCS theory, the Coulomb repulsion is only implicitly included in the effective attraction of the electrons (see Sec. 2.6.1). More advanced treatments of phonon-mediated superconductivity use the Eliashberg theory, often in the Allen-Dynes approximation (see Sec. 2.6.2), and usually include the Coulomb repulsion via the effective Morel-Anderson constant μ^*, see Eq. (2.104) and [114]. This constant can be obtained in several ways such as fits to experimental values for the critical temperature. In a lot of cases, it is simply assumed to have a certain value between 0.1 and 0.2, e.g. $\mu^* = 0.13$ [81, 116, 192]. Other studies including calculations of μ^* also find values in this range, see for example Refs. [200–202]. We aim at a better, material-realistic and specific description of the effective Coulomb repulsion for the monolayer TMDCs which is not available yet. To this end, we perform calculations for the averaged Coulomb interaction μ [see Eq. (2.100)] from ab-initio data via our own RPA code which uses the Coulomb

[3] Since this is also the case for the undoped metallic TMDCs, we have not discussed the electron-phonon coupling in NbS_2 and $NbSe_2$.

[4] This effect can also be seen from Fig. 3.8 where doping is included only as a rigid shift of the Fermi level.

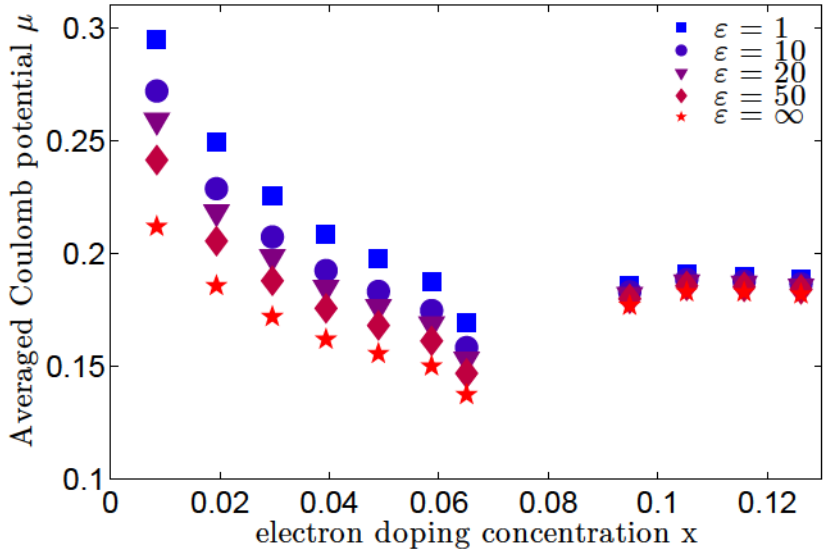

Figure 5.5.: Dependence of the averaged Coulomb repulsion μ on the electron doping concentration x, subject to various ε_{sub} of the dielectric environment.

interaction presented in the previous chapter.[5] The parts of our results that show only data for MoS_2 have already been published by the author in Ref. [159].

First of all, we use Eq. (2.100) to calculate the effective Coulomb coupling constant μ. The results are shown in Fig. 5.5 for different dielectric environments of a MoS_2 monolayer and in dependence on the electron doping concentration. We see a decrease of μ with increasing doping up to $x \lesssim 0.07$ from values of $\mu \sim 0.3$ to $\mu < 0.2$ for the freestanding layer ($\varepsilon_{\text{sub}} = 1$); for higher doping levels, μ is nearly independent of the doping. In the low-doping regime, $x \lesssim 0.07$, where only two Fermi pockets around the two K points are present, the coupling μ is renormalized by up to $\sim 30\%$ via external screening, resulting in a decrease of μ with increasing dielectric constant of the environment. In contrast, at higher doping concentrations μ is clearly much less sensitive to the dielectric environment, and variations of μ due to external screening are limited to $\lesssim 10\%$.

If we account for the multi-valley structure of the Fermi surface (see Fig. 3.7), μ is no longer a simple scalar but becomes a matrix in the electronic valleys. To further investigate the effect of the dielectric environment, we discuss this matrix structure of $\boldsymbol{\mu}$. For low doping concentrations, where only the two valleys around the K points are

[5] For this subsection, the calculations use band structures of undoped TMDCs and treat the doping as a rigid shift of the Fermi level. This changes the values of the *critical* electron doping at which additional Fermi pockets arise but does not influence the trends and conclusions since the relative change of the minima at K and Σ is not important here.

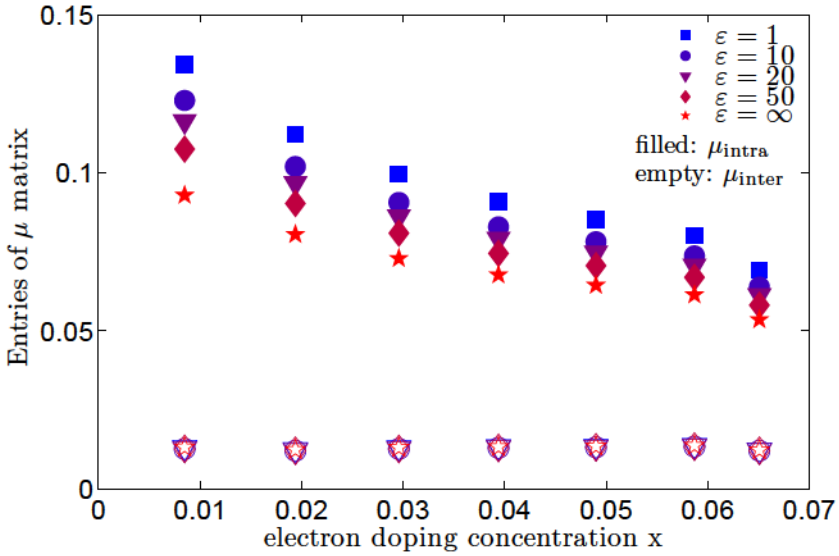

Figure 5.6.: Values of the 2×2-matrix $\boldsymbol{\mu}$ [cf. Eq. (5.1)] for low doping concentrations and their dependence on the dielectric environment.

occupied, we obtain the following structure

$$\boldsymbol{\mu}_{\text{low}} = \begin{pmatrix} \mu_{\text{intra}} & \mu_{\text{inter}} \\ \mu_{\text{inter}} & \mu_{\text{intra}} \end{pmatrix}, \tag{5.1}$$

where the states $\{\boldsymbol{k}, \boldsymbol{k}'\}$ in Eq. (2.100) are in the same valley for μ_{intra} while they are in different valleys for μ_{inter}. The sum of all matrix elements yields the total coupling constant μ. A comparison of external screening effects on intra- and intervalley Coulomb scattering (Fig. 5.6) shows that essentially only the intravalley scattering is affected by the dielectric environment; the intervalley scattering experiences no notable change. These observations can be explained intuitively.[6] External screening is most effective when the separation ($\sim 1/q$) of the interacting charges inside the monolayer is larger than the distance $\sim \frac{1}{2}d$ to their image charges in the environment but smaller than the internal Thomas-Fermi screening length $1/q_{\text{TF}}$ [cf. Eq. (2.57)], i.e., for $q_{\text{TF}} < q < \frac{2}{d}$ (cf. Fig. 4.7). As a consequence, the influence of the substrate weakens as soon as $q_{\text{TF}} \gtrsim \frac{2}{d}$. Using the effective thickness of $d \approx 9.1\,\text{Å}$, a Thomas-Fermi wave vector $q_{\text{TF}} = 2\pi \text{e}^2 N(E_{\text{F}})/(A\,\varepsilon_1(q_{\text{TF}}))$, and a background dielectric constant on the order of $\varepsilon_1(q) \approx \varepsilon_\infty = 9.3$ for $q > \frac{2}{d}$, we find that the substrate influence is minor as soon as the density of states at the Fermi level exceeds $N(E_{\text{F}}) \gg 0.19\,/\text{eV}$ per unit cell. In MoS_2, we have $N(E_{\text{F}}) \approx 0.4\,\text{eV}^{-1}$ and $N(E_{\text{F}}) \approx 2\,\text{eV}^{-1}$ for low ($x < 0.07$) and high electron doping

[6] See also the discussion in Sec. 4.3.

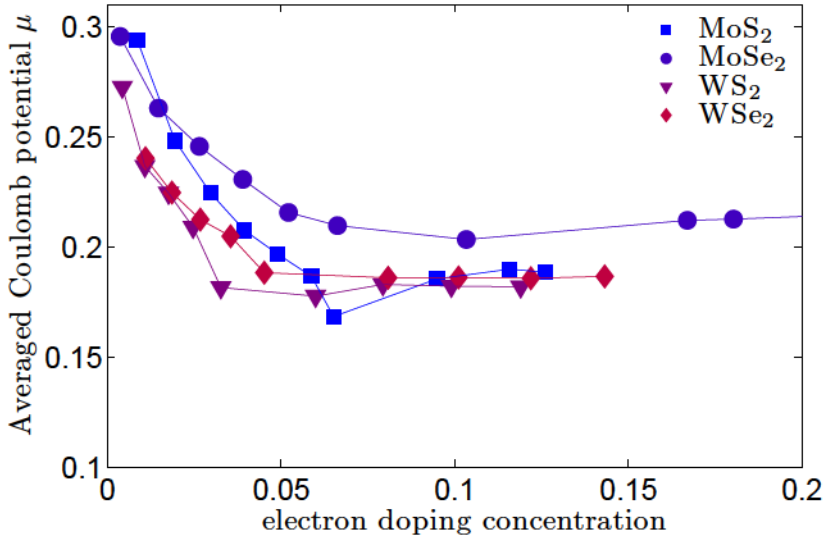

Figure 5.7.: Development of averaged Coulomb interaction μ with electron doping in several TMDCs.

Table 5.2.: Values of the averaged Coulomb interaction μ and the density of states per spin at the Fermi level $N(E_F)$ for different TMDCs, shown as averages of several values at high doping (semiconductors) or for the undoped, half filled material (metals). For $N(E_F)$ of the semiconductors, see also Fig. 3.8.

Material	MoS_2	$MoSe_2$	WS_2	WSe_2	NbS_2	$NbSe_2$
$\overline{\mu}$	0.189	0.214	0.182	0.186	0.235	0.217
$\overline{N(E_F)}$ (1/eV)	1.02	1.24	0.99	1.02	1.40	1.42

concentrations ($x > 0.07$), respectively, which means that substrate influence is weak, especially in the regime of high doping concentrations. However, for sufficiently low doping concentrations, the scattering inside the same K- or K'-valley can be controlled via the substrates.

We now compare the results for the averaged Coulomb repulsion μ in several TMDCs. The dependence of μ on electron doping in the different semiconducting TMDCs is shown in Fig. 5.7. One observes a similar trend in all TMDCs, namely a descrease from values between 0.25 and 0.3 to a constant value around 0.2 upon increased electron doping. The small difference of $MoSe_2$ to the other three materials can be explained in parts by the slightly larger DOS at the Fermi level, see Fig. 3.8, which leads to a larger value of the Coulomb repulsion, see Eq. 2.101. The tungsten materials have a lower DOS at the Fermi level than the molybdenum materials in the low-doping regime which may be the reason for the slightly lower values of μ.

The similarity of the values of μ at high doping, where all K and Σ valleys are occupied, can also be seen in Tab. 5.2. There, we show the average μ in the full metallic regime for all six TMDCs, i.e., at high doping for the semiconductors and for the undoped/half-filled case for the metals. This average Coulomb interaction is between 0.18 and 0.24 for all six materials. Again, one reason for the overall similar values as well as the slightly larger values in $MoSe_2$ and the niobium compounds can be the DOS at the Fermi level, because $\mu = N(E_F)\overline{W}$ in a simple picture with local interaction $\overline{W}$, see Eq. (2.101).

Eq. (2.101) can also be used to gain insight into the the range of values that is possible for the averaged Coulomb repulsion. An upper limit for μ can be calculated via the unitary limit of the Coulomb interaction, $V \to \infty$. This leads to the following estimation for the maximum of the screened onsite interaction, derived from Eq. (2.51):

$$\overline{W}_{\max} = \frac{V}{1 - V \cdot \Pi} \overset{V\to\infty}{=} -\frac{1}{\Pi} \overset{q\to 0}{=} \frac{1}{2N(E_F)} \tag{5.2}$$

where we have used the long-wavelength limit of the polarization, see Eq. (2.58), and taken into account that the interaction is screened by all electrons, which leads to the factor of 2 due to a (in our case) spin-degenerate DOS. Since the prefactor in the calculation of μ is only the DOS per spin, this leads to an estimation of

$$\mu_{\max} = N(E_F)\overline{W}_{\max} = \frac{1}{2} \tag{5.3}$$

for the upper limit of the Coulomb repulsion. With a μ of up to 0.3 in the low-doping regime of the semiconducting TMDCs, our values are at 60 % or less of this maximal value.

In chapter 4, we discussed a pseudo-Resta model as an improvement of the simple fit of the Coulomb interaction, see Sec. 4.2.1. Using this model to calculate the Coulomb interaction instead of the simple model used so far has only a minor influence on the values for μ, as is apparent from Fig. 5.8. In the low-doping regime, the values of the pseudo-Resta model are slightly higher by an amount of less than 2 %, while the change in the high-doping regime is barely visible.

As a last step, we show the change of the Coulomb pseudopotential μ^* [see Eq. (2.104)] with doping and dielectric environment for the case of MoS_2 in Fig. 5.9. For free-standing MoS_2 we observe a decrease of μ^* from $\mu^* > 0.25$ to $\mu^* \lesssim 0.15$ for $x \lesssim 0.07$, which is caused by the corresponding decrease in μ and the decrease in the phonon frequency $\omega_{\log}$ (see Tab. 5.1 and [193]). At larger electron doping concentrations, μ is basically

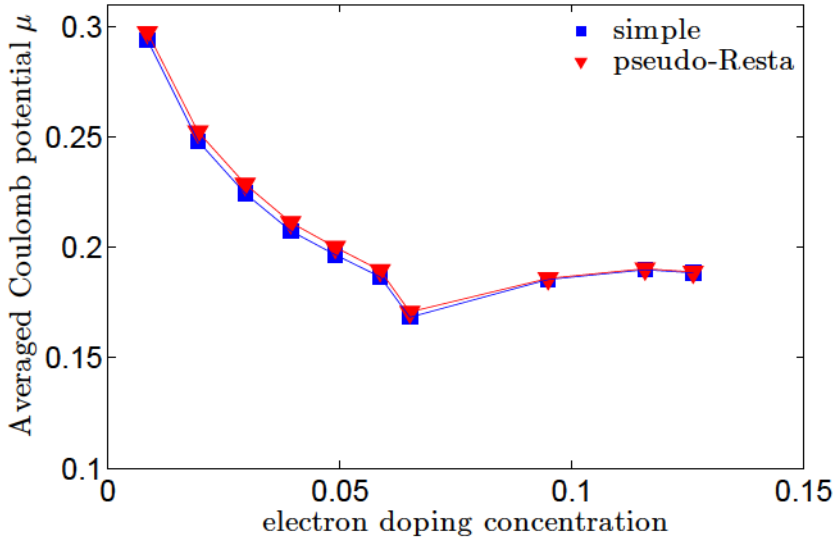

Figure 5.8.: Comparison of the averaged Coulomb interaction μ for electron doped MoS_2, resulting from the simple Fit for the interaction and the pseudo-Resta fit.

constant and we have $\mu^* \sim 0.13$. For MoS_2 embedded in a metallic environment, μ^* shows essentially the same trend with the only difference in comparison to the free-standing case being a reduction of μ^* by up to 25 %, particularly at low doping, which could shift the onset of the superconducting phase to a lower doping concentration than the critical concentration for the freestanding layer.

A significant T_c is only reached when the exponent in Eq. (2.106) is close to -1 or larger, especially when the electrons mainly couple to acoustic phonons as it is the case for the TMDCs (cf. Fig. 5.3) and, thus, the frequency $\omega_{\log}$ is rather small, e.g. $T_c \gtrsim \frac{\hbar\omega_{\log}}{1.2k_B} e^{-2}$. To achieve this, $\lambda > 3\mu^*$ has to be realized for the range of $0.1 < \mu^* < 0.3$ found here. From the comparison of μ^* and $\lambda/3$ in Fig. 5.9, we see that a significant T_c (as occurring for $\lambda > 3\mu^*$) can only be observed once $x \gtrsim 0.07$, i.e., when both valleys in the conduction band are occupied by electrons. This result for the strong effect of the Lifschitz transition on the critical temperature is true for all four semiconducting TMDCs discussed here, as we will see in the next section, see Tab. 5.3.

We thus conclude that the frequent use of a constant for the Coulomb pseudopotential, e.g. $\mu^* = 0.13$ [81, 116, 192], is not sufficient in the case of electron doped MoS_2 to describe the influence of the Coulomb interaction directly at the transition to the superconducting phase. However, $\mu^* \sim 0.13$ yields a sufficient description of the Coulomb repulsion deep in the superconducting phase.

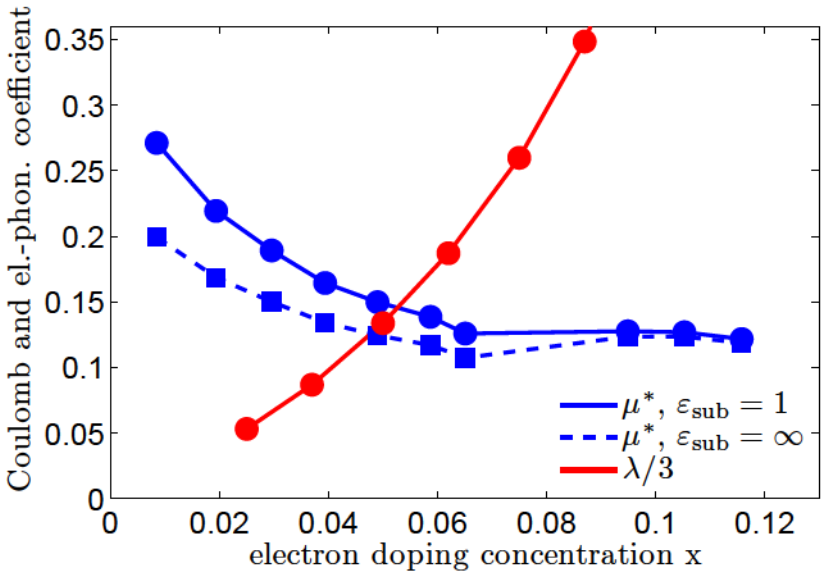

Figure 5.9.: Development of effective Coulomb interaction μ^* and electron-phonon interaction λ with electron doping in MoS_2. The values of λ are scaled by a factor of 3 for comparability.

5.1.4. Critical temperature and phase diagram

Experimentally, evidence of a superconducting phase in few-layer MoS_2 was first found by Ye et al., [22], where a dome shape of the critical temperature upon electron doping via electic field gating was observed, see Fig. 1.2. The experimental phase diagram included a rapid onset of superconductivity at a certain critical doping and a maximum critical temperature around 10 K at doping level $x \approx 0.1$. This phase diagram shares some similarities with the phase diagram observed in high-temperature superconductors [97] which is one reason for the interest of the scientific community in these results. High-temperature superconductors also share some similarities with the TMDCs concerning their crystal structure due to the layered structure of the cuprates. The doping dependence of superconductivity in the semiconducting TMDCs was also found in theoretical studies on MoS_2 [192, 193] as well as experimental investigations of $MoSe_2$ [28].

A feature of superconductivity in metallic TMDCs is its enhancement upon pressure which was found in Ref. [203] for bulk $NbSe_2$ and in Ref. [204] for bulk NbS_2. Furthermore, several studies have found that the critical temperature reduces with decreasing thickness of the few-layer MoS_2 [36] and $NbSe_2$ [11, 23, 26] (see also Fig. 1.1). The reason behind this reduction has not been clearly identified so far. One possibility that has been discussed in the literature [36] is enhanced Coulomb interaction due to the

Table 5.3.: Critical temperatures of superconductivity in electron doped TMDCs below, directly at and above the Lifshitz transition. To calculate these values, the values in Tab. 5.1 and the Allen-Dynes equation (2.106) were used. For comparability of the values of one material, a value of $\mu^* = 0.15$ is used in all cases. Note that the values of the doping x of different materials are not necessarily comparable.

Material	MoS_2	$MoSe_2$	WS_2	WSe_2
x_{below}	0.05	0.05	0.02	0.03
$T_{\text{c, below}}$ (K)	0.2	0.3	0.0	0.2
x_{at}	0.075	0.08	0.05	0.05
$T_{\text{c, at}}$ (K)	6.5	9.3	2.9	4.6
x_{above}	0.087	0.09	0.08	0.08
$T_{\text{c, above}}$ (K)	11.2	*CDW*	10.0	*CDW*

low dimensionality and the reduced screening of the system. From the results in the previous section on μ^*, we can already state that the drop in the critical temperature of TMDCs when going from the bulk or multilayer-system to a monolayer cannot be caused by this effect as far as our calculations go, because the values of the electron-phonon coupling (see Tab. 5.1) are much larger than the $\mu^* \approx 0.13$, which we find in the region of optimal doping independently of the dielectric environment of the MoS_2 monolayer. However, one topic that is not included in this thesis are the possible effects of disorder on the phase diagram. These effects can be very significant and can lead to a reduction of the critical temperature of the superconducting phase, especially in systems with low dimensionality [205].

From the results obtained so far, we can calculate the critical temperatures of the electron-doped semiconducting TMDCs using the Allen-Dynes equation (2.106) together with the values in Tab. 5.1. The resulting data with critical temperatures below, at, and above the Lifhitz transition is pesented in Tab. 5.3. We see that all four materials have a vanishing T_c below the Lifshitz transition and a rapid onset of the superconducting phase at the transition. The maximal critical temperatures reached for high doping concentrations are above 10 K. Due to the fact that the coupling to low-frequency acoustic phonons dominates in the TMDCs, we do not reach higher critical temperatures such as those calculated for functionalized graphene (see Sec. 5.2) despite the strong effective electron-phonon coupling evidenced by large values of λ.

Using our data as well as the data from [22] and [193], we can draw a generic phase diagram of the semiconducting TMDCs under electron doping, see Fig. 5.10. By increasing the doping level, our calculations predict that the materials first become metallic, then

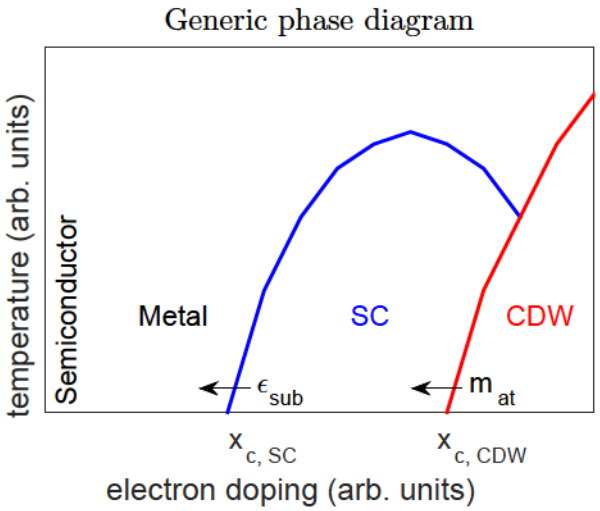

Figure 5.10.: Sketch of the generic phase diagram including the DFT, DFPT and Eliashberg results for semiconducting TMDCs upon electron doping.

turn superconducting and eventually obtain a CDW phase. The arrows indicate that increased substrate screening ε_{sub} can shift the onset of the superconducting phase towards lower values of the electron doping, while an increase in the atomic mass, i.e., the use of a heavier transition metal or chalcogen, leads to the formation of the CDW phase at lower doping concentrations due to lower phonon frequencies (see Sec. 5.1.2). While the coexistence of CDW phases and superconductivity was investigated for bulk, metallic 1T-TaS_2 [19], we are not aware of any experimental study that has investigated few-layer or monolayer systems of the semiconducting TMDCs under high electron doping and searched for a CDW phase. For high-temperature superconductors, a possible competition between superconductivity and CDW has been investigated for example in Ref. [206]. Whether superconductivity and the CDW phase coexist in metallic TMDCs and whether the superconducting order persists beyond the critical doping of the predicted CDW in the semiconducting TMDCs is unclear and has to be investigated experimentally.

5.2. Conventional superconductivity in functionalized graphene

Superconductivity in functionalized or doped, i.e., metallic graphene materials was already investigated in a lot of studies from both theory and experiment, [207–212] among others. In this thesis, we discuss the example of partially hydrogenated graphene C_8H_2 and look at the possibility of electron-phonon superconductivity. The electronic properties of this material were in parts already shown in Sec. 3.2. As was mentioned there, C_8H_2 is an interesting material since the placement of the hydrogen atoms on just one side of the carbon layer leaves the other side open for further functionalization, e.g. via substrates. Furthermore, the material is especially interesting concerning its superconducting properties due to the large phonon frequencies and resulting high critical temperatures that can be obtained in hydrogen and carbon compounds because of their small atomic masses.

The Coulomb interaction in graphene was already investigated by several studies, for example [34, 81]; we will not discuss it here and use a constant Coulomb pseudopotential of $\mu^* = 0.15$ when calculating the critical temperature of the superconducting phase. The doping that is needed to have free charge carriers in the otherwise semiconducting C_8H_2 is modeled again via additional or missing electrons, compensated by a homogeneous jellium background [cf. Eq. (2.13)]; this means that no chemical doping is considered explicitly.

5.2.1. Superconducting phase

To investigate the possibility of a superconducting phase that is induced by electron-phonon coupling in doped C_8H_2, we look at the phonon dispersion upon doping, the phononic density of states and the function α^2F. In Fig. 5.11 (top) we see the results for electron dopings of $x = -0.1$ and $x = -0.4$; the corresponding electronic band structures were shown in Fig. 3.15. Compared to the TMDCs (see Fig. 5.3 for $MoSe_2$), the phonon dispersion of C_8H_2 has a richer structure, consisting of 30 modes since there are 10 atoms in the unit cell. The three acoustic modes lie below $320\,\mathrm{cm}^{-1}$; they experience no substantial softening upon electron doping. Between $330\,\mathrm{cm}^{-1}$ and $1550\,\mathrm{cm}^{-1}$ we see a large group of 25 optical modes where only two modes around $500\,\mathrm{cm}^{-1}$ are strongly softened. Seperated from the other optical modes, two C-H stretching modes lie between

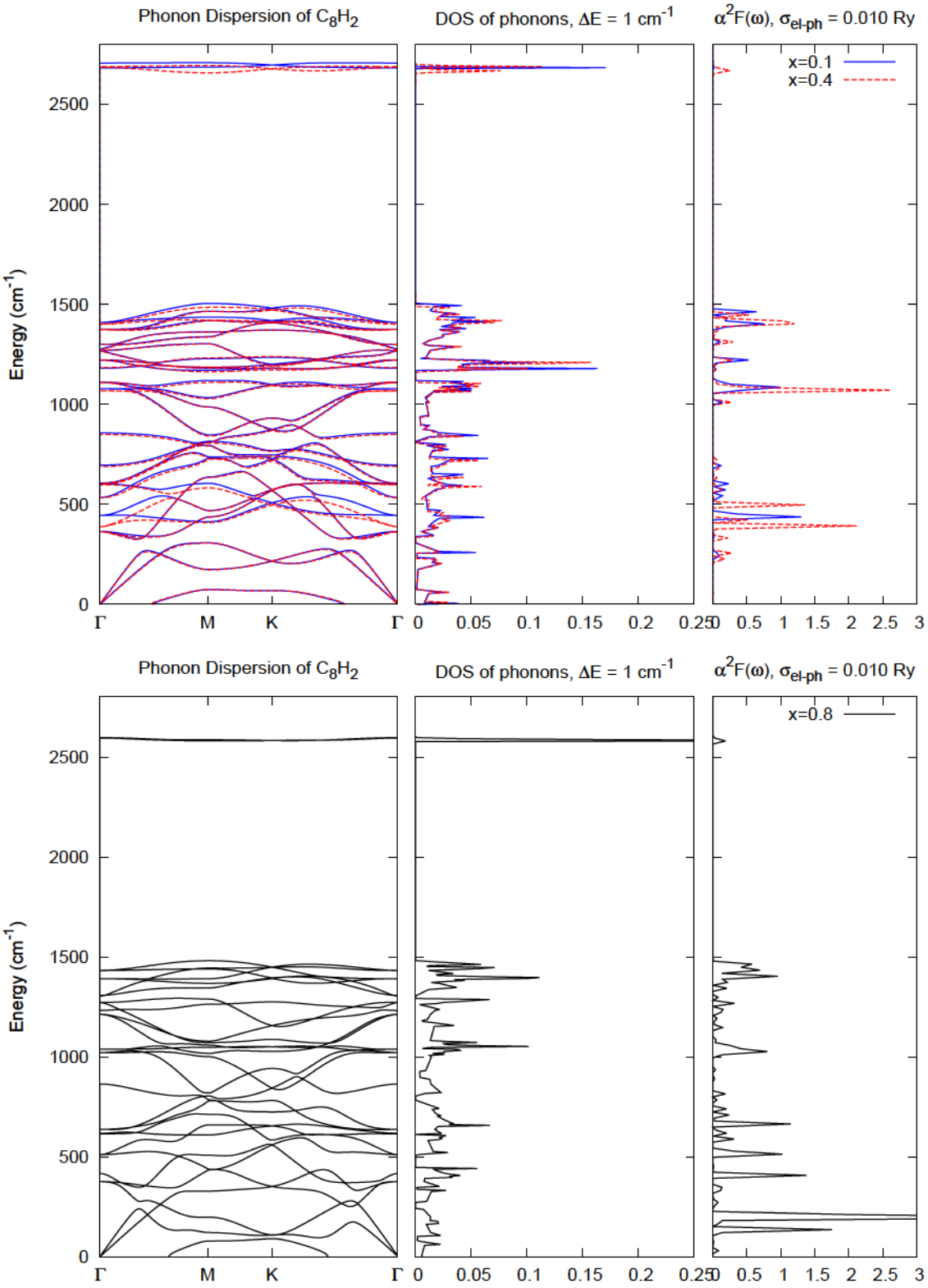

Figure 5.11.: Phononic dispersion, DOS and α^2F for C_8H_2 under electron doping (top) and hole doping (bottom). The ZA-mode is unstable around Γ due to the fact that the atomic structure is not fully relaxed for symmetry reasons; cf. Sec. 3.2.

$2680\,\mathrm{cm}^{-1}$ and $2730\,\mathrm{cm}^{-1}$. They are very similar to the high-energy optical modes in graphane [207] and show a small softening upon electron doping. Since they have a very flat dispersion, the DOS of these two modes is rather large. Additionally, there is one other peak in the phononic DOS around $1250\,\mathrm{cm}^{-1}$; besides these two features, the phononic DOS has values at or below $0.05\,\mathrm{eV}^{-1}$.

Via the third panel in Fig. 5.11 (top), showing the values of the function α^2F, we can once again distinguish between DOS and electron-phonon coupling effects (cf. Sec. 5.1.2). The acoustic modes and the two C-H stretching modes have only marginal values for α^2F despite their finite DOS which shows that the coupling of the electrons to these modes is rather weak. Futhermore, the electrons do not couple strongly to the modes around $1250\,\mathrm{cm}^{-1}$ which have a peak in the DOS. Instead, the coupling is strong for the optical modes between $1000\,\mathrm{cm}^{-1}$ and $1250\,\mathrm{cm}^{-1}$ as well as for the modes around $500\,\mathrm{cm}^{-1}$. The sizeable values of α^2F just below $1500\,\mathrm{cm}^{-1}$ can be attributed to both the coupling and the DOS.

In the case of hole doping [see Fig. 5.11 (bottom) for $x = 0.8$ removed electrons or additional holes per unit cell of C_8H_2], the acoustic phonon bands are not anymore decoupled from the optical modes. This is a sign for the strong softening of the low-frequency optical phonons. Rather strong softening can also be seen for the C-H stretching modes with a shift of up to $100\,\mathrm{cm}^{-1}$. Furthermore, these two modes have again a large DOS, but the coupling to the electrons is almost negligible as can be seen from $\alpha^2F \sim 0$. The other optical modes have values of $\alpha^2F \lesssim 1$ which shows that they couple significantly to the electrons, similar to the case of electron doping. What is different for hole doping, though, is that there is large coupling in the acoustic frequency range below $250\,\mathrm{cm}^{-1}$ resulting in two peaks in α^2F. This difference can be explained via the different Fermi surfaces of C_8H_2 upon electron (see Fig. 3.15) and hole doping (see Fig. 3.16) and the corresponding orbital characters (see Fig. 3.17). In the case of electron doping, the Fermi surface consists of two (three) partially degenerate Fermi pockets around Γ before (after) the Lifshitz transition, and the relevant electrons have purely carbon p_z-character. Upon hole doping, a hole pocket around M in the highest valence band arises and the corresponding conduction electrons have carbon p_z- as well as hydrogen s-character. The coupling to the low-frequency modes in the latter case is, thus, also due to these hydrogen electrons.

Similar to the discussion of $MoSe_2$ in Sec. 5.1, we now have a look at the frequency-dependent electron-phonon interaction, see Fig. 5.12. For the electron-doping levels

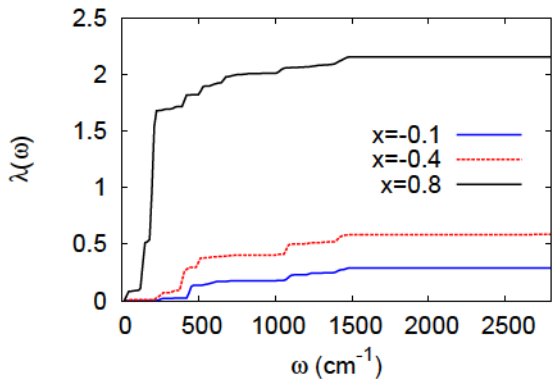

Figure 5.12.: Frequency-dependent electron-phonon interaction $\lambda(\omega)$ in C_8H_2 at two electron doping levels $x = 0.1$ and $x = 0.4$ as well as for hole doping $x = 0.08$. Values were obtained by setting the upper boundary of the integration in Eq. (2.83) to ω, which is equal to setting $n = n'$ in Eq. (2.99). For $\omega \to \infty$, the interaction values are equal to the values of λ entering the Allen-Dynes equation, see Tab. 5.4. The colors are the same as in Fig. 5.11.

$x = -0.1$ and $x = -0.4$, we see that the contribution of the acoustic phonons to the full efective interaction λ is negligible. The main contribution of more than 50% stems from the lower-frequency optical phonons around $500\,\mathrm{cm}^{-1}$. The intermediate-frequency phonons between $1000\,\mathrm{cm}^{-1}$ and $1500\,\mathrm{cm}^{-1}$ also contribute significantly, while the amount of effective interaction from the high-frequency stretching modes is negligible. For hole doping, the situation is similar to $MoSe_2$, cf. Fig. 5.4, since the strong coupling to acoustic phonons around $200\,\mathrm{cm}^{-1}$ amounts to more than 75% of the full effective λ. The contributions of the other phonons at higher frequencies are similar to the case of electron doping.

From the values of the function α^2F we can calculate the parameters of superconductivity via the equations in Sec. 2.6.2. The results for both electron and hole doping are provided in Tab. 5.4. A significant critical temperature of up to 40 K and more is obtained in both cases. This is a rather large value for a conventional electron-phonon superconductor and comparable[7] to the T_c of 39 K found in MgB_2, [213–215]. The reason for this large critical temperature is the coupling to high-frequency optical phonon modes. For the TMDCs we obtained comparable values for the effective electron-phonon coupling $\lambda \sim 1$

[7]The situation in MgB_2 is more complex due to the multi-gap nature of the superconducting phase, which is beyond the scope of the isotropic Eliashberg or Allen-Dynes approach used here. If one wanted to describe the critical temperature of about 40 K in MgB_2 within the latter approach anyway, an effective interaction of $\lambda = 1.01$, a frequency of $\omega_{\log} = 453\,\mathrm{cm}^{-1}$, and a value of $\mu^* = 0.1$ would be reasonable according to Ref. [213].

Table 5.4.: Parameters for the superconducting phase in doped C_8H_2, calculated by DFPT (see Sec. 2.5.2) and Eliashberg theory (see Sec. 2.6.2). Negative values for the doping x represent electron doping, while positive represent hole doping. A value of $\mu^* = 0.15$ is used for all critical temperatures.

Doping x	coupling λ	$\omega_{\log}$ (cm^{-1})	T_c (K)
-0.1	0.29	930	0.1
-0.2	0.48	865	3.5
-0.4	0.57	773	7.7
-1.0	1.48	535	51.4
0.1	0.51	685	3.6
0.2	0.60	577	6.8
0.3	0.87	504	20.0
0.4	1.48	488	34.7
0.8	2.15	320	43.2

(see Tab. 5.1), but these values resulted in considerably lower critical temperatures (see Tab. 5.3) due to the coupling to low-frequency acoustic phonons. For the case of C_8H_2 discussed here, already a lower λ leads to a larger critical temperature because of the large values for $\omega_{\log}$. Especially in the case of hole doping, where we have a rather large $T_c \gtrsim 20\,\mathrm{K}$ already at doping levels $x \gtrsim 0.3$, another reason is the strong coupling which results from the high electronic DOS since the Fermi level is close to the maximum at the M point (see Fig. 3.16). Much larger electron-doping levels of up to $x \sim 1.0$ are needed to get an effective coupling of similar strength.

In both doping regimes, a Lifshitz transition to a larger number of Fermi pockets takes place at $x \sim -0.2$ and $x \sim 0.9$, respectively (see Figs. 3.15 and 3.16). These two transitions have different effects on the superconducting phase. At the critical electron doping, we see a significant enhancement of λ which leads to a rise in the critical temperature. For hole doping levels $x \gtrsim 0.9$, the coupling to acoustic, instable phonons leads to non-zero values of α^2F at negative, i.e., imaginary frequencies. In this case, the use of Eliashberg theory in the simple Allen-Dynes form is no longer valid and we are, thus, not able to calculate superconducting parameters for hole-doping levels beyond $x = 0.8$. Furthermore, we see that the atomic structure of C_8H_2 used in this thesis is not stable beyond hole doping levels of $x \gtrsim 0.9$.

As a last point, we need to mention that the validity of some of the results presented here can be questioned. In [155], the C_8H_2-structure that we use for all our calculations was found to be stable only up to a critical doping of $x = 0.05$ additional electrons per carbon atom which corresponds to a doping level of $x = \pm 0.4$ per unit cell as discussed here.

Assuming the phase diagram to be symmetric, this means that the crystal structure of C_8H_2 might be different from the one in Fig. 3.13 for $|x| > 0.4$ which would certainly change the parameters of the superconducting phase.

To conclude, superconductivity in C_8H_2 was investigated here for the first time. We have seen that critical temperatures of 40 K and more can be achieved in electron as well as hole-doped C_8H_2. The high values for T_c result from a strong coupling of the electrons to acoustic (hole doping) and optical (electron doping) phonons with high frequencies due to the low atomic masses of hydrogen and carbon.

5.3. Unconventional superconductivity in MoS_2

By unconventional superconductivity we mean that the effective electron-electron interaction which leads to the formation of Cooper pairs and is responsible for the superconducting phase is not mediated by electron-phonon interaction, but rather by some other mechanism such as charge or spin fluctuations. Since the experimental observation of high-temperature superconductivity in the cuprates [97], a lot of such mechanisms have been discussed [99]. Most of them share that their pairing is of pure electronic nature and that the order parameter, i.e., the gap function, has a lower symmetry than the s-wave of conventional electron-phonon superconductors.

In this section, we investigate possible unconventional superconductivity that arises when the Fermi surface consists of multiple distinct sheets, and where the pairing is purely mediated by the otherwise repulsive Coulomb interaction between the electrons. This Fermi surface is realized in the electron doped semiconducting TMDCs, see Fig. 3.7. We first write down the relevant equations starting from anisotropic BCS-theory (see Sec. 2.6.1) and then discuss the example of MoS_2 as a typical semiconducting TMDC. Most of this section was already published by the author in Ref. [159].

5.3.1. BCS equations in the multi-valley case

To get an effective mean-field description that can be used for the discussion of unconventional Coulomb-driven superconductivity, we use the anisotropic BCS equations, see Eq. (2.86) and Ref. [216],

$$\Delta_k = -\frac{1}{N}\sum_{k'} V(k,k')\frac{\Delta_{k'}}{2E(\varepsilon_{k'})}\tanh\frac{\beta E(\varepsilon_{k'})}{2}, \tag{5.4}$$

where Δ_k is the anistropic gap, N is the number of unit cells, $V(k,k')$ is the coupling of momenta k and k', $E(\varepsilon_k) = \sqrt{\varepsilon_k^2 + \Delta_k^2}$ is the energy, and β is the inverse temperature. If the Fermi surface can be divided into different valleys FS_i (as it is the case in the doped semiconducting TMDCs, cf. Fig. 3.7) and if the energy gap Δ is constant in each valley and does not depend on the wave vector k, we can simplify the description of the gap to

$$\Delta_k = \Delta_i \quad \text{if } k \in \mathrm{FS}_i. \tag{5.5}$$

In this way, the summation over k' in Eq. (5.4) can be decomposed into a summation over Fermi suface sheets and a summation over all momenta k' on the relevant Fermi surface sheet. If we further rewrite the summation over k' into an energy integration and introduce the partial DOS per valley

$$N_i = \frac{1}{N}\sum_{k\in\mathrm{FS}_i}\delta(\varepsilon_{k'} - \varepsilon), \tag{5.6}$$

we arrive at the expression

$$\Delta_i = -\sum_j V_{ij}\Delta_j N_j 2\int_0^{E_\mathrm{cut}} \mathrm{d}\varepsilon \frac{1}{2E(\varepsilon)}\tanh\frac{\beta E(\varepsilon)}{2}, \tag{5.7}$$

where we assume a constant coupling V_{ij} inside as well as between the valleys and an energy cutoff E_cut.

Close to the critical temperature, the gap is $\Delta \approx 0$ which leads to $E(\varepsilon) \approx \varepsilon$, and we can rewrite the integration to

$$\int_0^{\beta E_\mathrm{cut}/2} \mathrm{d}x \frac{\tanh x}{x} \equiv F(\beta E_\mathrm{cut}/2) \tag{5.8}$$

with the function $F(x)$ and $x = \beta\varepsilon/2$. The function $F(x)$ can be evaluated numerically

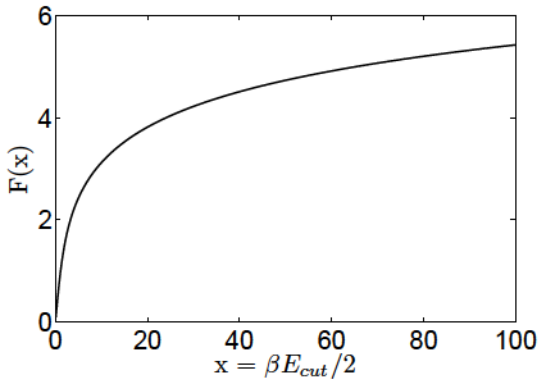

Figure 5.13.: Function $F(x)$ as defined in Eq. (5.8) and used from Eq. (5.9) onwards.

and has positive finite values for all x, see Fig. 5.13. These approximations lead to the expression of the gap

$$\Delta_i = -\sum_j V_{ij}\Delta_j N_j F\left(\frac{\beta E_{\text{cut}}}{2}\right). \tag{5.9}$$

We define a dimensionless valley-valley coupling constant

$$\mu_{ij} = \frac{1}{N(E_{\text{F}})} V_{ij} N_i N_j, \tag{5.10}$$

where $N(E_{\text{F}})$ is the total density of states per spin and the full coupling matrix is given by $(\boldsymbol{\mu})_{ij} = \mu_{ij}$, similar to Eq. (5.1). Note that the above definition of μ_{ij} can be regarded as an anisotropic extension to the result for the averaged Coulomb repulsion μ in the case of purely local coupling, see Eq. (2.101). Using this terminology, Eq. (5.9) becomes

$$\Delta_i = -\sum_j \frac{N(E_{\text{F}})}{N_i} \mu_{ij} F\left(\frac{\beta E_{\text{cut}}}{2}\right) \Delta_j. \tag{5.11}$$

This can be cast into a matrix form via

$$0 = \left(\mathbf{N} + N(E_{\text{F}})\, F\, \boldsymbol{\mu}\right) \boldsymbol{\Delta}, \tag{5.12}$$

where $\mathbf{N}$ is the diagonal matrix containing the density of states per valley and $\boldsymbol{\Delta}$ is a vector of the gaps in each valley.

A non-trivial solution to Eq. (5.12) exists if

$$\det\left[\mathbf{N} + N(E_{\text{F}})\, F\, \boldsymbol{\mu}\right] = 0. \tag{5.13}$$

Otherwise, $[\mathbf{N} + N(E_\mathrm{F})\, F\, \boldsymbol{\mu}]$ would be invertible and Eq. (5.12) could be fulfilled via the trivial case $\boldsymbol{\Delta} = 0$. Since $N(E_\mathrm{F})$ and F are always positive, Eq. (5.13) has no solution if all eigenvalues of $\mathbf{N}$ and $\boldsymbol{\mu}$ are positive. Furthermore, since $\mathbf{N}$ has only positive entries and is diagonal, it can have only positive eigenvalues which means that the necessary criterion is that at least one eigenvalue of $\boldsymbol{\mu}$ is negative. A sufficient criterion for a non-trivial solution and, thus, a superconducting instability with a non-vanishing gap $\boldsymbol{\Delta}$ is a negative eigenvalue of $\mathbf{N}^{-1/2}\boldsymbol{\mu}\mathbf{N}^{-1/2}$. This can be seen by multiplying Eq. (5.12) with $\mathbf{N}^{-1/2}$ from left and right and by looking at the characteristic polynomial of the resulting condition, $\det\left[\mathbf{N}^{-1/2}\boldsymbol{\mu}\mathbf{N}^{-1/2} + 1/\{N(E_\mathrm{F})\, F\}\, \mathbb{1}\right] = 0$.

If $\boldsymbol{\mu}$ is a 2×2-matrix with only positive, i.e., repulsive entries as it is the case in our calculations in the range of low electron doping [cf. Eq. (5.1)], it has a negative eigenvalue once the off-diagonal element is larger than the diagonal elements, which means in our case that the coupling between the two valleys, μ_inter, is larger than the coupling inside of one valley, μ_intra. This scenario was originally proposed for MoS_2 in the range of low doping in Ref. [217]. If the Fermi surface consists of more than two valleys, as it is the case for MoS_2 under high electron doping where the Fermi surface has six additional pockets and $\boldsymbol{\mu}$ is an 8×8-matrix, there are various μ_inter and μ_intra, and it is more insightful to directly discuss the eigenvalues of the $\boldsymbol{\mu}$-matrix.

5.3.2. Results of matrix calculations

In general, superconductivity occurs when the total coupling between the electrons is attractive, $\mu_\mathrm{tot} < 0$. For conventional phonon-mediated superconductivity, as it was discussed in Secs. 5.1 and 5.2, this is the case when the effective coupling between electrons mediated by the phonons overcomes the electron-electron repulsion. As we showed in the previous section, a superconducting instability is also possible for a purely repulsive Coulomb interaction if at least one eigenvalue of the coupling matrix $\boldsymbol{\mu}$ is negative. We now investigate whether this type of superconducting order is possible in electron doped MoS_2 and the semiconducting TMDCs in general.

At low doping levels, i.e., when only two Fermi surface sheets around the two K points exist in the semiconducting TMDCs (see Fig. 3.7), $\mu_\mathrm{inter} > \mu_\mathrm{intra}$ would lead to a negative eigenvalue of μ and, thus, to a superconducting phase. This phase would be purely electronically mediated with an unconventional sign-changing order parameter ($\Delta_\mathrm{K} = -\Delta_\mathrm{K'}$) as discussed in Ref. [217]. However, as one can see from Fig. 5.6 and Fig. 5.14, the intravalley coupling is always larger than the intervalley coupling

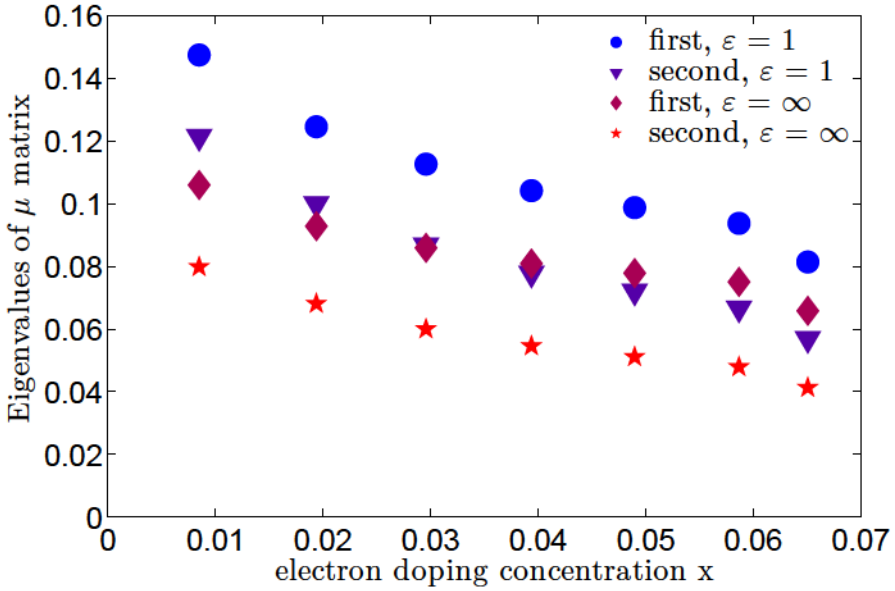

Figure 5.14.: Dependence of the 2×2-matrix $\boldsymbol{\mu}$ [cf. Eq. (5.1)] on the electron doping concentration x in the case of low doping. We present the eigenvalues for vacuum ($\varepsilon = 1$) and metallic ($\varepsilon = \infty$) surrounding.

and $\boldsymbol{\mu}$ has only positive eigenvalues. This means that the described situation is not realized in freestanding MoS_2. Furthermore, it cannot be achieved using substrates or capping layers with arbitrarily large (q independent) dielectric constants. Although the additional screening by the dielectric environment can lower the intravalley coupling constant by up to 30 %, see Fig. 5.6, it is not strong enough to achieve $\mu_{\text{inter}} > \mu_{\text{intra}}$.

In the high-doping regime, we do not find any negative eigenvalues, either (see Fig. 5.15). Furthermore, there is no significant difference in the values for freestanding MoS_2 and MoS_2 in a perfectly metallic dielectric environment, here. This insensitivity to the dielectric environment upon high doping was already oberserved for the full averaged Coulomb coupling constant μ (see Fig. 5.5). Thus, Coulomb-driven superconductivity is not possible in MoS_2 below and above the Lifschitz transition involving the mechanism of several Fermi pockets discussed here. Since both the electronic structure and the averaged Coulomb coupling are very similar for the other semiconducting TMDCs, see Figs. 3.6 and 5.7, we can expand this conclusion to all four materials investigated here. All in all, we conclude that for unconventional electron-driven superconductivity in doped MoS_2 or other semiconducting TMDCs one would need more complex mechanisms involving a stronger renormalization of the interactions at low energies than what can be achieved via substrates [218].

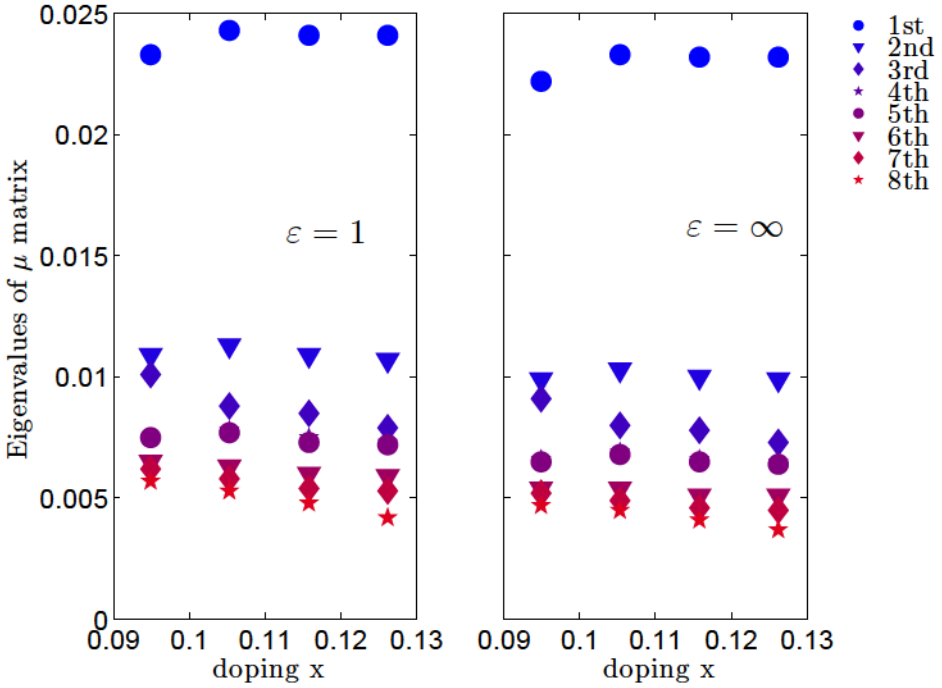

Figure 5.15.: Dependence of the 8×8-matrix $\boldsymbol{\mu}$ on the electron doping concentration x in the case of high doping. The eigenvalues with background dielectric constant $\varepsilon = 1$ (left) and $\varepsilon = \infty$ (right) are shown.

5.4. Charge and spin order in TMDCs

Charge order has been a popular research topic in the TMDCs in recent years. Especially the *typical* Charge Density Wave (CDW) material $NbSe_2$ has received a lot of attention [16, 23, 194, 219–223] but other metallic TMDCs and their CDW phases have also been studied, e.g. TaS_2 [19, 24] and $TaSe_2$ [224].

One original theoretical description of charge order that is often referred to was performed by Peierls who showed that a one-dimensional metallic chain is not stable at low temperatures [225]. Rather, the underlying atomic lattice gets distorted which leads to a charge modulation called charge density wave with the wave vector $q = 2k_F$. A band gap opens up and the material becomes insulating. Since the work by Peierls, a lot of theoretical and experimental effort has been put into the investigation of CDWs; they have been found in materials with higher dimension, and more sophisticated descriptions have been developed [226].

Besides the Peierls mechanism and related mechanisms, where charge order arises due to the interplay of atoms, electrons and phonons, charge order can also arise due to strong

Coulomb repulsion which pins the electrons to the atomic sites. These mechanisms are qualitatively different since in a half-filled band described by a Hubbard-Holstein Hamiltonian, cf. Eq. 2.16, large electron-phonon coupling may lead to a bipolaronic insulator while large electron-electron coupling may lead to Mott insulating states, see Ref. [49].

A similar phenomenon is the magnetic ordering of the electronic spins that can lead to Spin Density Waves (SDWs), ferromagnetism, and other magnetic phenomena. For the TMDCs and related materials, magnetic ordering was previously observed in theoretical results for vanadium based compounds [227, 228], while ferromagnetic ordering upon strain was predicted to occur in niobium compounds [229]. Furthermore, the possibility of SDWs in NbS_2 was discussed [184].

In this section, we discuss charge order in the form of CDWs which means that we look at instabilities in the phononic dispersion, see Sec. 5.4.1, as well as in the charge susceptibility, see Sec. 5.4.2. These instabilities signal a tendency of the system towards a periodic modulation of the lattice positions and, accordingly, of the electronic charge density. Additionally, we look at the possibility of spin order signaled by an enhancement of the magnetic susceptibility, see Sec. 5.4.3. In all subsections, we focus on the example of NbS_2 since it turns out that this material is on the brink between spin and charge order and is, thus, an especially interesting case.

5.4.1. Lattice instability and charge density wave

For the metallic TMDCs NbS_2 and $NbSe_2$, our calculations of the phonon dispersion using DFPT predict an instability at a point below the M point in reciprocal space, see Figs. 5.2 and B.3, respectively. In both cases, the minimum of the softened phonon frequency is at $q_{\mathrm{CDW}} \approx 2/3\,\overline{\Gamma\mathrm{M}}$ which indicates a threefold symmetry of the CDW phase, i.e., that the phase is commensurate with a 3×3-supercell. This is indeed the wave vector at which the CDW instability occurs in bulk and probably monolayer 2H-$NbSe_2$ [16], which shows that DFT and DFPT calculations can already be sufficient to describe charge ordering. On the other hand, no anharmonic effects are included here, and, thus, the suppression of the CDW phase that is observed in bulk 2H-NbS_2 [195] cannot be reproduced by our calculations. Whether monolayer NbS_2 exhibits a CDW phase has not been investigated experimentally, as far as we know, so our result that a CDW exists in this system cannot be verified.

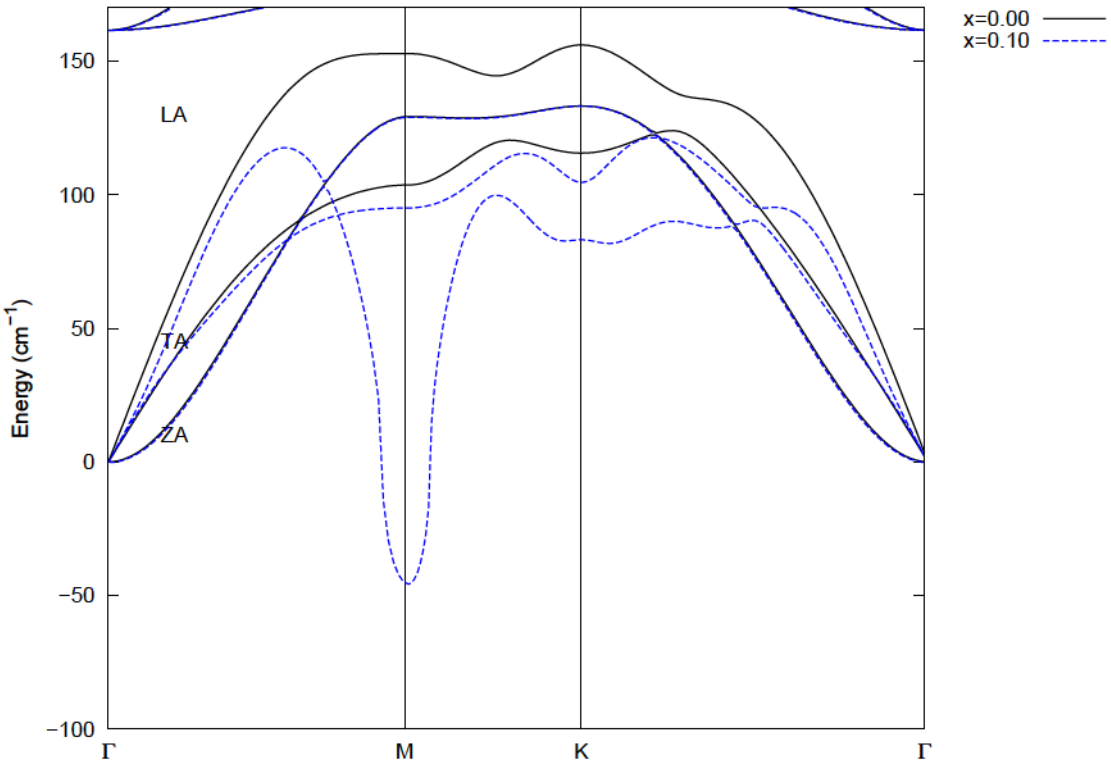

Figure 5.16.: Phononic dispersion in electron doped $MoSe_2$ showing possible CDW instability.

In addition to the at least partially correct description of the CDW in the metallic TMDCs, our calculations predict the occurence of a CDW for the semiconductors upon high electron doping. Using again the example of $MoSe_2$, we show in Fig. 5.16 that the strong softening of the LA acoustic mode leads to an instability at the M point, meaning that the resulting CDW phase is commensurate with a 2×2-supercell. Similar results were obtained for MoS_2 in Ref. [193], and we also find the instability at M for WS_2 and WSe_2. This result can be very interesting since it means that not only the superconducting phase, but also the CDW phase in semiconducting TMDCs can be tuned externally via the electron doping level, see Fig. 5.10. As already mentioned in Sec. 5.1.4, we do not know of any study that has looked for a CDW in the high-doping regime of monolayer semiconducting TMDCs. Thus, it remains unclear whether the CDW instability found here is only a theoretical prediction or also a real effect found in experiments. As indicated in Fig. 5.10, the onset of the CDW phase can be shifted towards lower electron doping concentrations by the use of heavier atoms due to the lowered phonon frequencies. This leads us to the prediction that the CDW phase will be most easily realizable in experiments on WSe_2 (see also Tab. 5.3).

5.4.2. Instability in the charge susceptibility

In addition to looking at the atomic properties of a material, i.e., the phononic dispersion in our case, and implying that a CDW goes hand in hand with a lattice instability, indications of a CDW can also be found by looking at the electronic charge susceptibility. An enhancement and a divergence or eventually a sign change around some wave vector q_{crit} in this quantity can be interpreted as an instability towards the formation of a charge ordered phase with wave vector q_{crit}, which would result in an increased double occupancy and eventually lead to an insulating state [49]. By performing model calculations for the charge susceptibility, we can gain insight into the formation of charge order beyond the rather superficial interpretation of phonon dispersions obtained from DFPT. Employing again the RPA approximation and the matrix formalism for the electronic orbitals, as already done for the plasmonic spectra in Sec. 4.4, the charge susceptibility or charge response function can be calculated using a Dyson equation via

$$\chi_{\text{ch}} = -\Pi \cdot (\mathbb{1} - \mathbf{V}^* \Pi)^{-1} \tag{5.14}$$

where $\Pi = \Pi_0(\boldsymbol{q}, \omega)$ is the polarization obtained from RPA calculations, see Eq. (2.53), and where we include a model electron-phonon coupling $\lambda(\omega)$ in addition to the interband and background screened interaction $\mathbf{V}$ [see Eq. (4.6)]

$$\mathbf{V}^* = \mathbf{V} - \lambda(\omega) \begin{pmatrix} 1 & 1 & 1 \\ 1 & 1 & 1 \\ 1 & 1 & 1 \end{pmatrix}. \tag{5.15}$$

In the static limit, the model electron-phonon coupling is equal to the coupling in the Hubbard-Holstein model, i.e., $\lambda = 2g^2/\omega_0$, and we use $\lambda = 1.55\,\text{eV}$. Away from $\omega = 0$, the model electron-phonon interaction is frequency-dependent with

$$\lambda(\omega) = g^2 D_0(\omega) = 2g^2 \frac{\omega_0}{\omega^2 - \omega_0^2} \tag{5.16}$$

with the non-interacting phonon Green's function D_0 [see Eq. (2.24)]. We use an electron-phonon coupling of $g = 0.1245\,\text{eV}$ and a phonon frequency[8] of $\omega_0 = 20\,\text{meV}$, which lead to $\lambda = 1.55\,\text{eV}$ in the static limit. The matrix of ones in Eq. (5.15) means that we assume an effective electron-phonon coupling that is the same for the three relevant

[8] Values around $150\,\text{cm}^{-1} \sim 20\,\text{meV}$ are typical for the short-wavelength acoustic phonons of NbS_2 and other TMDCs, cf. Fig. 5.2.

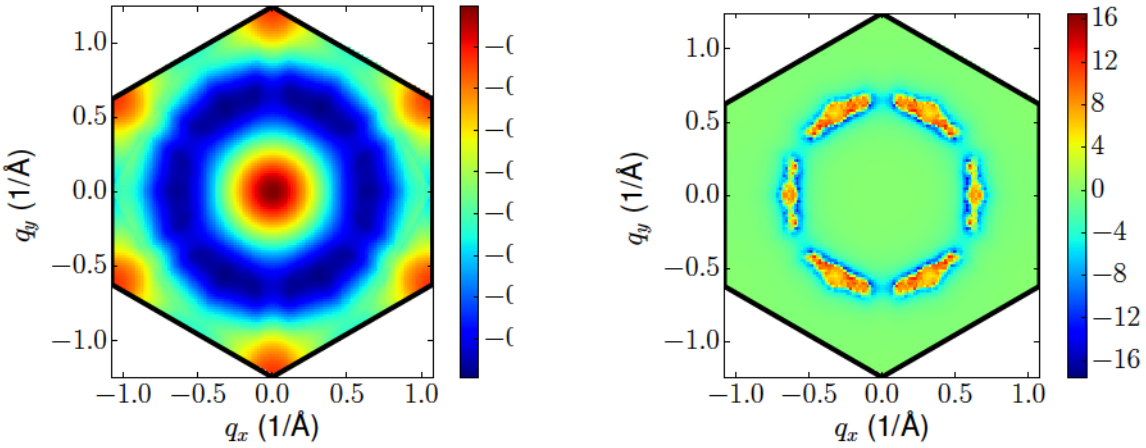

Figure 5.17.: Real part of the static macroscopic charge susceptibility $\chi_{\mathrm{ch}}(\mathbf{q}, \omega = 0)$ in free-standing monolayer NbS_2 as calculated via Eq. (5.14). We show the values of χ for a Coulomb interaction $\mathbf{V}^*$ without electron-phonon coupling as described in Eq. (5.15) (Left) and the values with static model electron-phonon coupling $\lambda = 1.55$ (Right). The black lines correspond to the boundaries of the first Brillouin zone.

electronic orbitals. This is basically comparable to the use of an effective electron-phonon interaction in the Allen-Dynes approximation to the Eliashberg theory of superconductivity, see Eq. (2.83).

In Fig. 5.17 we show the results for the macroscopic value [see Eq. (4.4)] of $\chi_{\mathrm{ch}}(\boldsymbol{q}, \omega = 0)$ for $\lambda = 0$ and $\lambda = 1.55$. If we remind ourselves that the static non-interacting susceptibility, which is just the RPA polarization $\Pi_0(q \to 0, \omega = 0)$, has limiting values of[9] $1/3 \cdot N(E_{\mathrm{F}}) \sim 1/3 \cdot 2.8\,\mathrm{eV}^{-1} \sim 1\,\mathrm{eV}^{-1}$, see Eq. (2.58) and Tab. 5.2, we can directly conclude that the Coulomb interaction reduces the charge susceptibility quite strongly by a factor of ~ 10 or more if no electron-phonon interaction is present. On the other hand, one can see that the additional electron-phonon coupling leads a strong enhancement of the static susceptibility and to a sign-changing instability around $q_{\mathrm{crit}} = 0.6\,\overline{\Gamma\mathrm{M}}$. This indicates that large enough electron-phonon coupling can trigger the formation of a CDW in NbS_2. The critical value of the wave vector is similar to the observed CDW vector of $2/3\,\overline{\Gamma\mathrm{M}}$ that was discussed in Sec. 5.4.1 which shows that the tendency towards charge order in the metallic TMDCs can already be understood on a RPA level.

Figs. 5.18 and 5.19 show the results for the dynamic susceptibility $\chi_{\mathrm{ch}}(\boldsymbol{q}, \omega)$ along the

[9] The factor of 1/3 results from the use of the macroscopic value of the susceptibility and the polarization, cf. Eq. (4.4). A simple sum of all matrix elemts of the 3×3 polarization matrix would yield the full DOS at the Fermi level in the static long-wavelength limit.

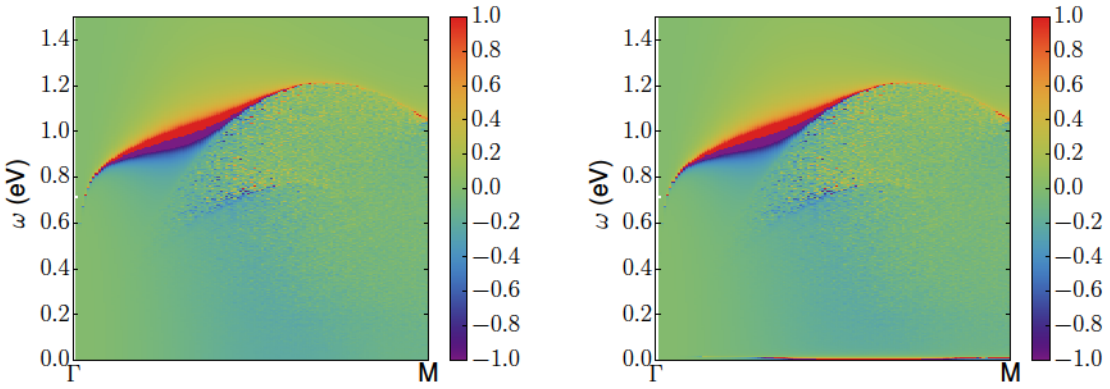

Figure 5.18.: Real part of the macroscopic charge susceptibility $\chi_{\mathrm{ch}}(\mathbf{q},\omega)$ in freestanding monolayer NbS_2 as calculated via Eq. (5.14) for the path from Γ to M in reciprocal space (cf. Fig. 3.3). We show the values of χ for a Coulomb interaction $\mathbf{V}^*$ without electron-phonon coupling as described in Eq. (5.15) (Left) and the values with model electron-phonon coupling $g = 0.1245\,\mathrm{eV}$ and phonon

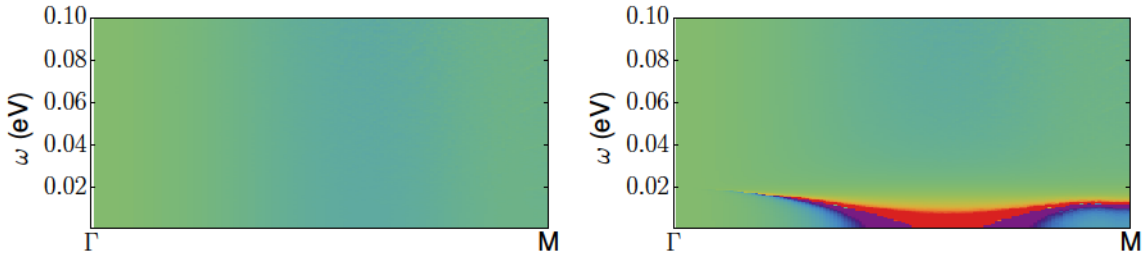

Figure 5.19.: Same as Fig. 5.18 for small frequencies ω.

path from Γ to M. The instability around q_{crit} upon increased electron-phonon interaction is only present for very small frequencies below the phonon frequency $\omega_0 = 20\,\mathrm{meV}$; at higher frequencies, there is no visible difference between the values of the susceptibility with and without electron-phonon coupling. This shows that the coupling to phonons is only relevant in a small energy range, at least in the case of acoustic phonons. Overall, the susceptibility without electron-phonon coupling has similar features to the EELS spectrum of NbS_2, see Fig. 4.11. It shows a sign-changing transition from a minimum to a maximum at frequencies of around 1 eV for wave vectors below $0.5\,\overline{\Gamma\mathrm{M}}$ which is similar to the plasmonic dispersion.

5.4.3. Instability in the spin channel

So far, possible magnetic ordering in NbS_2 was studied in Ref. [184]. There, a single-band model without orbital characters [cf. Eq. (2.53)] and without Coulomb interaction was used. The authors found possible SDW instabilities at a wave vector $q_{\text{crit}} = 0.4\,\overline{\Gamma\text{M}}$.

We make use of the magnetic response function [see Eq. (2.17)] or magnetic susceptibility

$$R^{ij} = \frac{\delta\langle\hat{\sigma}_i\rangle}{\delta B_j} \tag{5.17}$$

which describes the change of the spin density $\langle\hat{\sigma}\rangle$ due to a change in the applied magnetic field B with $i, j \in [x, y, z, -, +]$. The $+$ and $-$ correspond to the raising and lowering of spins, i.e., the ladder operators $\hat{\sigma}_+ = \hat{\sigma}_x + i\hat{\sigma}_y$ and $\hat{\sigma}_- = \hat{\sigma}_x - i\hat{\sigma}_y$. The Pauli matrices $\sigma_x, \sigma_y, \sigma_z$ are given in Eq. (2.93).

To calculate the magnetic susceptibility, we use the formalism described in Ref. [230] which means that the T-matrix approximation as well as the GW approximation (see Sec. 2.4) are employed. The relevant quantity for our considerations is the spin susceptibility which is the transverse magnetic susceptbility $R^{-+}(\boldsymbol{q}, \omega)$. In our case, the equations from Ref. [230] yield for the interacting susceptibility

$$\chi_{\text{sp}}(\boldsymbol{q}, \omega) = R^{-+}(\boldsymbol{q}, \omega) = -\sum_{mn}\sum_{\alpha\beta} \sigma^{-}_{\beta\alpha}\sigma^{+}_{\alpha\beta}\left[K^{\alpha\beta}_{mn,nm}(\boldsymbol{q}, \omega) + L^{\alpha\beta}_{mn,nm}(\boldsymbol{q}, \omega)\right] \tag{5.18}$$

with spin indices α, β and orbital indices m, n which are again given by $\{d_{z^2}, d_{xy}, d_{x^2-y^2}\}$. Since we do not take spin-orbit coupling into account and have a spin-degenerate band structure and Coulomb interaction, the kernels K and L do not depend on the spin indices and the summation over Pauli matrices in Eq. (5.18) yields

$$\sum_{\alpha\beta} \sigma^{-}_{\beta\alpha}\sigma^{+}_{\alpha\beta} = 4. \tag{5.19}$$

The kernel K is given by

$K_{kl,mn}(\boldsymbol{k}, \boldsymbol{q}, i\omega) =$ 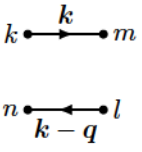

(5.20)

which is equal to an open RPA *bubble* and, thus, the negative of the RPA polarizability from Eq. (2.53), which in turn means that the non-interacting susceptibility is related

to the polarizability via

$$R^{-+}_{\text{Non-Int}}(\boldsymbol{q},\omega) = \frac{4}{2}\,\Pi_0(\boldsymbol{q},\omega) \tag{5.21}$$

where the factor 4 comes from the summation over Pauli matrices as mentioned above and the 2 results from the fact that the RPA polarizability that we used in the previous chapters was calculated without spin-orbit coupling and, thus, all included bands were two-fold spin-degenerate.

To calculate the Kernel L, which is defined by

$L_{km,ln} =$ 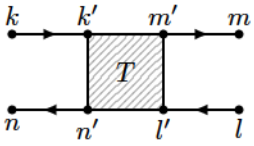

(5.22)

we need the so-called T-matrix which incorporates all interaction effects. The elements of this matrix follow the Bethe-Salpeter equation

$$T_{kl,mn}(\boldsymbol{q},\omega) = W_{kl,mn} + \sum_{k'l',m'n'} W_{kk',n'n} K_{k'l',m'n'}(\boldsymbol{q},\omega) T_{k'l,mn'}(\boldsymbol{q},\omega) \tag{5.23}$$

where the Coulomb interaction W is the fully screened local interaction as given in Tabs. B.8 and B.11. Adopting a generalized index notation of a product basis with $\tilde{k} = \{k, n\}$ and $\tilde{m} = \{l, m\}$, we can rewrite the above equation using a matrix formalism

$$\mathbf{T} = \mathbf{W} + \mathbf{W} \cdot \mathbf{K} \cdot \mathbf{T}. \tag{5.24}$$

From this equation, similar to a Dyson equation, we can obtain the T-matrix directly via

$$\mathbf{T} = (\mathbb{1} - \mathbf{W} \cdot \mathbf{K})^{-1} \cdot \mathbf{W}. \tag{5.25}$$

The kernel L is then calculated via

$$\mathbf{L} = \mathbf{K} \cdot \mathbf{T} \cdot \mathbf{K}. \tag{5.26}$$

Our results for the static spin susceptibility are given in Fig. 5.20. We find the same critical wave vector $q_c = 0.4\,\overline{\Gamma\mathrm{M}}$ as [184] for the non-interacting susceptibility, but the susceptibility is suppressed for large wave vectors due to the inclusion of orbital characters and the resulting overlap matrix elements in our model. Furthermore, we see a strong enhancement in the interacting susceptibility due to the fully screened onsite

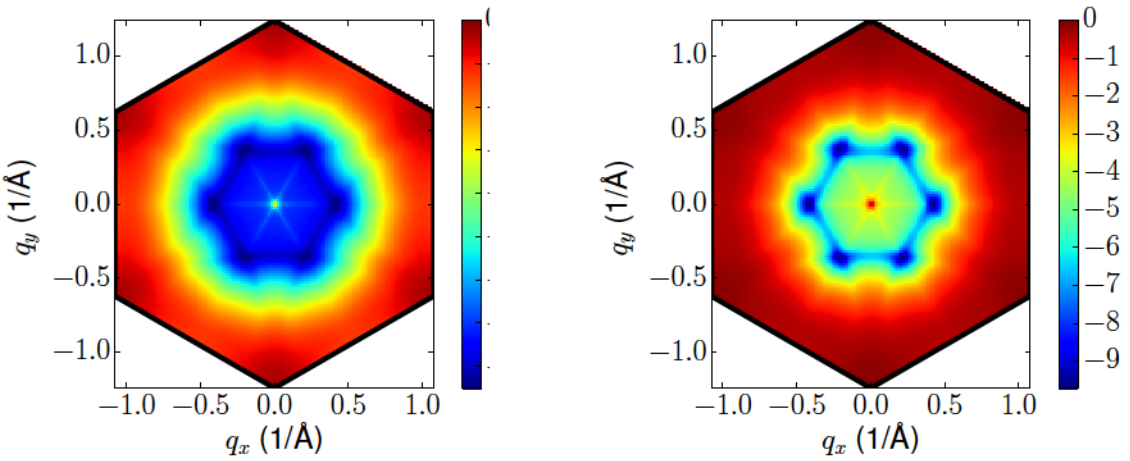

Figure 5.20.: (Left) Non-interacting static spin susceptibility $R^{-+}_{\mathrm{Non-Int}}(\boldsymbol{q}, \omega = 0)$ for NbS_2. (Right) Interacting static spin susceptibility $R^{-+}(\boldsymbol{q}, \omega = 0)$ for NbS_2. Both quantities were calculated using Eq. (5.18), where we set $L = 0$ for the non-interacting susceptibility[11]. The black lines correspond to the boundaries of the first Brillouin zone.

interaction as given in Tabs. B.8 and B.11; the enhancement leads to a difference of up to an order of magnitude compared to the non-interacting susceptibility. This change upon the inclusion of interaction effects is a clear indication that $q_c = 0.4\,\overline{\Gamma\mathrm{M}}$ can indeed be a critical[10] point for magnetic ordering in NbS_2. The enhancement is usually called a Stoner enhancement, since for the single-band and single-orbital case where Π and W are scalars, we can calculate the magnetic susceptibility in the long-wavelength limit via

$$R = \frac{\Pi}{1 - \overline{W}\Pi} \tag{5.27}$$

with the DOS at the Fermi level $N(E_\mathrm{F}) = \Pi(q \to 0, \omega = 0)$ and the onsite interaction $\overline{W}$. From Eq. (5.27), we can directly see the Stoner criterion which states that a magnetic instability is to be expected for $N(E_\mathrm{F})\overline{W} > 1$.

Whether spin and/or charge order are indeed realized in monolayer NbS_2 is beyond the scope of the RPA approach presented here. To decide this question, one needs theories that include the correlation of both electron-electron and electron-phonon interaction, such as the Dual Boson method [90, 91]. However, our results clearly show that NbS_2

[10] We call this point *critical* although the spin susceptibility is only strongly enhanced and does not diverge here.

[11] One might expect the non-interacting susceptibility to be equal to twice the DOS at the Fermi level in the long-wavelength limit due to Eq. (5.21). This is only true here if one considers a scaling factor of 1/3 which arises due to the use of the macroscopic values as shown in Eq. (4.4).

is an intermediate interesting case since it exhibits characteristica of the transitions to both phases. This means that it might be possible to experimentally tune the order in NbS_2 via substrates or other external parameters.

6. Conclusions

Although many fundamental properties of 2D materials have been investigated in the last couple of years, a lot of open questions remain in the research on this new material class. One topic that has not received enough attention and is not yet fully understood is the Coulomb interaction, along with its influences on the (many-body) properties of 2D materials and its interplay with other interactions such as the electron-phonon interaction. While it is known that the Coulomb interaction can be very strong in low dimensions due to reduced environmental screening, the details and effects of the interaction in specific situations are often unclear.

In this thesis, we performed a detailed investigation of the Coulomb interaction, alongside with calculations for the properties of the phonons, and with a focus on the six transition metal dichalcogenides (TMDCs) MX_2 with $M = \mathrm{Mo}, \mathrm{W}, \mathrm{Nb}$ and $X = \mathrm{S}, \mathrm{Se}$. We build up a material database containing both electronic and phononic properties, the electron-electron interaction, the electron-phonon interaction, and resulting phases. To this end, we made use of Density Functional Theory and Density Functional Perturbation Theory as implemented in the software package Quantum Espresso, as well as (c)RPA calculations employing the Spex and Fleur codes and our own RPA code.

As a first result, we obtained a simple, yet accurate and material-specific model for the band structure and the Coulomb interaction in 2D semiconducting and metallic TMDCs. We studied the Coulomb interaction and the screening and found that they can have a profound influence on many-body instabilities. Furthermore, 2D materials show a strong tunability, which was investigated here systematically concerning the use of doping and dielectric substrates. We saw that there are many similarities in the behavior of the different semiconducting or metallic TMDCs, respectively.

In more detail, we found at our level of theory that the plasmon dispersion quantified by the electron energy loss spectrum depends strongly on the electron doping level and the dielectric environment. The dome-shaped or similarly structured superconducting phase found experimentally in doped semiconducting TMDCs could be reproduced with maximum critical temperatures above 10 K and an onset at some critical electron doping

level. Furthermore, we found that the influence of the Coulomb repulsion on superconductivity goes beyond a simple, doping- and material-independent constant μ^*, which leads to a shift of the onset of the phase. We observed a decrease of the values of μ^* with increased doping, with reasonable values $\mu^* \sim 0.13$ in the high-doping regime.

Beyond conventional superconductivity in the TMDCs, our calculations predict a superconducting phase with high critical temperatures above 40 K in electron or hole-doped functionalized graphene C_8H_2, which was investigated here for the first time concerning its superconducting properties. In contrast to previous theoretical studies, we find that no unconventional superconductivity is possible in the doped semiconducting TMDCs, based on the mechanism of different Fermi pockets and a strong intervalley Coulomb repulsion considered here.

Charge order in form of a Charge Density Wave (CDW) is a frequent topic for the TMDCs, especially in $NbSe_2$. Our investigations yield a CDW for all TMDCs, with $q_{\text{crit}} \approx 0.6\,\overline{\Gamma\text{M}}$ in metals from both DFPT and RPA calculations, which is similar to the ordering observed in experiments and theoretical studies on $NbSe_2$. In all semiconducting TMDCs upon high electron doping, we find charge order with $q_{\text{crit}} \approx \overline{\text{M}}$ from DFPT calculations, which is a prediction not yet investigated by experiments. Furthermore, we find possible magnetic order in the metallic TMDC NbS_2 with a strong Stoner enhancement of the spin susceptibility around $q_{\text{crit}} \approx 0.4\,\overline{\Gamma\text{M}}$. This result is an indication of a competition between charge and spin order in the metallic TMDCs; the strong correlations involved in this process are beyond the RPA approach used here.

All in all, this thesis presents a step forward towards a predictive theory of the phases and interactions of 2D materials and especially TMDCs. We see that the properties of these materials are determined by a complex interplay of different factors, notably the Coulomb interaction, the electron-phonon interaction and the screening. Furthermore, this shows that it is possible to manipulate the properties in a non-invasive way from outside of the monolayer system. The different elements of the material database developed here, especially the simple model for the band structure and the Coulomb interaction, present ingredients that are relevant for the further study of the TMDCs. This includes a variety of subjects such as the excitonic properties, where the results on WS_2 are part of an upcoming publication, or the use of monolayer TMDCs in both vertical and lateral heterostructures, which is for example discussed in Refs. [31, 32].

A. Details of calculations

A.1. TMDCs

A.1.1. Electron-phonon calculations

We have used k-meshes of $64 \times 64 \times 1$ points for the fine electron-phonon coupling calculations involved in the DFPT-code of Quantum Espresso and $32 \times 32 \times 1$ points for the coarse calculations of the electronic and phononic structure. The q-mesh for the phonons was made up of $8 \times 8 \times 1$ points in reciprocal space. Cut-offs were set to 60 Ry for the wave functions and to 500 Ry for the charge density.

In Tab. A.1 we show the pseudopotentials that we used for each material as well as the lattice constants. To get the lattice constants, we minimized the total energy of each system using Quantum Espresso. The pseudopotentials were chosen in such a way that the phonon calculations using DFPT worked and yielded reasonable results and that the band structures from our calculations matched those found in the literature. For example, this means that for $MoSe_2$, we needed to use a GGA potential since calculations involving LDA potentials yielded an indirect band gap in the monolayer, which was not found experimentally [231].

Table A.1.: Pseudopotentials and lattice constants that we used for the calculations of different TMDCs in Quantum Espresso.

Material	Pseudo potential	lattice constant (a_0)
MoS_2	LDA, PW [66], MT [232]	5.90
$MoSe_2$	GGA, PBE [69], MT [232]	6.28
WS_2	GGA, PBE [69], HGH [233]	6.07
WSe_2	GGA, PBE [69], HGH [233]	6.34
NbS_2	LDA, PW [66], MT [232]	6.13
$NbSe_2$	GGA, PBE [69], MT [232]	6.57

A.1.2. RPA and cRPA calculations

We performed (c)RPA calculations in Spex for the six different TMDCs in a semiconducting state at vacuum heights from $\sim 30\,a_0$ to $\sim 60\,a_0$ and extrapolated the results to infinite vacuum height to get the best estimation of the Coulomb interaction of an isolated monolayer. All calculations were done on an $18 \times 18 \times 1$ k-mesh, except for the calculations of MoS_2, where we used a $16 \times 16 \times 1$ k-mesh.

In Tab. A.2, we show the lattice constants for the calculations in Fleur and Spex as well as the Unit cell areas that are used to fit the bare Coulomb interaction according to Eqs. (4.5) and (4.11).

Table A.2.: Lattice constants and unit cell areas that we used for the calculations of different TMDCs in Fleur and Spex.

Material	Unit cell area (Å^2)	lattice constant (Å)
MoS_2	8.758	3.180
$MoSe_2$	9.546	3.320
WS_2	8.818	3.191
WSe_2	9.574	3.325
NbS_2	9.840	3.371
$NbSe_2$	10.612	3.501

Concerning the calculations which employ the three-band model and use our own RPA code, we have to make sure that the resolution of the Fermi surface is fine enough. This is why we use k-meshes of 576×576 points for all line plots of the plasmon dispersions of the TMDCs in a metallic state as presented in Sec. 4.4. For the calculation of the effective Coulomb repulsion μ^* of MoS_2 in Sec. 5.1.3, we have also used our own RPA code and k-meshes of 500×500 points.

A.2. Functionalized graphene

A.2.1. Electron-phonon calculations

We have used a lattice constant of $9.315\,a_0 = 4.93\,$Å for the 2×2 super cell, which is equal to 2.465 Å for a primitive graphene cell and, thus, only slightly larger than the $\sim 2.46\,$Å lattice constant of graphene. The potentials were GGA, PBE [69], MT [232] potentials, similar to the calculation of $MoSe_2$ as described above. We have used a

vaccum height of 12.3 Å. The k-meshes were 16×16×1 for the electron structure and coarse phonon calculation and 32×32×1 for the fine electron-phonon mesh. The q-mesh for the phonon dispersion consisted of 4×4×1 points in reciprocal space. We have checked our procedure by computing the electronic band structure for graphane and comparing to the literature in [207].

B. Phononic and Coulomb properties of various TMDCs

In this appendix, we present the data for our fits of the density-density Coulomb interaction and the phonon dispersion for the TMDCs considered in this thesis, as long as they were not shown elsewhere already. Additionally, we show data for the exchange interaction in RPA.

B.1. MoS_2

- The phonon and electron-phonon calculations for MoS_2 that we use in this thesis were previously described in [73, 113, 193].
- Parts of the data for the Coulomb interaction were already published in [159].

Table B.1.: Parameters of Coulomb interaction in MoS_2.

bare U	
leading EV, quadratic	
γ (Å)	2.091
leading EV, cubic	
γ (Å)	1.932
δ (Å^2)	0.395
microscopic EV	
U_2 (eV)	0.810
U_3 (eV)	0.367

dielectric ε	
leading EV, simple	
ε_∞	9.253
d (Å)	9.136
leading EV, pseudo-Resta	
a (1/Å^2)	2.383
b	17.836
c (Å)	5.107
d (Å)	2.740
e	5.739
microscopic EV	
ε_2	3.077
ε_3	2.509

Table B.2.: Bare onsite U as well as background screened onsite V and fully screened onsite Coulomb matrix elements W for the three important orbitals in real space. Values for W are in the range of low electron doping $x \approx 0.04$ in the fifth (W_{low}, K is occupied) and for high electron doping $x \approx 0.13$ in the last column (W_{high}, K and Σ are occupied).

orbitals		bare	undoped	doped	
		U (eV)	V (eV)	W_{low} (eV)	W_{high} (eV)
d_{z^2}	d_{z^2}	9.11	1.55	0.82	0.68
d_{z^2}	d_{xy}	8.30	1.29	0.58	0.44
d_{z^2}	$d_{x^2y^2}$	8.30	1.29	0.58	0.44
d_{xy}	d_{xy}	8.89	1.49	0.80	0.64
d_{xy}	$d_{x^2y^2}$	8.52	1.35	0.65	0.51
$d_{x^2y^2}$	$d_{x^2y^2}$	8.89	1.49	0.80	0.64

B.2. $MoSe_2$

- The phonon properties of $MoSe_2$ and their behaviour upon doping were described in the main text in Figs. 5.1, 5.3 and 5.16.
- The Coulomb interaction parameters were given in Tabs. 4.1 and 4.2.

B.3. WS_2

Table B.3.: Parameters of Coulomb interaction in WS_2.

bare U	
leading EV, quadratic	
γ (Å)	2.455
leading EV, cubic	
γ (Å)	2.130
δ (Å^2)	0.720
microscopic EV	
U_2 (eV)	0.712
U_3 (eV)	0.354

dielectric ε	
leading EV, simple	
ε_∞	7.593
d (Å)	11.960
leading EV, pseudo-Resta	
a (1/Å^2)	3.947
b	29.931
c (Å)	5.440
d (Å)	1.578
e	4.497
microscopic EV	
ε_2	2.979
ε_3	2.494

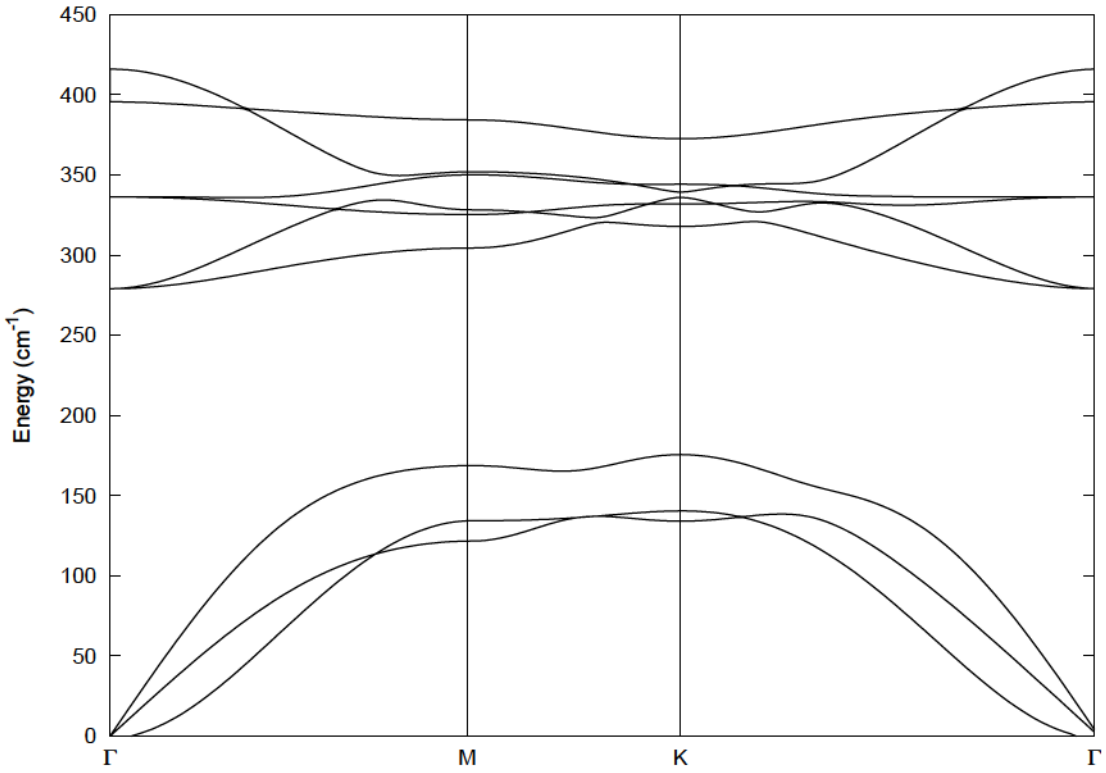

Figure B.1.: Phononic dispersion in undoped WS_2.

Table B.4.: Bare onsite U as well as background screened onsite V and fully screened onsite Coulomb matrix elements W for the three important orbitals in real space. Values for W are in the range of low electron doping $x \approx 0.03$ in the fifth (W_{low}, K is occupied) and for high electron doping $x \approx 0.12$ in the last column (W_{high}, K and Σ are occupied).

orbitals		bare	undoped	doped	
		U (eV)	V (eV)	W_{low} (eV)	W_{high} (eV)
d_{z^2}	d_{z^2}	8.37	1.57	0.89	0.71
d_{z^2}	d_{xy}	7.66	1.33	0.67	0.48
d_{z^2}	$d_{x^2y^2}$	7.66	1.33	0.67	0.48
d_{xy}	d_{xy}	8.19	1.52	0.87	0.68
d_{xy}	$d_{x^2y^2}$	7.84	1.38	0.73	0.54
$d_{x^2y^2}$	$d_{x^2y^2}$	8.19	1.52	0.87	0.68

B.4. WSe_2

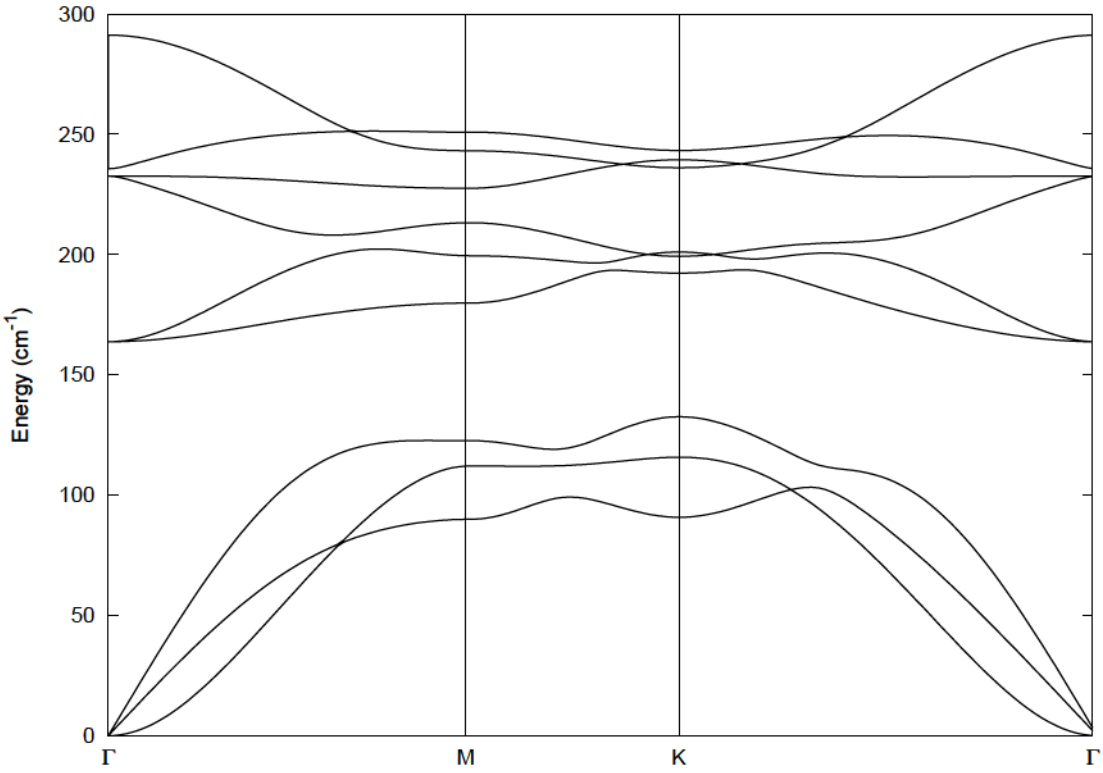

Figure B.2.: Phononic dispersion in undoped WSe_2.

Table B.5.: Parameters of Coulomb interaction in WSe_2.

bare U	
leading EV, quadratic	
γ (Å)	2.376
leading EV, cubic	
γ (Å)	2.297
δ (Å^2)	0.174
microscopic EV	
U_2 (eV)	0.715
U_3 (eV)	0.360

dielectric ε	
leading EV, simple	
ε_∞	8.435
d (Å)	12.661
leading EV, pseudo-Resta	
a (1/Å^2)	2.430
b	20.764
c (Å)	5.761
d (Å)	2.489
e	5.305
microscopic EV	
ε_2	3.028
ε_3	2.481

Table B.6.: Bare onsite U as well as background screened onsite V and fully screened onsite Coulomb matrix elements W for the three important orbitals in real space. Values for W are in the range of low electron doping $x \approx 0.03$ in the fifth (W_{low}, K is occupied) and for high electron doping $x \approx 0.12$ in the last column (W_{high}, K and Σ are occupied).

orbitals		bare	undoped	doped	
		U (eV)	V (eV)	W_{low} (eV)	W_{high} (eV)
d_{z^2}	d_{z^2}	8.33	1.42	0.83	0.65
d_{z^2}	d_{xy}	7.62	1.18	0.61	0.43
d_{z^2}	$d_{x^2y^2}$	7.62	1.18	0.61	0.43
d_{xy}	d_{xy}	8.15	1.38	0.81	0.63
d_{xy}	$d_{x^2y^2}$	7.79	1.23	0.67	0.49
$d_{x^2y^2}$	$d_{x^2y^2}$	8.15	1.38	0.81	0.63

B.5. NbS_2

The phonon dispersion of NbS_2 was already shown in Fig. 5.2.

Table B.7.: Parameters of Coulomb interaction in NbS_2.

bare U	
leading EV, quadratic	
γ (Å)	1.901
leading EV, cubic	
γ (Å)	1.923
δ (Å^2)	-0.046
microscopic EV	
U_2 (eV)	0.877
U_3 (eV)	0.393

dielectric ε	
leading EV, simple	
ε_∞	7.090
d (Å)	9.611
leading EV, pseudo-Resta	
a (1/Å^2)	2.488
b	16.479
c (Å)	5.622
d (Å)	2.143
e	4.105
microscopic EV	
ε_2	2.749
ε_3	2.361

Table B.8.: Bare onsite U as well as background screened onsite V for an empty conduction band and fully screened onsite Coulomb matrix elements W for the three important orbitals in real space.

orbitals		bare U (eV)	empty band V (eV)	undoped W (eV)
d_{z^2}	d_{z^2}	9.19	1.91	0.52
d_{z^2}	d_{xy}	8.32	1.60	0.27
d_{z^2}	$d_{x^2y^2}$	8.32	1.60	0.27
d_{xy}	d_{xy}	8.96	1.84	0.51
d_{xy}	$d_{x^2y^2}$	8.56	1.67	0.35
$d_{x^2y^2}$	$d_{x^2y^2}$	8.96	1.84	0.51

B.6. $NbSe_2$

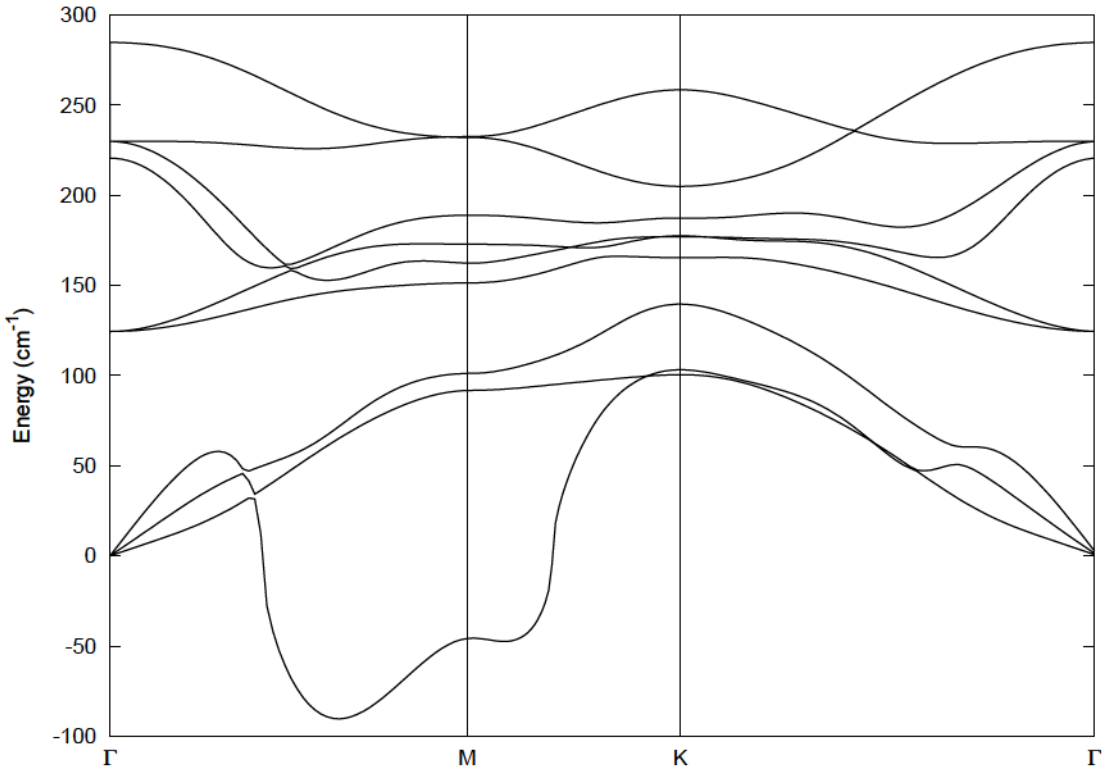

Figure B.3.: Phononic dispersion in undoped $NbSe_2$.

Table B.9.: Parameters of Coulomb interaction in $NbSe_2$.

bare U	
leading EV, quadratic	
γ (Å)	1.934
leading EV, cubic	
γ (Å)	2.161
δ (Å^2)	-0.476
microscopic EV	
U_2 (eV)	0.846
U_3 (eV)	0.384

dielectric ε	
leading EV, simple	
ε_∞	8.011
d (Å)	10.522
leading EV, pseudo-Resta	
a (1/Å^2)	2.040
b	15.149
c (Å)	6.311
d (Å)	2.620
e	5.092
microscopic EV	
ε_2	2.819
ε_3	2.383

Table B.10.: Bare onsite U as well as background screened onsite V for an empty conduction band and fully screened onsite Coulomb matrix elements W for the three important orbitals in real space.

orbitals		bare U (eV)	empty band V (eV)	undoped W (eV)
d_{z^2}	d_{z^2}	8.93	1.53	0.45
d_{z^2}	d_{xy}	8.08	1.23	0.21
d_{z^2}	$d_{x^2y^2}$	8.08	1.23	0.21
d_{xy}	d_{xy}	8.69	1.46	0.44
d_{xy}	$d_{x^2y^2}$	8.31	1.30	0.29
$d_{x^2y^2}$	$d_{x^2y^2}$	8.69	1.46	0.44

B.7. Exchange interaction

Here, we show the values of the exchange interaction as resulting from our RPA calculations for the undoped semiconducting and the half-filled metallic TMDCs.

Table B.11.: Onsite exchange interaction J for the six TMDCs.

Material	orbitals		J (eV)
MoS_2	d_{z^2}	d_{xy} or $d_{x^2y^2}$	0.26
	d_{xy}	$d_{x^2y^2}$	0.15
$MoSe_2$	d_{z^2}	d_{xy} or $d_{x^2y^2}$	0.27
	d_{xy}	$d_{x^2y^2}$	0.15
WS_2	d_{z^2}	d_{xy} or $d_{x^2y^2}$	0.26
	d_{xy}	$d_{x^2y^2}$	0.15
WSe_2	d_{z^2}	d_{xy} or $d_{x^2y^2}$	0.27
	d_{xy}	$d_{x^2y^2}$	0.15
NbS_2	d_{z^2}	d_{xy} or $d_{x^2y^2}$	0.25
	d_{xy}	$d_{x^2y^2}$	0.15
$NbSe_2$	d_{z^2}	d_{xy} or $d_{x^2y^2}$	0.24
	d_{xy}	$d_{x^2y^2}$	0.15

C. Deviation of Coulomb fit from ab-initio data

In Fig. C.1 we show the dependence of the eigenvectors of the bare Coulomb interaction on the wave vector in $MoSe_2$. The errors of our fit model for the interband screened interaction V are presented in Fig. C.2.

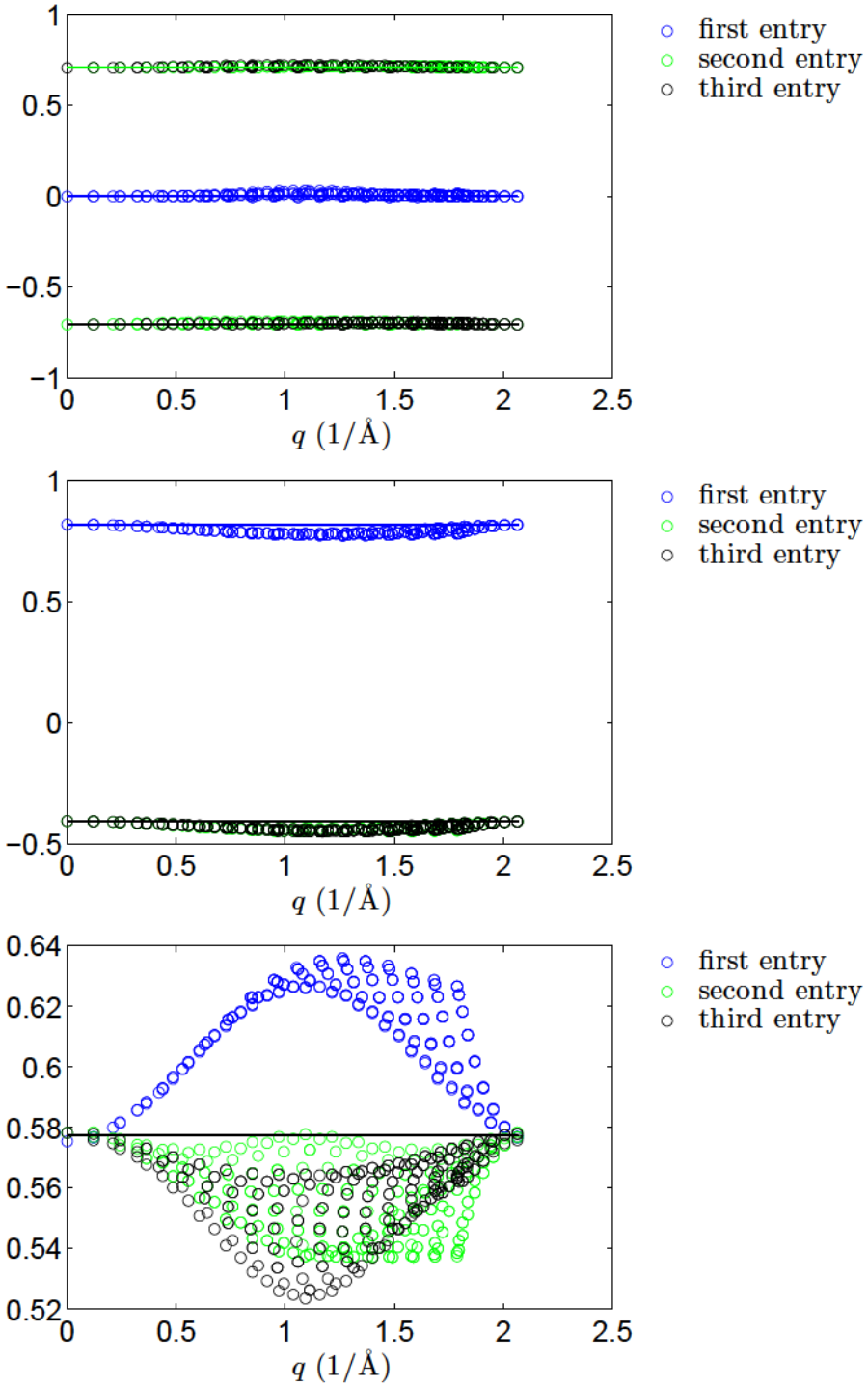

Figure C.1.: Ab-initio data and fit model according to Eq. (4.3) for the eigenvectors of the bare Coulomb interaction in $MoSe_2$.

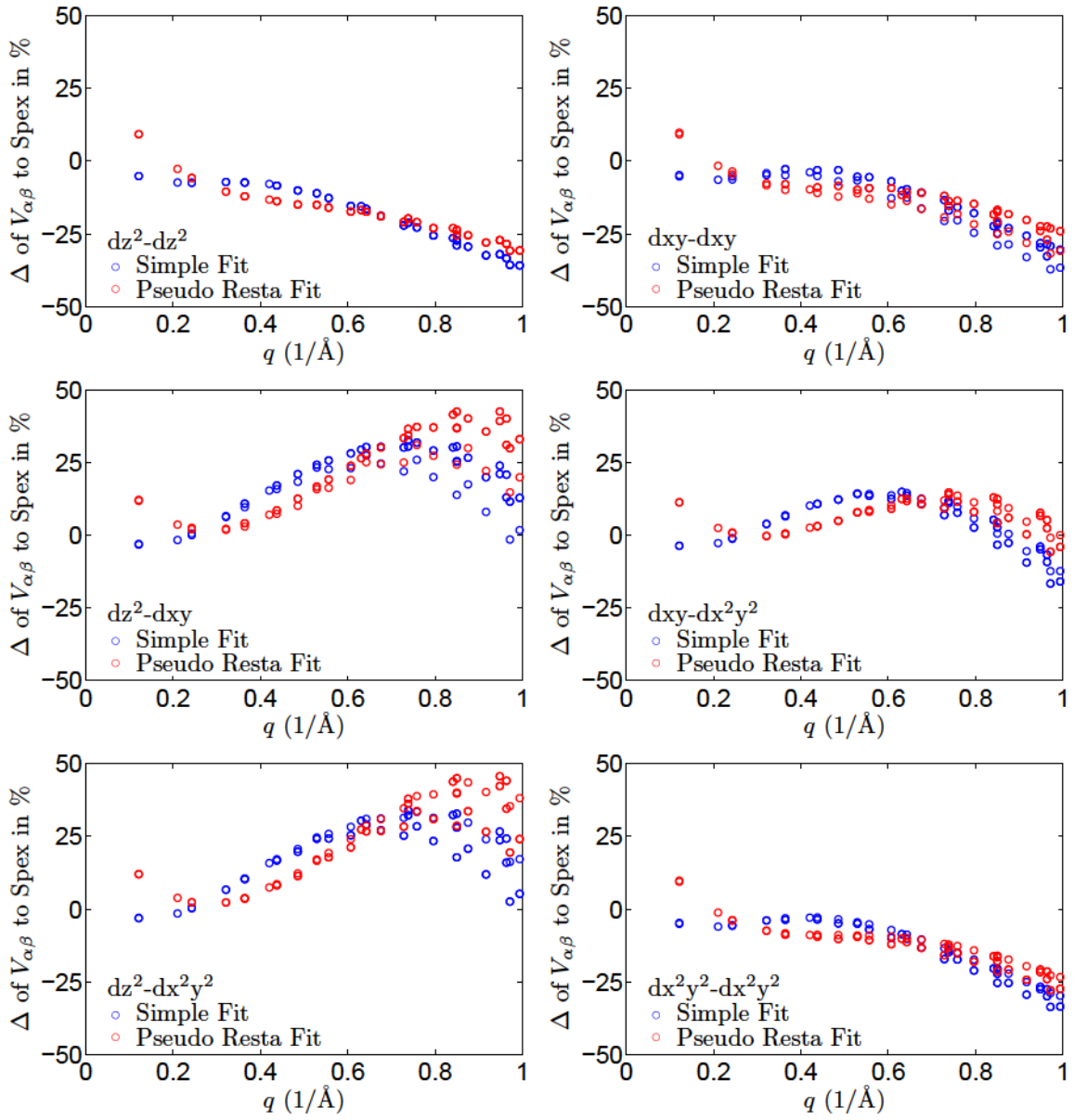

Figure C.2.: Difference in % between ab-initio data and fit model for the interband screened Coulomb interaction in the orbital basis $V_{\alpha\beta}$ in $MoSe_2$.

Bibliography

[1] G. R. Bhimanapati, Z. Lin, V. Meunier, Y. Jung, J. Cha, S. Das, D. Xiao, Y. Son, M. S. Strano, V. R. Cooper, L. Liang, S. G. Louie, E. Ringe, W. Zhou, S. S. Kim, R. R. Naik, B. G. Sumpter, H. Terrones, F. Xia, Y. Wang, J. Zhu, D. Akinwande, N. Alem, J. A. Schuller, R. E. Schaak, M. Terrones, and J. A. Robinson, "Recent Advances in Two-Dimensional Materials beyond Graphene," ACS Nano **9**, 11509–11539 (2015).

[2] K. S. Novoselov, A. K. Geim, S. V. Morozov, D. Jiang, Y. Zhang, S. V. Dubonos, I. V. Grigorieva, and A. A. Firsov, "Electric field effect in atomically thin carbon films," Science **306**, 666–669 (2004).

[3] K. S. Novoselov, D. Jiang, F. Schedin, T. J. Booth, V. V. Khotkevich, S. V. Morozov, and A. K. Geim, "Two-dimensional atomic crystals," PNAS **102**, 10451–10453 (2005).

[4] S. Z. Butler, S. M. Hollen, L. Cao, Y. Cui, J. A. Gupta, H. R. Gutierrez, T. F. Heinz, S. S. Hong, J. Huang, A. F. Ismach, E. Johnston-Halperin, M. Kuno, V. V. Plashnitsa, R. D. Robinson, R. S. Ruoff, S. Salahuddin, J. Shan, L. Shi, M. G. Spencer, M. Terrones, W. Windl, and J. E. Goldberger, "Progress, Challenges, and Opportunities in Two-Dimensional Materials Beyond Graphene," ACS Nano **7**, 2898–2926 (2013).

[5] V. Nicolosi, M. Chhowalla, M. G. Kanatzidis, M. S. Strano, and J. N. Coleman, "Liquid Exfoliation of Layered Materials," Science **340**, 1226419 (2013).

[6] F. Schwierz, "Graphene transistors," Nat. Nano. **5**, 487–496 (2010).

[7] B. Radisavljevic, A. Radenovic, J. Brivio, V. Giacometti, and A. Kis, "Single-layer MoS_2 transistors," Nat. Nano. **6**, 147–150 (2011).

[8] K. S. Novoselov, A. K. Geim, S. V. Morozov, D. Jiang, M. I. Katsnelson, I. V. Grigorieva, S. V. Dubonos, and A. A. Firsov, "Two-dimensional gas of massless Dirac fermions in graphene," Nature **438**, 197–200 (2005).

[9] A. H. Castro Neto, F. Guinea, N. M. R. Peres, K. S. Novoselov, and A. K. Geim, "The electronic properties of graphene," Rev. Mod. Phys. **81**, 109–162 (2009).

[10] T. O. Wehling, A. M. Black-Schaffer, and A. V. Balatsky, "Dirac materials," Advances in Physics **63**, 1–76 (2014).

[11] R. Frindt, "Superconductivity in Ultrathin $NbSe_2$ Layers," Phys. Rev. Lett. **28**, 299–301 (1972).

[12] D. Yang, S. J. Sandoval, W. M. R. Divigalpitiya, J. C. Irwin, and R. F. Frindt, "Structure of single-molecular-layer MoS_2," Phys. Rev. B **43**, 12053–12056 (1991).

[13] S. F. Meyer, R. E. Howard, G. R. Stewart, J. V. Acrivos, and T. H. Geballe, "Properties of intercalated 2H-$NbSe_2$, 4Hb-TaS_2, and 1T-TaS_2," The Journal of Chemical Physics **62**, 4411–4419 (1975).

[14] R. H. Friend and A. D. Yoffe, "Electronic properties of intercalation complexes of the transition metal dichalcogenides," Advances in Physics **36**, 1–94 (1987).

[15] A. Splendiani, L. Sun, Y. Zhang, T. Li, J. Kim, C.-Y. Chim, G. Galli, and F. Wang, "Emerging photoluminescence in monolayer MoS_2," Nano Lett. **10**, 1271–1275 (2010).

[16] M. M. Ugeda, A. J. Bradley, Y. Zhang, S. Onishi, Y. Chen, W. Ruan, C. Ojeda-Aristizabal, H. Ryu, M. T. Edmonds, H.-Z. Tsai, A. Riss, S.-K. Mo, D. Lee, A. Zettl, Z. Hussain, Z.-X. Shen, and M. F. Crommie, "Characterization of collective ground states in single-layer $NbSe_2$," Nat. Phys. **12**, 92–97 (2016).

[17] R. B. Somoano, V. Hadek, A. Rembaum, S. Samson, and J. A. Woollam, "The alkaline earth intercalates of molybdenum disulfide," The Journal of Chemical Physics **62**, 1068–1073 (1975).

[18] J. A. Woollam and R. B. Somoano, "Proceedings of the Franco American Conference on Intercalation Compounds of Graphite Physics and chemistry of MoS_2 intercalation compounds," Materials Science and Engineering **31**, 289–295 (1977).

[19] B. Sipos, A. F. Kusmartseva, A. Akrap, H. Berger, L. Forro, and E. Tutis, "From Mott state to superconductivity inÂ 1t-TaS_2," Nat. Mater. **7**, 960–965 (2008).

[20] J. Paglione and R. L. Greene, "High-temperature superconductivity in iron-based materials," Nat. Phys. **6**, 645–658 (2010).

[21] K. Taniguchi, A. Matsumoto, H. Shimotani, and H. Takagi, "Electric-field-induced superconductivity at 9.4 K in a layered transition metal disulphide MoS_2," Appl. Phys. Lett. **101**, 042603 (2012).

[22] J. T. Ye, Y. J. Zhang, R. Akashi, M. S. Bahramy, R. Arita, and Y. Iwasa, "Superconducting dome in a gate-tuned band insulator," Science **338**, 1193–1196 (2012).

[23] X. Xi, L. Zhao, Z. Wang, H. Berger, L. Forro, J. Shan, and K. F. Mak, "Strongly enhanced charge-density-wave order in monolayer $NbSe_2$," Nat. Nano. **10**, 765–769 (2015).

[24] Y. Yu, F. Yang, X. F. Lu, Y. J. Yan, Y.-H. Cho, L. Ma, X. Niu, S. Kim, Y.-W. Son, D. Feng, S. Li, S.-W. Cheong, X. H. Chen, and Y. Zhang, "Gate-tunable phase transitions in thin flakes of 1T-TaS_2," Nat. Nano. **10**, 270–276 (2015).

[25] J. K. Glasbrenner, I. I. Mazin, H. O. Jeschke, P. J. Hirschfeld, R. M. Fernandes, and R. Valenti, "Effect of magnetic frustration on nematicity and superconductivity in iron chalcogenides," Nat. Phys. **11**, 953–958 (2015).

[26] Y. Cao, A. Mishchenko, G. L. Yu, E. Khestanova, A. P. Rooney, E. Prestat, A. V. Kretinin, P. Blake, M. B. Shalom, C. Woods, J. Chapman, G. Balakrishnan, I. V. Grigorieva, K. S. Novoselov, B. A. Piot, M. Potemski, K. Watanabe, T. Taniguchi, S. J. Haigh, A. K. Geim, and R. V. Gorbachev, "Quality Heterostructures from Two-Dimensional Crystals Unstable in Air by Their Assembly in Inert Atmosphere," Nano Lett. **15**, 4914–4921 (2015).

[27] S. Jo, D. Costanzo, H. Berger, and A. F. Morpurgo, "Electrostatically Induced Superconductivity at the Surface of WS_2," Nano Lett. **15**, 1197–1202 (2015).

[28] W. Shi, J. Ye, Y. Zhang, R. Suzuki, M. Yoshida, J. Miyazaki, N. Inoue, Y. Saito, and Y. Iwasa, "Superconductivity Series in Transition Metal Dichalcogenides by Ionic Gating," Sci. Rep. **5**, 12534 (2015).

[29] H.-P. Komsa and A. V. Krasheninnikov, "Effects of confinement and environment on the electronic structure and exciton binding energy of MoS_2 from first principles," Phys. Rev. B **86**, 241201 (2012).

[30] M. M. Ugeda, A. J. Bradley, S.-F. Shi, F. H. da Jornada, Y. Zhang, D. Y. Qiu, W. Ruan, S.-K. Mo, Z. Hussain, Z.-X. Shen, F. Wang, S. G. Louie, and M. F. Crommie, "Giant bandgap renormalization and excitonic effects in a monolayer transition metal dichalcogenide semiconductor," Nat. Mater. **13**, 1091–1095 (2014).

[31] M. Rösner, C. Steinke, M. Lorke, C. Gies, F. Jahnke, and T. O. Wehling, "Two-Dimensional Heterojunctions from Nonlocal Manipulations of the Interactions," Nano Lett. **16**, 2322–2327 (2016).

[32] A. K. Geim and I. V. Grigorieva, "Van der Waals heterostructures," Nature **499**, 419–425 (2013).

[33] K. S. Novoselov, A. Mishchenko, A. Carvalho, and A. H. C. Neto, "2D materials and van der Waals heterostructures," Science **353**, aac9439 (2016).

[34] T. O. Wehling, E. Şaşıoğlu, C. Friedrich, A. I. Lichtenstein, M. I. Katsnelson, and S. Blügel, "Strength of effective coulomb interactions in graphene and graphite," Phys. Rev. Lett. **106**, 236805 (2011).

[35] M. Schüler, M. Rösner, T. O. Wehling, A. I. Lichtenstein, and M. I. Katsnelson, "Optimal Hubbard Models for Materials with Nonlocal Coulomb Interactions: Graphene, Silicene, and Benzene," Phys. Rev. Lett. **111**, 036601 (2013).

[36] D. Costanzo, S. Jo, H. Berger, and A. F. Morpurgo, "Gate-induced superconductivity in atomically thin MoS_2 crystals," Nat. Nano. **11**, 339–344 (2016).

[37] S. Doniach and E. H. Sondheimer, *Green's functions for solid state physicists*, 2nd ed. (Imperial College Press, London, 1998).

[38] G. D. Mahan, *Many-Particle Physics*, 3rd ed. (Kluwer Academics/Plenum Publishers, New York, 2000).

[39] H. Bruus and K. Flensberg, *Many-body quantum theory in condensed matter physics - an introduction* (Oxford University Press, 2004).

[40] G. Czycholl, *Theoretische Festkörperphysik*, 3rd ed. (Springer-Verlag Berlin Heidelberg, 2008).

[41] U. Rössler, *Solid State Theory: An Introduction*, 2nd ed. (Springer-Verlag Berlin Heidelberg, 2009).

[42] R. B. Laughlin and D. Pines, "The Theory of Everything," PNAS **97**, 28–31 (2000).

[43] M. Born and R. Oppenheimer, "Zur Quantentheorie der Molekeln," Ann. Phys. **389**, 457–484 (1927).

[44] J. Hubbard, "Electron Correlations in Narrow Energy Bands," Proc. R. Soc. Lond. A **276**, 238–257 (1963).

[45] E. Dagotto, "Correlated electrons in high-temperature superconductors," Rev. Mod. Phys. **66**, 763–840 (1994).

[46] N. F. Mott, "Metal-Insulator Transition," Rev. Mod. Phys. **40**, 677–683 (1968).

[47] T. Holstein, "Studies of polaron motion," Annals of Physics **8**, 325–342 (1959).

[48] E. Berger, P. Valasek, and W. von der Linden, "Two-dimensional Hubbard-Holstein model," Phys. Rev. B **52**, 4806–4814 (1995).

[49] W. Koller, D. Meyer, Y. Ono, and A. C. Hewson, "First- and second-order phase transitions in the Holstein-Hubbard model," EPL **66**, 559 (2004).

[50] G. H. Wannier, "The Structure of Electronic Excitation Levels in Insulating Crystals," Phys. Rev. **52**, 191–197 (1937).

[51] A. A. Mostofi, J. R. Yates, Y.-S. Lee, I. Souza, D. Vanderbilt, and N. Marzari, "wannier90: A tool for obtaining maximally-localised Wannier functions," Comp. Phys. Comm. **178**, 685–699 (2008).

[52] A. A. Mostofi, J. R. Yates, G. Pizzi, Y.-S. Lee, I. Souza, D. Vanderbilt, and N. Marzari, "An updated version of wannier90: A tool for obtaining maximally-localised Wannier functions," Comp. Phys. Comm. **185**, 2309–2310 (2014).

[53] N. Marzari and D. Vanderbilt, "Maximally localized generalized Wannier functions for composite energy bands," Phys. Rev. B **56**, 12847–12865 (1997).

[54] I. Souza, N. Marzari, and D. Vanderbilt, "Maximally localized Wannier functions for entangled energy bands," Phys. Rev. B **65**, 035109 (2001).

[55] P. Hohenberg and W. Kohn, "Inhomogeneous electron gas," Phys. Rev. **136**, B864–B871 (1964).

[56] W. Kohn and L. J. Sham, "Self-consistent equations including exchange and correlation effects," Phys. Rev. **140**, A1133–A1138 (1965).

[57] R. Jones, "Density functional theory: Its origins, rise to prominence, and future," Rev. Mod. Phys. **87**, 897–923 (2015).

[58] A. J. Cohen, P. Mori-Sanchez, and W. Yang, "Challenges for Density Functional Theory," Chem. Rev. **112**, 289–320 (2012).

[59] V. I. Anisimov, F. Aryasetiawan, and A. I. Lichtenstein, "First-principles calculations of the electronic structure and spectra of strongly correlated systems: the LDA + U method," J. Phys.: Condens. Matter **9**, 767 (1997).

[60] A. Georges, G. Kotliar, W. Krauth, and M. J. Rozenberg, "Dynamical mean-field theory of strongly correlated fermion systems and the limit of infinite dimensions," Rev. Mod. Phys. **68**, 13–125 (1996).

[61] P. Giannozzi, S. Baroni, N. Bonini, M. Calandra, R. Car, C. Cavazzoni, D. Ceresoli, G. L. Chiarotti, M. Cococcioni, I. Dabo, A. D. Corso, S. d. Gironcoli, S. Fabris, G. Fratesi, R. Gebauer, U. Gerstmann, C. Gougoussis, A. Kokalj, M. Lazzeri, L. Martin-Samos, N. Marzari, F. Mauri, R. Mazzarello, S. Paolini, A. Pasquarello, L. Paulatto, C. Sbraccia, S. Scandolo, G. Sclauzero, A. P. Seitsonen, A. Smogunov, P. Umari, and R. M. Wentzcovitch, "QUANTUM ESPRESSO: a modular and open-source software project for quantum simulations of materials," J. Phys.: Condens. Matter **21**, 395502 (2009).

[62] "The juelich fleur project," `http://www.flapw.de` (2014).

[63] G. Kresse and J. Hafner, "Ab initio molecular dynamics for liquid metals," Phys. Rev. B **47**, 558–561 (1993).

[64] G. Kresse and J. Furthmüller, "Efficient iterative schemes for ab initio total-energy calculations using a plane-wave basis set," Phys. Rev. B **54**, 11169–11186 (1996).

[65] R. O. Jones and O. Gunnarsson, "The density functional formalism, its applications and prospects," Rev. Mod. Phys. **61**, 689–746 (1989).

[66] J. P. Perdew and Y. Wang, "Accurate and simple analytic representation of the electron-gas correlation energy," Phys. Rev. B **45**, 13244–13249 (1992).

[67] A. D. Becke, "Density-functional exchange-energy approximation with correct asymptotic behavior," Phys. Rev. A **38**, 3098–3100 (1988).

[68] A. Roy, H. C. P. Movva, B. Satpati, K. Kim, R. Dey, A. Rai, T. Pramanik, S. Guchhait, E. Tutuc, and S. K. Banerjee, "Structural and Electrical Properties of $MoTe_2$ and $MoSe_2$ Grown by Molecular Beam Epitaxy," ACS Appl. Mater. Interfaces **8**, 7396–7402 (2016).

[69] J. P. Perdew, K. Burke, and M. Ernzerhof, "Generalized gradient approximation made simple," Phys. Rev. Lett. **77**, 3865–3868 (1996).

[70] D. Bohm and D. Pines, "A collective description of electron interactions: III. coulomb interactions in a degenerate electron gas," Phys. Rev. **92**, 609–625 (1953).

[71] R. E. Groenewald, M. Rösner, G. Schönhoff, S. Haas, and T. O. Wehling, "Valley plasmonics in transition metal dichalcogenides," Phys. Rev. B **93**, 205145 (2016).

[72] J. Lindhard, *On the properties of a gas of charged particles.* (I kommission hos Munksgaard, Copenhagen, 1954).

[73] M. Rösner, *Electronic Structure of Novel Two-dimensional Materials and Graphene Heterostructures*, Ph.D. thesis, University of Bremen (2016).

[74] S. Das Sarma, S. Adam, E. H. Hwang, and E. Rossi, "Electronic transport in two-dimensional graphene," Rev. Mod. Phys. **83**, 407–470 (2011).

[75] F. Stern, "Polarizability of a two-dimensional electron gas," Phys. Rev. Lett. **18**, 546–548 (1967).

[76] B. Mihaila, "Lindhard function of a d-dimensional fermi gas," arXiv:1111.5337 [cond-mat, physics:math-ph] (2011).

[77] F. Aryasetiawan, K. Karlsson, O. Jepsen, and U. Schönberger, "Calculations of Hubbard U from first-principles," Phys. Rev. B **74**, 125106 (2006).

[78] T. Miyake and F. Aryasetiawan, "Screened Coulomb interaction in the maximally localized Wannier basis," Phys. Rev. B **77**, 085122 (2008).

[79] E. Şaşıoğlu, C. Friedrich, and S. Blügel, "Effective Coulomb interaction in transition metals from constrained random-phase approximation," Phys. Rev. B **83**, 121101 (2011).

[80] M. Kaltak, *Merging GW with DMFT*, Ph.D. thesis, University of Vienna (2015).

[81] M. Rösner, E. Şaşıoğlu, C. Friedrich, S. Blügel, and T. O. Wehling, "Wannier function approach to realistic Coulomb interactions in layered materials and heterostructures," Phys. Rev. B **92**, 085102 (2015).

[82] C. Friedrich, A. Schindlmayr, and S. Blügel, "Efficient calculation of the Coulomb matrix and its expansion around within the FLAPW method," Comp. Phys. Comm. **180**, 347–359 (2009).

[83] C. Friedrich, S. Blügel, and A. Schindlmayr, "Efficient implementation of the GW approximation within the all-electron FLAPW method," Phys. Rev. B **81**, 125102 (2010).

[84] F. Aryasetiawan and O. Gunnarsson, "The GW method," Rep. Prog. Phys. **61**, 237 (1998).

[85] L. Hedin, "On correlation effects in electron spectroscopies and the GW approximation," J. Phys.: Condens. Matter **11**, R489 (1999).

[86] G. Onida, L. Reining, and A. Rubio, "Electronic excitations: density-functional versus many-body Green's-function approaches," Rev. Mod. Phys. **74**, 601–659 (2002).

[87] L. Hedin, "New Method for Calculating the One-Particle Green's Function with Application to the Electron-Gas Problem," Phys. Rev. **139**, A796–A823 (1965).

[88] C. Rostgaard, K. W. Jacobsen, and K. S. Thygesen, "Fully self-consistent GW calculations for molecules," Phys. Rev. B **81**, 085103 (2010).

[89] S. Biermann, F. Aryasetiawan, and A. Georges, "First-Principles Approach to the Electronic Structure of Strongly Correlated Systems: Combining the GW Approximation and Dynamical Mean-Field Theory," Phys. Rev. Lett. **90**, 086402 (2003).

[90] A. N. Rubtsov, M. I. Katsnelson, and A. I. Lichtenstein, "Dual boson approach to collective excitations in correlated fermionic systems," Annals of Physics **327**, 1320–1335 (2012).

[91] E. G. C. P. van Loon, A. I. Lichtenstein, M. I. Katsnelson, O. Parcollet, and H. Hafermann, "Beyond extended dynamical mean-field theory: Dual boson approach to the two-dimensional extended Hubbard model," Phys. Rev. B **90**, 235135 (2014).

[92] S. Baroni, S. de Gironcoli, A. Dal Corso, and P. Giannozzi, "Phonons and related crystal properties from density-functional perturbation theory," Rev. Mod. Phys. **73**, 515–562 (2001).

[93] R. Heid, "Density functional perturbation theory and electron phonon coupling," in *Emergent Phenomena in Correlated Matter*, Lecture Notes of the Autumn School Correlated Electrons (2013).

[94] D. J. Scalapino, J. R. Schrieffer, and J. W. Wilkins, "Strong-coupling superconductivity. i," Phys. Rev. **148**, 263–279 (1966).

[95] J. T. Devreese, "Fröhlich Polarons. Lecture course including detailed theoretical derivations," arXiv:1012.4576 [cond-mat] (2010), arXiv: 1012.4576.

[96] H. Onnes, "Van der Waals heterostructures," Commun. Phys. Lab. Univ. Leiden **12**, 120 (1911).

[97] J. G. Bednorz and K. A. Müller, "Possible high-Tc superconductivity in the Ba-La-Cu-O system," Z. Physik B - Condensed Matter **64**, 189–193 (1986).

[98] Y. Kamihara, T. Watanabe, M. Hirano, and H. Hosono, "Iron-Based Layered Superconductor La[$O_{1-x}F_x$]FeAs ($x = 0.05 - 0.12$) with $T_c = 26$ K," J. Am. Chem. Soc. **130**, 3296–3297 (2008).

[99] M. R. Norman, "The Challenge of Unconventional Superconductivity," Science **332**, 196–200 (2011).

[100] F. Wang and D.-H. Lee, "The Electron-Pairing Mechanism of Iron-Based Superconductors," Science **332**, 200–204 (2011).

[101] K. H. Bennemann and J. B. Ketterson, eds., *Superconductivity - Volume 1: Conventional and unconventional superconductors* (Springer-Verlag Berlin Heidelberg, 2008).

[102] V. Z. Kresin, H. Morawitz, and S. A. Wolf, *Superconducting State. Mechanism and Properties*, 1st ed. (Oxford University Press, Oxford, 2014).

[103] J. Bardeen, L. N. Cooper, and J. R. Schrieffer, "Theory of superconductivity," Phys. Rev. **108**, 1175–1204 (1957).

[104] J. Bardeen, L. N. Cooper, and J. R. Schrieffer, "Microscopic theory of superconductivity," Phys. Rev. **106**, 162–164 (1957).

[105] F. London and H. London, "The electromagnetic equations of the supraconductor," Proc. R. Soc. Lond. A **149**, 71–88 (1935).

[106] L. N. Cooper, "Bound electron pairs in a degenerate fermi gas," Phys. Rev. **104**, 1189–1190 (1956).

[107] A. P. Drozdov, M. I. Eremets, I. A. Troyan, V. Ksenofontov, and S. I. Shylin, "Conventional superconductivity at 203 kelvin at high pressures in the sulfur hydride system," Nature **525**, 73–76 (2015).

[108] G. A. C. Ummarino, "Eliashberg Theory," in *Emergent Phenomena in Correlated Matter*, Lecture Notes of the Autumn School Correlated Electrons (2013).

[109] G. M. Eliashberg, "Interactions between electrons and lattice vibrations in a superconductor," Sov. Phys. JETP **11**, 696 (1960).

[110] Y. Nambu, "Quasi-particles and gauge invariance in the theory of superconductivity," Phys. Rev. **117**, 648–663 (1960).

[111] A. B. Migdal, "Interaction between electrons and lattice vibrations in a normal metal," Sov. Phys. JETP **7**, 996 (1958).

[112] J. Berges, *On the scope of McMillan's formula*, Master's thesis, University of Bremen (2016).

[113] G. Schönhoff, *Coulomb interaction and superconductivity in doped MoS_2*, Master's thesis, University of Bremen (2015).

[114] P. Morel and P. W. Anderson, "Calculation of the superconducting state parameters with retarded electron-phonon interaction," Phys. Rev. **125**, 1263–1271 (1962).

[115] P. B. Allen and R. C. Dynes, "Transition temperature of strong-coupled superconductors reanalyzed," Phys. Rev. B **12**, 905–922 (1975).

[116] W. L. McMillan, "Transition temperature of strong-coupled superconductors," Phys. Rev. **167**, 331–344 (1968).

[117] T. Ando, A. Fowler, and F. Stern, "Electronic properties of two-dimensional systems," Rev. Mod. Phys. **54**, 437–672 (1982).

[118] X. Li, W. Cai, J. An, S. Kim, J. Nah, D. Yang, R. Piner, A. Velamakanni, I. Jung, E. Tutuc, S. K. Banerjee, L. Colombo, and R. S. Ruoff, "Large-Area Synthesis of High-Quality and Uniform Graphene Films on Copper Foils," Science **324**, 1312–1314 (2009).

[119] L. Britnell, R. V. Gorbachev, R. Jalil, B. D. Belle, F. Schedin, A. Mishchenko, T. Georgiou, M. I. Katsnelson, L. Eaves, S. V. Morozov, N. M. R. Peres, J. Leist, A. K. Geim, K. S. Novoselov, and L. A. Ponomarenko, "Field-effect tunneling transistor based on vertical graphene heterostructures," Science **335**, 947–950 (2012).

[120] Q. H. Wang, K. Kalantar-Zadeh, A. Kis, J. N. Coleman, and M. S. Strano, "Electronics and optoelectronics of two-dimensional transition metal dichalcogenides," Nat. Nano. **7**, 699–712 (2012).

[121] R. Roldan, J. A. Silva-Guillen, M. P. Lopez-Sancho, F. Guinea, E. Cappelluti, and P. Ordejon, "Electronic properties of single-layer and multilayer transition metal dichalcogenides MX_2 (M = Mo, W and X = S, Se)," Annalen der Physik **526**, 347–357 (2014).

[122] M. Bernardi, C. Ataca, M. Palummo, and J. C. Grossman, "Optical and Electronic Properties of Two-Dimensional Layered Materials," Nanophotonics **0**, 111–125 (2016).

[123] M. Chhowalla, H. S. Shin, G. Eda, L.-J. Li, K. P. Loh, and H. Zhang, "The chemistry of two-dimensional layered transition metal dichalcogenide nanosheets," Nat. Chem. **5**, 263–275 (2013).

[124] F. A. Rasmussen and K. S. Thygesen, "Computational 2d Materials Database: Electronic Structure of Transition-Metal Dichalcogenides and Oxides," J. Phys. Chem. C **119**, 13169–13183 (2015).

[125] C. Drummond, N. Alcantar, J. Israelachvili, R. Tenne, and Y. Golan, "Microtribology and Friction-Induced Material Transfer in WS_2 Nanoparticle Additives," Adv. Funct. Mater. **11**, 348–354 (2001).

[126] H. Wang, H. Yuan, S. S. Hong, Y. Li, and Y. Cui, "Physical and chemical tuning of two-dimensional transition metal dichalcogenides," Chem. Soc. Rev. **44**, 2664–2680 (2015).

[127] D. Jariwala, V. K. Sangwan, L. J. Lauhon, T. J. Marks, and M. C. Hersam, "Emerging Device Applications for Semiconducting Two-Dimensional Transition Metal Dichalcogenides," ACS Nano **8**, 1102–1120 (2014).

[128] R. Lv, J. A. Robinson, R. E. Schaak, D. Sun, Y. Sun, T. E. Mallouk, and M. Terrones, "Transition Metal Dichalcogenides and Beyond: Synthesis, Properties, and Applications of Single- and Few-Layer Nanosheets," Acc. Chem. Res. **48**, 56–64 (2015).

[129] L. Britnell, R. M. Ribeiro, A. Eckmann, R. Jalil, B. D. Belle, A. Mishchenko, Y.-J. Kim, R. V. Gorbachev, T. Georgiou, S. V. Morozov, A. N. Grigorenko, A. K. Geim, C. Casiraghi, A. H. C. Neto, and K. S. Novoselov, "Strong Light-Matter Interactions in Heterostructures of Atomically Thin Films," Science **340**, 1311–1314 (2013).

[130] H. Wang, H. Feng, and J. Li, "Graphene and Graphene-like Layered Transition Metal Dichalcogenides in Energy Conversion and Storage," Small **10**, 2165–2181 (2014).

[131] S. Wi, H. Kim, M. Chen, H. Nam, L. J. Guo, E. Meyhofer, and X. Liang, "Enhancement of Photovoltaic Response in Multilayer MoS_2 Induced by Plasma Doping," ACS Nano **8**, 5270–5281 (2014).

[132] V. Podzorov, M. E. Gershenson, C. Kloc, R. Zeis, and E. Bucher, "High-mobility field-effect transistors based on transition metal dichalcogenides," App. Phys. Lett. **84**, 3301–3303 (2004).

[133] S. Kim, A. Konar, W.-S. Hwang, J. H. Lee, J. Lee, J. Yang, C. Jung, H. Kim, J.-B. Yoo, J.-Y. Choi, Y. W. Jin, S. Y. Lee, D. Jena, W. Choi, and K. Kim, "High-mobility and low-power thin-film transistors based on multilayer MoS_2 crystals," Nat. Comm. **3**, 1011 (2012).

[134] A. A. Tedstone, D. J. Lewis, and P. O'Brien, "Synthesis, Properties, and Applications of Transition Metal-Doped Layered Transition Metal Dichalcogenides," Chem. Mater. **28**, 1965–1974 (2016).

[135] P. E. Blöchl, O. Jepsen, and O. K. Andersen, "Improved tetrahedron method for Brillouin-zone integrations," Phys. Rev. B **49**, 16223–16233 (1994).

[136] Y. Zhang, T.-R. Chang, B. Zhou, Y.-T. Cui, H. Yan, Z. Liu, F. Schmitt, J. Lee, R. Moore, Y. Chen, H. Lin, H.-T. Jeng, S.-K. Mo, Z. Hussain, A. Bansil, and Z.-X. Shen, "Direct observation of the transition from indirect to direct bandgap in atomically thin epitaxial $MoSe_2$," Nat. Nano. **9**, 111–115 (2014).

[137] K. F. Mak, C. Lee, J. Hone, J. Shan, and T. F. Heinz, "Atomically thin MoS_2: A new direct-gap semiconductor," Phys. Rev. Lett. **105**, 136805 (2010).

[138] D. Y. Qiu, F. H. da Jornada, and S. G. Louie, "Optical Spectrum of MoS_2: Many-Body Effects and Diversity of Exciton States," Phys. Rev. Lett. **111**, 216805 (2013).

[139] W. Zhao, Z. Ghorannevis, L. Chu, M. Toh, C. Kloc, P.-H. Tan, and G. Eda, "Evolution of electronic structure in atomically thin sheets of WS_2 and WSe_2," ACS Nano **7**, 791–797 (2013).

[140] A. Kuc, N. Zibouche, and T. Heine, "Influence of quantum confinement on the electronic structure of the transition metal sulfide TS_2," Phys. Rev. B **83**, 245213 (2011).

[141] H. R. Gutierrez, N. Perea-Lopez, A. L. Elias, A. Berkdemir, B. Wang, R. Lv, F. Lopez-Urias, V. H. Crespi, H. Terrones, and M. Terrones, "Extraordinary Room-Temperature Photoluminescence in Triangular WS_2 Monolayers," Nano Lett. **13**, 3447–3454 (2013).

[142] A. Steinhoff, M. Rösner, F. Jahnke, T. O. Wehling, and C. Gies, "Influence of excited carriers on the optical and electronic properties of MoS_2," Nano Lett. **14**, 3743–3748 (2014).

[143] I. M. Lifshitz, "Anomalies of electron characteristics of a metal in the high pressure region," Sov. Phys. JETP **11**, 1130 (1960).

[144] Z. Y. Zhu, Y. C. Cheng, and U. Schwingenschlögl, "Giant spin-orbit-induced spin splitting in two-dimensional transition-metal dichalcogenide semiconductors," Phys. Rev. B **84**, 153402 (2011).

[145] X. Xu, W. Yao, D. Xiao, and T. F. Heinz, "Spin and pseudospins in layered transition metal dichalcogenides," Nat. Phys. **10**, 343–350 (2014).

[146] L. Van Hove, "The Occurrence of Singularities in the Elastic Frequency Distribution of a Crystal," Phys. Rev. **89**, 1189–1193 (1953).

[147] C.-H. Chang, X. Fan, S.-H. Lin, and J.-L. Kuo, "Orbital analysis of electronic structure and phonon dispersion in MoS_2, $MoSe_2$, WS_2, and WSe_2 monolayers under strain," Phys. Rev. B **88**, 195420 (2013).

[148] A. Kormanyos, G. Burkard, M. Gmitra, J. Fabian, V. Zolyomi, N. D. Drummond, and V. Fal'ko, "k · p theory for two-dimensional transition metal dichalcogenide semiconductors," 2D Mater. **2**, 022001 (2015).

[149] A. K. Geim and K. S. Novoselov, "The rise of graphene," Nat. Mater. **6**, 183–191 (2007).

[150] A. K. Geim, "Graphene: Status and Prospects," Science **324**, 1530–1534 (2009).

[151] P. Avouris, "Graphene: Electronic and Photonic Properties and Devices," Nano Lett. **10**, 4285–4294 (2010).

[152] K. S. Novoselov, V. I. Fal'ko, L. Colombo, P. R. Gellert, M. G. Schwab, and K. Kim, "A roadmap for graphene," Nature **490**, 192–200 (2012).

[153] D. C. Elias, R. R. Nair, T. M. G. Mohiuddin, S. V. Morozov, P. Blake, M. P. Halsall, A. C. Ferrari, D. W. Boukhvalov, M. I. Katsnelson, A. K. Geim, and K. S. Novoselov, "Control of Graphene's Properties by Reversible Hydrogenation: Evidence for Graphane," Science **323**, 610–613 (2009).

[154] S. Yuan, M. Rösner, A. Schulz, T. O. Wehling, and M. I. Katsnelson, "Electronic Structures and Optical Properties of Partially and Fully Fluorinated Graphene," Phys. Rev. Lett. **114**, 047403 (2015).

[155] T. O. Wehling, B. Grundkötter-Stock, B. Aradi, T. Frauenheim, and T. Niehaus, "Charge-doping-induced phase transitions in hydrogenated and fluorinated graphene," Phys. Rev. B **90**, 085422 (2014).

[156] D. Haberer, C. E. Giusca, Y. Wang, H. Sachdev, A. V. Fedorov, M. Farjam, S. A. Jafari, D. V. Vyalikh, D. Usachov, X. Liu, U. Treske, M. Grobosch, O. Vilkov, V. K. Adamchuk, S. Irle, S. R. P. Silva, M. Knupfer, B. Büchner, and A. Grüneis, "Evidence for a New Two-Dimensional C_4H-Type Polymer Based on Hydrogenated Graphene," Adv. Mater. **23**, 4497–4503 (2011).

[157] F. Hüser, T. Olsen, and K. S. Thygesen, "How dielectric screening in two-dimensional crystals affects the convergence of excited-state calculations: Monolayer MoS_2," Phys. Rev. B **88**, 245309 (2013).

[158] K. Andersen, S. Latini, and K. S. Thygesen, "Dielectric Genome of van der Waals Heterostructures," Nano Lett. **15**, 4616–4621 (2015).

[159] G. Schönhoff, M. Rösner, R. E. Groenewald, S. Haas, and T. O. Wehling, "Interplay of screening and superconductivity in low-dimensional materials," Phys. Rev. B **94**, 134504 (2016).

[160] A. Emelyanenko and L. Boinovich, "On the effect of discrete charges adsorbed at the interface on nonionic liquid film stability: charges in the film," J. Phys.: Condens. Matter **20**, 494227 (2008).

[161] R. Resta, "Thomas-Fermi dielectric screening in semiconductors," Phys. Rev. B **16**, 2717–2722 (1977).

[162] F. Roth, A. König, J. Fink, B. Büchner, and M. Knupfer, "Electron energy-loss spectroscopy: A versatile tool for the investigations of plasmonic excitations," J. Electron Spectrosc. Relat. Phenom. **195**, 85–95 (2014).

[163] B. Santoyo and M. Mussot, "Plasmons in three, two and one dimension," Revista Mexicana de Fisica **39**, 640–652 (1993).

[164] E. H. Hwang and S. Das Sarma, "Dielectric function, screening, and plasmons in two-dimensional graphene," Phys. Rev. B **75**, 205418 (2007).

[165] H. Morawitz, I. Bozovic, V. Z. Kresin, G. Rietveld, and D. v. d. Marel, "The plasmon density of states of a layered electron gas," Z. Physik B - Condensed Matter **90**, 277–281 (1993).

[166] A. Bill, H. Morawitz, and V. Z. Kresin, "Electronic collective modes and superconductivity in layered conductors," Phys. Rev. B **68**, 144519 (2003).

[167] J. Homola, S. S. Yee, and G. Gauglitz, "Surface plasmon resonance sensors: review," Sensors and Actuators B: Chemical **54**, 3–15 (1999).

[168] S. A. Maier, *Plasmonics: fundamentals and applications* (Springer Science & Business Media, 2007).

[169] F. H. L. Koppens, D. E. Chang, and F. J. Garcia de Abajo, "Graphene Plasmonics: A Platform for Strong Light-Matter Interactions," Nano Lett. **11**, 3370–3377 (2011).

[170] L. Ju, B. Geng, J. Horng, C. Girit, M. Martin, Z. Hao, H. A. Bechtel, X. Liang, A. Zettl, Y. R. Shen, and F. Wang, "Graphene plasmonics for tunable terahertz metamaterials," Nat. Nano. **6**, 630–634 (2011).

[171] A. N. Grigorenko, M. Polini, and K. S. Novoselov, "Graphene plasmonics," Nat Photon **6**, 749–758 (2012).

[172] Y. Takada, "Plasmon Mechanism of Superconductivity in Two- and Three-Dimensional Electron Systems," Journal of the Physical Society of Japan **45**, 786–794 (1978).

[173] R. Akashi and R. Arita, "Development of density-functional theory for a plasmon-assisted superconducting state: Application to lithium under high pressures," Phys. Rev. Lett. **111**, 057006 (2013).

[174] R. Akashi and R. Arita, "Density functional theory for plasmon-assisted superconductivity," J. Phys. Soc. Jpn. **83**, 061016 (2014).

[175] H. Yan, T. Low, W. Zhu, Y. Wu, M. Freitag, X. Li, F. Guinea, P. Avouris, and F. Xia, "Damping pathways of mid-infrared plasmons in graphene nanostructures," Nat. Photon. **7**, 394–399 (2013).

[176] A. Principi, G. Vignale, M. Carrega, and M. Polini, "Intrinsic lifetime of Dirac plasmons in graphene," Phys. Rev. B **88**, 195405 (2013).

[177] A. Scholz, T. Stauber, and J. Schliemann, "Plasmons and screening in a monolayer of MoS_2," Phys. Rev. B **88**, 035135 (2013).

[178] K. Kechedzhi and D. S. L. Abergel, "Weakly damped acoustic plasmon mode in transition metal dichalcogenides with Zeeman splitting," Phys. Rev. B **89**, 235420 (2014).

[179] K. Andersen and K. S. Thygesen, "Plasmons in metallic monolayer and bilayer transition metal dichalcogenides," Phys. Rev. B **88**, 155128 (2013).

[180] J. van Wezel, R. Schuster, A. König, M. Knupfer, J. van den Brink, H. Berger, and B. Büchner, "Effect of Charge Order on the Plasmon Dispersion in Transition-Metal Dichalcogenides," Phys. Rev. Lett. **107**, 176404 (2011).

[181] P. Cudazzo, E. Müller, C. Habenicht, M. Gatti, H. Berger, M. Knupfer, Angel Rubio, and S. Huotari, "Negative plasmon dispersion in 2H-NbS_2 beyond the charge-density-wave interpretation," New J. Phys. **18**, 103050 (2016).

[182] A. König, K. Koepernik, R. Schuster, R. Kraus, M. Knupfer, B. Büchner, and H. Berger, "Plasmon evolution and charge-density wave suppression in potassium intercalated 2H-$TaSe_2$," EPL **100**, 27002 (2012).

[183] A. König, R. Schuster, M. Knupfer, B. Büchner, and H. Berger, "Doping dependence of the plasmon dispersion in 2H-$TaSe_2$," Phys. Rev. B **87**, 195119 (2013).

[184] F. Güller, V. L. Vildosola, and A. M. Llois, "Spin density wave instabilities in the NbS_2 monolayer," Phys. Rev. B **93**, 094434 (2016).

[185] Y. Nakata, K. Sugawara, R. Shimizu, Y. Okada, P. Han, T. Hitosugi, K. Ueno, T. Sato, and T. Takahashi, "Monolayer 1t-NbSe2 as a Mott insulator," NPG Asia Mater. **8**, e321 (2016).

[186] N. D. Mermin and H. Wagner, "Absence of Ferromagnetism or Antiferromagnetism in One- or Two-Dimensional Isotropic Heisenberg Models," Phys. Rev. Lett. **17**, 1133–1136 (1966).

[187] P. C. Hohenberg, "Existence of Long-Range Order in One and Two Dimensions," Phys. Rev. **158**, 383–386 (1967).

[188] V. L. Berezinskii, "Destruction of long-range order in one-dimensional and two-dimensional systems having a continuous symmetry group. I. classical systems," Sov. Phys. JETP **32**, 493 (1971).

[189] J. M. Kosterlitz and D. J. Thouless, "Ordering, metastability and phase transitions in two-dimensional systems," Journal of Physics C: Solid State Physics **6**, 1181 (1973).

[190] S. Horzum, H. Sahin, S. Cahangirov, P. Cudazzo, A. Rubio, T. Serin, and F. M. Peeters, "Phonon softening and direct to indirect band gap crossover in strained single-layer $MoSe_2$," Phys. Rev. B **87**, 125415 (2013).

[191] A. Molina-Sanchez and L. Wirtz, "Phonons in single-layer and few-layer MoS2 and WS2," Phys. Rev. B **84**, 155413 (2011).

[192] Y. Ge and A. Y. Liu, "Phonon-mediated superconductivity in electron-doped single-layer MoS_2: A first-principles prediction," Phys. Rev. B **87**, 241408 (2013).

[193] M. Rösner, S. Haas, and T. O. Wehling, "Phase diagram of electron-doped dichalcogenides," Phys. Rev. B **90**, 245105 (2014).

[194] M. Calandra, I. I. Mazin, and F. Mauri, "Effect of dimensionality on the charge-density wave in few-layer 2H-$NbSe_2$," Phys. Rev. B **80**, 241108 (2009).

[195] M. Leroux, M. Le Tacon, M. Calandra, L. Cario, M.-A. Measson, P. Diener, E. Borrissenko, A. Bosak, and P. Rodiere, "Anharmonic suppression of charge density waves in 2H-NbS_2," Phys. Rev. B **86**, 155125 (2012).

[196] M. D. Johannes and I. I. Mazin, "Fermi surface nesting and the origin of charge density waves in metals," Phys. Rev. B **77**, 165135 (2008).

[197] D. J. Scalapino, E. Loh, and J. E. Hirsch, "d-wave pairing near a spin-density-wave instability," Phys. Rev. B **34**, 8190–8192 (1986).

[198] H. Rietschel and L. J. Sham, "Role of electron Coulomb interaction in superconductivity," Phys. Rev. B **28**, 5100–5108 (1983).

[199] M. Calandra, P. Zoccante, and F. Mauri, "Universal Increase in the Superconducting Critical Temperature of Two-Dimensional Semiconductors at Low Doping by the Electron-Electron Interaction," Phys. Rev. Lett. **114**, 077001 (2015).

[200] O. Gunnarsson and G. Zwicknagl, "Coulomb pseudopotential, screening and superconductivity in C_{60}," Phys. Rev. Lett. **69**, 957–960 (1992).

[201] K.-H. Lee, K. J. Chang, and M. L. Cohen, "First-principles calculations of the coulomb pseudopotential μ^*: Application to al," Phys. Rev. B **52**, 1425–1428 (1995).

[202] C.-Y. Moon, Y.-H. Kim, and K. J. Chang, "Dielectric-screening properties and Coulomb pseudopotential μ^* for MgB_2," Phys. Rev. B **70**, 104522 (2004).

[203] D. Jerome, A. J. Grant, and A. D. Yoffe, "Pressure enhanced superconductivity in $NbSe_2$," Solid State Comm. **9**, 2183–2185 (1971).

[204] V. G. Tissen, M. R. Osorio, J. P. Brison, N. M. Nemes, M. Garcia-Hernandez, L. Cario, P. Rodiere, S. Vieira, and H. Suderow, "Pressure dependence of superconducting critical temperature and upper critical field of 2H-NbS_2," Phys. Rev. B **87**, 134502 (2013).

[205] A. M. Finkel'stein, "Suppression of superconductivity in homogeneously disordered systems," Physica B: Condensed Matter **197**, 636–648 (1994).

[206] J. Chang, E. Blackburn, A. T. Holmes, N. B. Christensen, J. Larsen, J. Mesot, R. Liang, D. A. Bonn, W. N. Hardy, A. Watenphul, M. v. Zimmermann, E. M. Forgan, and S. M. Hayden, "Direct observation of competition between superconductivity and charge density wave order in $YBa_2Cu_3O_{6.67}$," Nat. Phys. **8**, 871–876 (2012).

[207] G. Savini, A. C. Ferrari, and F. Giustino, "First-Principles Prediction of Doped Graphane as a High-Temperature Electron-Phonon Superconductor," Phys. Rev. Lett. **105**, 037002 (2010).

[208] A. P. Durajski, "Influence of hole doping on the superconducting state in graphane," Supercond. Sci. Technol. **28**, 035002 (2015).

[209] B. M. Ludbrook, G. Levy, P. Nigge, M. Zonno, M. Schneider, D. J. Dvorak, C. N. Veenstra, S. Zhdanovich, D. Wong, P. Dosanjh, C. Straßer, A. Stöhr, S. Forti, C. R. Ast, U. Starke, and A. Damascelli, "Evidence for superconductivity in Li-decorated monolayer graphene," PNAS **112**, 11795–11799 (2015).

[210] E. R. Margine, H. Lambert, and F. Giustino, "Electron-phonon interaction and pairing mechanism in superconducting Ca-intercalated bilayer graphene," Sci. Rep. **6** (2016).

[211] H.-Y. Lu, L. Hao, R. Wang, and C. S. Ting, "Ferromagnetism and superconductivity with possible $p + ip$ pairing symmetry in partially hydrogenated graphene," Phys. Rev. B **93**, 241410 (2016).

[212] J. Chapman, Y. Su, C. A. Howard, D. Kundys, A. N. Grigorenko, F. Guinea, A. K. Geim, I. V. Grigorieva, and R. R. Nair, "Superconductivity in Ca-doped graphene laminates," Sci. Rep. **6**, 23254 (2016).

[213] A. Y. Liu, I. I. Mazin, and J. Kortus, "Beyond Eliashberg Superconductivity in MgB_2: Anharmonicity, Two-Phonon Scattering, and Multiple Gaps," Phys. Rev. Lett. **87**, 087005 (2001).

[214] J. Nagamatsu, N. Nakagawa, T. Muranaka, Y. Zenitani, and J. Akimitsu, "Superconductivity at 39 K in magnesium diboride," Nature **410**, 63–64 (2001).

[215] H. J. Choi, D. Roundy, H. Sun, M. L. Cohen, and S. G. Louie, "First-principles calculation of the superconducting transition in MgB_2 within the anisotropic eliashberg formalism," Phys. Rev. B **66**, 020513 (2002).

[216] K. H. Bennemann and J. B. Ketterson, eds., *The Physics of Superconductors* (Springer Berlin Heidelberg, Berlin, Heidelberg, 2003).

[217] R. Roldan, E. Cappelluti, and F. Guinea, "Interactions and superconductivity in heavily doped MoS_2," Phys. Rev. B **88**, 054515 (2013).

[218] J. Yuan and C. Honerkamp, "Triplet pairing driven by Hund's coupling in doped monolayer MoS_2," arXiv:1504.04536 [cond-mat] (2015).

[219] C. D. Malliakas and M. G. Kanatzidis, "Nb-Nb Interactions Define the Charge Density Wave Structure of 2H-$NbSe_2$," J. Am. Chem. Soc. **135**, 1719–1722 (2013).

[220] M. Leroux, I. Errea, M. Le Tacon, S.-M. Souliou, G. Garbarino, L. Cario, A. Bosak, F. Mauri, M. Calandra, and P. Rodiere, "Strong anharmonicity induces quantum melting of charge density wave in 2H-$NbSe_2$ under pressure," Phys. Rev. B **92**, 140303 (2015).

[221] F. Flicker and J. van Wezel, "Charge order from orbital-dependent coupling evidenced by $NbSe_2$," Nat. Commun. **6**, 7034 (2015).

[222] F. Flicker and J. van Wezel, "Charge ordering geometries in uniaxially strained $NbSe_2$," Phys. Rev. B **92**, 201103 (2015).

[223] X. Xi, H. Berger, L. Forro, J. Shan, and K. F. Mak, "Gate Tuning of Electronic Phase Transitions in Two-Dimensional $NbSe_2$," Phys. Rev. Lett. **117**, 106801 (2016).

[224] R. Samnakay, D. Wickramaratne, T. R. Pope, R. K. Lake, T. T. Salguero, and A. A. Balandin, "Zone-Folded Phonons and the Commensurate-Incommensurate Charge-Density-Wave Transition in 1T-$TaSe_2$ Thin Films," Nano Lett. **15**, 2965–2973 (2015).

[225] R. E. Peierls, *Quantum Theory of Solids* (Oxford University New York/London, 1955).

[226] G. Grüner, "The dynamics of charge-density waves," Rev. Mod. Phys. **60**, 1129–1181 (1988).

[227] Y. Ma, Y. Dai, M. Guo, C. Niu, Y. Zhu, and B. Huang, "Evidence of the Existence of Magnetism in Pristine VX_2 Monolayers (X = S, Se) and Their Strain-Induced Tunable Magnetic Properties," ACS Nano **6**, 1695–1701 (2012).

[228] H. Zhang, L.-M. Liu, and W.-M. Lau, "Dimension-dependent phase transition and magnetic properties of VS_2," J. Mat. Chem. A **1**, 10821–10828 (2013).

[229] Y. Zhou, Z. Wang, P. Yang, X. Zu, L. Yang, X. Sun, and F. Gao, "Tensile Strain Switched Ferromagnetism in Layered NbS_2 and $NbSe_2$," ACS Nano **6**, 9727–9736 (2012).

[230] E. Şaşıoğlu, A. Schindlmayr, C. Friedrich, F. Freimuth, and S. Blügel, "Wannier-function approach to spin excitations in solids," Phys. Rev. B **81**, 054434 (2010).

[231] S. Tongay, J. Zhou, C. Ataca, K. Lo, T. S. Matthews, J. Li, J. C. Grossman, and J. Wu, "Thermally Driven Crossover from Indirect toward Direct Bandgap in 2d Semiconductors: $MoSe_2$ versus MoS_2," Nano Lett. **12**, 5576–5580 (2012).

[232] N. Troullier and J. L. Martins, "Efficient pseudopotentials for plane-wave calculations," Phys. Rev. B **43**, 1993–2006 (1991).

[233] C. Hartwigsen, S. Goedecker, and J. Hutter, "Relativistic separable dual-space Gaussian pseudopotentials from H to Rn," Phys. Rev. B **58**, 3641–3662 (1998).

List of publications

Published in peer-reviewed journals

- *Valley plasmonics in transition metal dichalcogenides.*
  R. E. Groenewald, M. Rösner, G. Schönhoff, S. Haas, and T. O. Wehling.
  Phys. Rev. **B** 93, 205145 (2016).
- *Interplay of screening and superconductivity in low-dimensional materials.*
  G. Schönhoff, M. Rösner, R. E. Groenewald, S. Haas, and T. O. Wehling.
  Phys. Rev. **B** 94, 134504 (2016).

Under review

- *Observation of exciton redshift-blueshift crossover in monolayer WS_2.*
  E. J. Sie, A. Steinhoff, C. Gies, C. H. Lui, Q. Ma, M. Rösner, G. Schönhoff, F. Jahnke, T. O. Wehling, Y.-H. Lee, J. Kong, P. Jarillo-Herrero, and N. Gedik.
  Submitted to Nano Lett. (2017)

Conference contributions

- Talk: *From optics to superconductivity: Many body effects in transition metal dichalcogenides.*
  G. Schönhoff, M. Rösner, A. Steinhoff, A. Schulz, F. Jahnke, C. Gies, S. Haas, T. O. Wehling.
  Towards Reality in Nanoscale Materials VIII, Levi, Finland,
  February 9th - 11th, 2015.

- Talk: *Coulomb interaction in transition metal dichalcogenides: effects on many-body instabilities.*
  G. Schönhoff, M. Rösner, S. Haas, T. O. Wehling.
  DPG Meeting, Regensburg, March 08th, 2016.

- Talk: *Coulomb interaction in transition metal dichalcogenides: effects on many-body instabilities.*
  G. Schönhoff, M. Rösner, R. E. Groenewald, C. Steinke, S. Haas, T. O. Wehling.
  Cecam Workshop, Bremen, June 28th, 2016.

- Talk: *Description of superconductivity, charge order, and magnetism in 2D materials.*
  G. Schönhoff, M. Rösner, E. v. Loon, R. E. Groenewald, S. Haas, M. Katsnelson, T. O. Wehling.
  QM^3 Workshop, Bremen, February 28th, 2017.

Acknowledgements

Many people have contributed to the work that was presented in this thesis. First of all, I would like to thank Tim Wehling for giving me the opportunity to work in his group and to write this thesis; this work would not have been possible without his support, his many ideas and the helpful discussions. Secondly, I am very thankful to Gerd Czycholl for acting as the co-referee of this thesis.

I thank all of our working group for the great atmosphere and a lot of help. In particular, I thank Malte Rösner for introducing me to the field of 2D materials and sharing a lot of his knowledge and skills with me. I enjoyed all the interesting discussions with Christian Renk and Jan Berges in our office, not only concerning physics. Jan Berges, Malte Schüler and Ebad Kamil have been really helpful with the proofreading of this manuscript. I also thank Klaus Bowe and Andreas Beuthner for their help with the hardware and software and Sarah-Jane Farley for her help with organizational problems.

Finally, I thank my family and Svenja for their ongoing support.